

ABSTRACT

LABARBERA, DARRELL ANDREW. Microstructural Modeling of Hot Spot and Failure Mechanisms in RDX Energetic Aggregates. (Under the direction of Dr. Mohammed Zikry).

Hot spot formation and failure mechanisms, such as dynamic fracture and shear strain localization, for RDX (cyclotrimethylene trinitramine)-polymer binder aggregates were investigated for dynamic thermo-mechanical loading conditions. A formulation based on a dislocation-density based crystalline plasticity and a finite viscoelasticity framework was coupled to a microstructurally-based dynamic fracture nucleation and propagation method, and it was used to investigate interrelated high strain-rate failure modes in RDX-polymer binder energetic aggregates. The effects of grain boundary (GB) misorientations, porosity, grain morphologies, dislocation densities, and crystal-binder interactions were coupled with adiabatic plasticity heating, thermal decomposition, thermal conduction, and dissipated heat to predict and understand hot spot formation for a PCTFE (Polychlorotrifluoroethylene) polymer binder. The validated predictions indicate that hot spots were induced by inelastic deformation modes, which resulted in unbounded temperatures due to localized plasticity and thermal decomposition at the peripheries of the voids.

Viscous dissipation, due to the estane polymer binder, where the operating temperatures were above the glass transition temperature, resulted in RDX crystal interactions due to hydrostatic compression of the polymer binder. This hydrostatic compression constrained the polymer binder interfaces, which enhanced RDX inelastic deformation modes and resulted in and accelerated hot spot formation at the RDX crystal peripheries in the interfacial regions between the estane binder and the RDX crystals.

The effects of dynamic crack nucleation and propagation were also investigated in energetic aggregates subjected to high strain rate loading conditions. The fracture approach was based on an overlapping elements method, and cracks were nucleated on preferential cleavage planes. Cracks nucleated from the peripheries of the voids and propagated towards the RDX-estane interfaces, where they were arrested. Large accumulations of plasticity occurred, at the RDX-estane interfaces, where the cracks were arrested, and this subsequently resulted in hot spot formation. Bicrystals with random low and high angle grain boundary (GB) misorientations were also investigated to further understand dynamic crack propagation and arrest at RDX-estane interfaces. For low angle GB misorientations, a pre-existing crack propagated towards the binder and was arrested at the interface due to low stresses in the binder, with little inelastic deformation occurring near the crack front. For high angle GB misorientations, the pre-existing crack propagated towards the interface, but was arrested due to crack front plasticity and dislocation-density accumulation.

The analyses, from this study, have been used to predict hot spot formation, shear strain localization, dynamic crack nucleation, propagation, and arrest in RDX-estane energetic aggregates, which have been subjected to dynamic, thermo-mechanical loading conditions. These predictions indicate that hot spot formation and dynamic failure nucleation, propagation, and arrest can be controlled through the optimization of dominant microstructural characteristics, such as RDX crystal and GB orientations, estane interfaces and distributions, and porosity.

© Copyright 2013 Darrell Andrew LaBarbera

All Rights Reserved

Microstructural Modeling of Hot Spot and Failure Mechanisms in
RDX Energetic Aggregates

by
Darrell Andrew LaBarbera

A dissertation submitted to the Graduate Faculty of
North Carolina State University
in partial fulfillment of the
requirements for the degree of
Doctor of Philosophy

Mechanical Engineering

Raleigh, North Carolina

2014

APPROVED BY:

Mohammed Zikry
Committee Chair

Jeffery Eischen

Larry Silverberg

Michael Steer

DEDICATION

I dedicate this dissertation to my parents, Richard and Susan, and my close uncle and aunt, Mike and Katy. Without them, I would have never been instilled with the curiosity to learn how the world around me works, nor would I have the common sense to apply what I have learned to real world problems. I attribute these great qualities, which I learned from them, to the accomplishments I have achieved thus far and to those to come in the future.

BIOGRAPHY

Darrell Andrew LaBarbera was born in Roanoke, Virginia on May 4th, 1988. He was raised in Roanoke until age 4 when his family moved to Raleigh, NC. He graduated from Wake Forest-Rolesville High school in June of 2006. He attended North Carolina State University for his undergraduate studies in Mechanical Engineering. During his undergraduate career, he worked as an engineering intern at SunTech Medical Inc. where he made most of his contributions in the area of tool and die design for RF welding machinery with applications to disposable blood pressure cuffs. He graduated cum laude with a Bachelors of Science degree in Mechanical Engineering in May of 2010.

Darrell continued directly into graduate studies at North Carolina State University. His research focused on crystalline plasticity and the finite element method with applications to explosive materials under the advising of Dr. Mohammed Zikry. He earned a Master of Science degree in Mechanical Engineering in May of 2012. He also earned a Master of Science degree in Material Science and Engineering in May of 2013. The research relating to the this dissertation has generated the following research papers and proceedings:

D. A. LaBarbera and M.A. Zikry, “Microstructural Behavior of Energetic Crystalline Aggregates,” Mater. Res. Soc. Symp. Proc. Volume 1513

D. A. LaBarbera and M. A. Zikry, “The Effects Of Microstructural Defects on Hot Spot Formation in cyclotrimethylenetrinitramine-polychlorotrifluoroethylene Energetic Aggregates,” *Journal of Applied Physics*, 113

J. Brown, **D. LaBarbera**, M.A. Zikry, “Laser Interaction Effects of Electromagnetic Absorption and Microstructural Defects on Hot Spot Formation in RDX-PCTFE Energetic Aggregates”, *Modeling and Simulation in Materials Science and Engineering*, 22

D. A. LaBarbera, and M. A. Zikry, "Heterogeneous Thermo-Mechanical Behavior and Hot Spot Formation in RDX-Estane Energetic Aggregates," Submitted.

D. A. LaBarbera, and M. A. Zikry, "Dynamic Fracture and Local Failure Mechanisms in Heterogeneous RDX-Estane Energetic Aggregates," Submitted.

D. A. LaBarbera, and M. A. Zikry, "Interfacial Fracture Failure in Heterogeneous RDX Estane Energetic Aggregates," Submitted.

Upon completion of the Doctor of Philosophy degree in Mechanical Engineering, he will begin work as a postdoc at Los Alamos National Laboratory under the direction of Dr. Mark Short and Dr. Scott Jackson. His postdoctoral work will focus on theory, simulation, and experimentation of non-ideal high explosive material performance.

ACKNOWLEDGMENTS

I would like to first and foremost acknowledge my fiancée, Amanda, for helping me through all of my toughest times. You made the hard times more bearable and kept encouraging me to keep pressing on. I would like to acknowledge my parents, Richard and Susan, for guiding me to be the person I am today. I would like to acknowledge my older brother, Brad, for the idea to pursue a degree in the field of material science, and my younger brother, Matt, for all the evenings of golf and basketball that helped me relax and recharge from my research.

A special thanks goes to Dr. Mohammed Zikry for his insightful comments and guidance throughout my research. I would also like to thank my doctoral committee member's - Dr. Mohammed Zikry, Dr. Jeffery Eischen, Dr. Larry Silverberg, and Dr. Michael Steer - for providing valuable feedback on my research. I would like to thank my co-workers Dr. William Lee, Dr. Tarek Hatem, Dr. Pratheek Shanthraj, Dr. Khalil Elkhodary, Dr. Prasenjit Khanikar, Dr. Siqi Xu, Cliff McKenzie, Dr. Letisha McLaughlin, Shoayb Ziae, Qifeng Wu, Judith Brown, Matt Bond, Tamir Hasan, Michael Rosenberg, and Ismail Mohamed with special thanks to Dr. William Lee for being my living Crystal2D manual and to Judith Brown for all the enlightening discussions dealing with our joint research. I would like to acknowledge the U.S. Office of Naval Research for funding this research project as a Multi-Disciplinary University Research Initiative on Sound and Electromagnetic Interacting Waves (SEMI-Wave) under grant number N00014-10-1-0958.

TABLE OF CONTENTS

LIST OF TABLES	viii
LIST OF FIGURES	ix
CHAPTER 1: Introduction	1
1.1 Overview	1
1.2 General Research Objectives and Approach.....	4
1.3 Dissertation Organization	5
CHAPTER 2: Crystalline Plasticity Formulation, Finite Viscoelasticity Formulation, and Thermo-Mechanical Coupling	6
2.1 Multiple Slip Crystal Plasticity Kinematics.....	6
2.2 Dislocation Density Evolution	8
2.3 Finite Viscoelasticity Formulation.....	12
2.4 Thermo-Mechanical Coupling	14
2.5 Tables and Figures	16
CHAPTER 3: Numerical Methods.....	19
3.1 Determination of the Total Velocity Gradient.....	19
3.2 Determination of the Plastic Velocity Gradient	21
3.3 Solving Systems of ODE's	22
3.4 Finite Element Representation of Thermal Conduction	23
CHAPTER 4: The Effects of Microstructural Defects on Hot Spot Formation in RDX-PCTFE Energetic Aggregates.....	25
4.1 Introduction	25
4.2 Results	25
4.2.1 750 MPa Pressure Loading and Random Low Angle GB Distributions	27
4.2.2 1 GPA Pressure Loading and Random Low Angle GB Distributions.....	29
4.2.3 750 MPa Pressure Loading and Random High Angle GB Distributions	31
4.3 Summary.....	33
4.4 Tables and Figures	35
CHAPTER 5: Heterogeneous Thermo-Mechanical Behavior and Hot Spot Formation in RDX-Estane Energetic Aggregates	48
5.1 Introduction	48
5.2 Results	48
5.2.1 Validation of the Viscoelastic Model	49
5.2.2 Dynamic Tensile Pressure Loading of 1 GPa.....	50
5.2.3 Dynamic Compressive Pressure Loading of 1 GPa.....	55
5.3 Summary.....	58
5.4 Tables and Figures	61
CHAPTER 6: Dynamic Fracture and Local Failure Mechanisms in Heterogeneous RDX-Estane Energetic Aggregates	76
6.1 Introduction	76
6.2 Results	76

6.2.1 1,000 s ⁻¹ Nominal Strain Rate	77
6.2.2 10,000 s ⁻¹ Nominal Strain Rate	81
6.3 Summary.....	84
6.4 Tables and Figures	86
CHAPTER 7: The Effects of Grain Boundary Misorientations on Fracture Propagation and Crack Stability at Crystalline-Amorphous Energetic Interfaces.....	98
7.1 Introduction	98
7.2 Results	98
7.2.1 Bi-Crystal, Random Low Angle GB Misorientations for a Nominal Strain Rate of 10,000 s ⁻¹	99
7.2.2 Bi-Crystal, Random High Angle GB Misorientations for a Nominal Strain Rate of 10,000 s ⁻¹	102
7.2.3 16 Crystal Aggregate, Random Low Angle GB Misorientations for a Nominal Strain Rate of 10,000 s ⁻¹	106
7.3 Summary.....	107
7.4 Tables and Figures	109
CONCLUSIONS	125
FUTURE RESEARCH RECOMMENDATIONS	127
REFERENCES.....	128

LIST OF TABLES

Table 2.1: Summary of interactions and coefficient values in an RDX crystal.....	16
Table 2.2: Summary of g-coefficients for dislocation density evolution equations	17
Table 5.1: Material Properties of RDX and Estane binder	61
Table 6.1: RDX and Estane binder Material Properties	86
Table 7.1: Material Properties for RDX and Estane	109

LIST OF FIGURES

Figure 2.1: Generalized Maxwell Model for Viscoelastic Materials.....	18
Figure 4.1: The RDX-polymer aggregate with loading, boundary conditions, and void distribution	35
Figure 4.2. (a) Rotation, (b) Normal Stress, (c) Pressure, and (d) Accumulated plastic shear strain for a 750 MPa compressive loading with low misorientations.....	36
Figure 4.3. (a) Immobile dislocation density 1, (b) Immobile dislocation density 2, (c) Immobile dislocation density 3 for a 750 MPa compressive loading with low misorientations.....	37
Figure 4.4. (a) Total temperature, (b) Decomposition temperature, (c) Plastic work temperature for a 750 MPa compressive loading with low misorientations.....	38
Figure 4.5. Temperature and normal stress as a function of time for a 750 MPa compressive loading with low GB misorientations.....	39
Figure 4.6. (a) Rotation, (b) Normal Stress, (c) Pressure, and (d) Accumulated plastic shear strain for a 1 GPa compressive loading with low angle GB misorientations.....	40
Figure 4.7. (a) Immobile dislocation density 1, (b) Immobile dislocation density 2, (c) Immobile dislocation density 3 for a 1 GPa compressive loading with low GB misorientations.....	41
Figure 4.8. (a) Total Temperature, (b) Decomposition Temperature, (c) Plastic Work Temperature for a 1 GPa Compressive loading with low misorientations.....	42
Figure 4.9. Temperature and normal stress as a function of time for a 1 GPa compressive loading with low angle GB misorientations. Hot spot initiation occurs due to an unbounded temperature caused by increases in thermal decomposition.....	43
Figure 4.10. (a) Rotation, (b) Normal Stress, (c) Pressure, and (d) Accumulated plastic shear strain for a 750 MPa compressive loading with high angle GB misorientations.....	44
Figure 4.11. (a) Immobile dislocation Density 1, (b) Immobile dislocation density 2, (c) Immobile dislocation density 3 for a 750 MPa compressive loading with high angle GB misorientations.....	45
Figure 4.12. (a) Total Temperature, (b) Decomposition Temperature, (c) Plastic Work Temperature for a 750 MPa Compressive loading with high misorientations.....	46
Figure 4.13. Temperature and normal stress as a function of time for a 750 MPa compressive loading with high misorientations.....	47
Figure 5.1: The RDX-Estane aggregate with loading, boundary conditions, and void distribution	62
Figure 5.2: The Estane model with loading and boundary conditions used for model validation.....	63
Figure 5.3: (a) Quasi-static strain rate of 0.005 s^{-1} , (b) dynamic strain rate of 2000 s^{-1} comparison of viscoelastic model with experimental data for estane.....	64
Figure 5.4: (a) Temperature, (b) normal stress, (c) lateral stress, and (d) shear stress for a 1 GPA tensile loading with low angle GB misorientations. (Spatial dimensions are in units of meters)	65

Figure 5.5: (a) Dissipated energy, (b) pressure, and (c) plastic shear slip for a 1 GPA tensile loading with low angle GB misorientations. (Spatial dimensions are in units of meters)	66
Figure 5.6: (a) Mobile dislocation density 1, (b) mobile dislocation density 2, and (c) mobile dislocation density 3 for a 1 GPA tensile loading with low angle GB misorientations. (Spatial dimensions are in units of meters)	67
Figure 5.7: (a) Immobile dislocation density 1, (b) immobile dislocation density 2, and (c) immobile dislocation density 3 for a 1 GPA tensile loading with low angle random GB misorientations. (Spatial dimensions are in units of meters)	68
Figure 5.8: Temperature, normal stress, shear stress, and pressure time history for the region where a hotspot formation occurred for a 1 GPA tensile loading with low angle GB misorientations	69
Figure 5.9: (a) Temperature, (b) normal stress, (c) lateral stress, and (d) shear stress for a 1 GPA compressive loading with low angle GB misorientations. (Spatial dimensions are in units of meters)	70
Figure 5.10: (a) Dissipated energy, (b) pressure, and (c) plastic shear slip for a 1 GPA compressive loading with low angle GB misorientations. (Spatial dimensions are in units of meters)	71
Figure 5.11: (a) Mobile dislocation density 1, (b) mobile dislocation density 2, and (c) mobile dislocation density 3 for a 1 GPA compressive loading with low angle GB misorientations. (Spatial dimensions are in units of meters)	72
Figure 5.12: (a) Immobile dislocation density 1, (b) immobile dislocation density 2, and (c) immobile dislocation density 3 for a 1 GPA compressive loading with low angle GB misorientations. (Spatial dimensions are in units of meters)	73
Figure 5.13: Temperature, normal stress, shear stress, and pressure time history for the region where a hotspot formation occurred for a 1 GPA compressive loading with low angle GB misorientations	74
Figure 5.14: (a) The spatial location where temperature and pressure data were extracted (specifically along the straight line within the circled region) and (b) is the spatial distribution for temperature and pressure across the RDX-Estane interface	75
Figure 6.1: The RDX-estane aggregate with loading and boundary conditions, void distribution, and grain morphology	87
Figure 6.2: (a) Normal Stress, (b) lateral stress, (c) shear stress, and (d) pressure for a nominal strain rate loading of $1,000 \text{ s}^{-1}$ and at a nominal strain of 9.0%. (Spatial dimensions are in units of meters)	88
Figure 6.3: (a) Temperature, (b) shear slip, (c) zoomed in view of (a), and (d) dissipated energy for a nominal strain rate loading of $1,000 \text{ s}^{-1}$ and at a nominal strain of 9.0%. (Spatial dimensions are in units of meters)	89
Figure 6.4: (a) Mobile and (b) immobile dislocation densities for the most active slip system for a nominal strain rate loading of $1,000 \text{ s}^{-1}$ and at a nominal strain of 9.0%. (Spatial dimensions are in units of meters)	90

Figure 6.5: Normal stress, pressure, shear stress, lateral stress, mobile and immobile dislocation density, for slip system one, time history for the interface-crack interaction region for a nominal strain rate loading of $1,000 \text{ s}^{-1}$	91
Figure 6.6: Stress-Strain curve for a nominal strain rate loading of $1,000 \text{ s}^{-1}$	92
Figure 6.7: (a) Normal Stress, (b) lateral stress, (c) shear stress, and (d) pressure for a nominal strain rate loading of $10,000 \text{ s}^{-1}$ and at a nominal strain of 9.4%. (Spatial dimensions are in units of meters)	93
Figure 6.8: (a) Temperature, (b) shear slip, (c) zoomed in view of (a), and (d) dissipated energy for a nominal strain rate loading of $10,000 \text{ s}^{-1}$ and at a nominal strain of 9.4%. (Spatial dimensions are in units of meters).....	94
Figure 6.9: (a) Mobile and (b) immobile dislocation densities for the most active slip system for a nominal strain rate loading of $10,000 \text{ s}^{-1}$ and at a nominal strain of 9.4%. (Spatial dimensions are in units of meters)	95
Figure 6.10: Normal stress, pressure, shear stress, lateral stress, mobile and immobile dislocation density time history for the interface-crack interaction region for a nominal strain rate loading of $10,000 \text{ s}^{-1}$	96
Figure 6.11: Stress-Strain curve for a nominal strain rate loading of $10,000 \text{ s}^{-1}$	97
Figure 7.1: The RDX-estane bi-crystal with loading, boundary conditions, and grain morphology.....	110
Figure 7.2: (a) Normal Stress, (b) lateral stress, (c) shear stress, and (d) pressure for a nominal strain rate loading of $10,000 \text{ s}^{-1}$, at a nominal strain of 6.5%, and random low angle GB misorientations. (Spatial dimensions are in units of meters).....	111
Figure 7.3: Normal stress, shear stress, and lateral stress spatial distribution across the RDX-estane interface for a nominal strain rate loading of $10,000 \text{ s}^{-1}$, at a nominal strain of 6.5%, and random low angle GB misorientations.	112
Figure 7.4: (a) Temperature, (b) shear slip, and (c) dissipated energy for a nominal strain rate loading of $10,000 \text{ s}^{-1}$, at a nominal strain of 6.5%, and random low angle GB misorientations. (Spatial dimensions are in units of meters)	113
Figure 7.5: (a) Mobile dislocation density and (b) immobile dislocation density for slip system one, which was the most active slip system, for a nominal strain rate loading of $10,000 \text{ s}^{-1}$, at a nominal strain of 6.5%, and random low angle GB misorientations. (Spatial dimensions are in units of meters).....	114
Figure 7.6: Crack tip velocity versus time for the crack propagating from the initial pre-crack, for a nominal strain rate loading of $10,000 \text{ s}^{-1}$ and random low angle GB misorientations.	115
Figure 7.7: Nominal stress-strain curve for a nominal strain rate loading of $10,000 \text{ s}^{-1}$ and random low angle GB misorientations.	116
Figure 7.8: (a) Normal Stress, (b) lateral stress, (c) shear stress, and (d) pressure for a nominal strain rate loading of $10,000 \text{ s}^{-1}$, at a nominal strain of 7.5%, and random high angle GB misorientations. (Spatial dimensions are in units of meters).....	117
Figure 7.9: (a) Temperature, (b) shear slip, and (c) dissipated energy for a nominal strain rate loading of $10,000 \text{ s}^{-1}$, at a nominal strain of 7.5%, and random high angle GB misorientations. (Spatial dimensions are in units of meters)	118

Figure 7.10: Immobile dislocation densities for (a) slip system one, (b) slip system two, and (c) slip system three for a nominal strain rate loading of $10,000 \text{ s}^{-1}$, at a nominal strain of 7.5%, and random high angle GB misorientations. (Spatial dimensions are in units of meters).....	119
Figure 7.11: Time history plot of normal stress, pressure, lateral stress, and temperature for a nominal strain rate loading of $10,000 \text{ s}^{-1}$ and random high angle GB misorientations in the critical element location.....	120
Figure 7.12: Crack tip velocity versus time for the crack propagating from the initial pre-crack, for a nominal strain rate loading of $10,000 \text{ s}^{-1}$ and random high angle GB misorientations.....	121
Figure 7.13: Stress versus strain curves for a nominal strain rate loading of $10,000 \text{ s}^{-1}$, for random low and high angle GB misorientations.....	122
Figure 7.14: The RDX-estane aggregate with loading and boundary conditions, pre-existing crack, grain morphology.....	123
Figure 7.15: (a) Immobile dislocation densities for slip system one, (b) inelastic shear slip, and (c) dissipated energy due to viscous effects and plasticity for a nominal strain rate loading of $10,000 \text{ s}^{-1}$, at a nominal strain of 10%, and random low angle GB misorientations. (Spatial dimensions are in units of meters)	124

CHAPTER 1: Introduction

1.1 Overview

Detonations of energetic materials can lead to damage of infrastructure and loss of life. Detonations can occur when the sensitivity, of a generally chemically unstable energetic material, to a thermo-mechanical stimulus is large, which would effectively reduce the required energy to initiate a detonation. Therefore, understanding and controlling the sensitivity to detonation of energetic materials, through hot spot formation, is critical.

Energetic materials generally are comprised of a crystalline solid that is encapsulated in a polymer binder, where the crystalline solid contains the expendable energy that is released during detonation. Energetic crystals commonly used are PETN (Pentaerythritol-tetranitrate), HMX (cyclotetramethylene-tetranitramine), and RDX (Cyclotrimethylenetrinitramine) [1]. The combination of an easily deformable polymer and a generally unstable crystalline material can provide desirable thermo-mechanical behavior. The combination of polymer and crystal, a plastic explosive, furthermore, results in an energetic material that can be molded, machined, or otherwise tailored for desired applications. The polymer within an energetic material is also needed due to the lack of self-adhesion of the crystalline energetic grains.

Thermo-mechanical stimulation, due to defects, such as dislocations, voids, and cracks can cause energy to localize, which gives rise to hot spot formation within energetic materials [2-6]. A hot spot, which has achieved a critical size and temperature, causes the energetic material to deflagrate and subsequently, under specific conditions, lead to

detonation [6]. Many microstructural mechanisms and characteristics have been suggested as the underlying mechanisms in understanding how hot spots form and evolve. Some of the dominant observed microstructural mechanisms are voids (both inter-crystalline and intra-crystalline) [2, 7, 8], shear banding [9], and dislocation pile-ups [5, 10]. Studies by Borne, Mory, et al. [7] and Qui, Stepanov, et al. [11] also clearly indicate that as the porosity volume fraction increases, the sensitivity to shock initiation increases.

The myriad heterogeneous microstructural aspects that span multiple physical scales associated with energetic materials, such as grain boundaries (GBs), energetic crystals, polymer binder composition, defects, and void distributions are further complicated by dynamic pressure loading conditions. The hot spot micromechanics model developed by Wu and Huang [12] attempts to predict the formation of hot spots in drop weight experiments. This model describes the microstructure as spherical domains of energetic crystals, where the grain morphology and defects were smeared out. Whitworth and Maw[13] developed a 1D Lagrangian multi-material model to predict temperature rises in a single material with one void. Several molecular dynamics simulations have also been undertaken to study energetic materials [14-19]. However, defects such as large voids and GBs, that span the micron scale are computationally difficult to represent in molecular dynamic simulations over physically realistic time scales.

Panchadhara and Gonthier [20] utilized a mesoscale analysis to predict the effects of volumetric and surface dissipation in granular HMX. Their predictions indicate that temperature increases in the material were mainly due to plastic work heating, and the peak temperatures observed were due to frictional heating. Baer [21] developed a model to

understand the highly fluctuating stress states in energetic materials through using multiple stress jump states. A Lagrangian finite element framework has been developed that accounts for polymer binder relaxation, frictional heating, and interfacial debonding and determined that the formation of hot spots was due to frictional heating and viscous dissipation in the binder [22, 23].

Dynamic behavior can lead to microstructural failure mechanisms, such as void coalescence, crack nucleation, and subsequent crack propagation[24-28]. Identifying and understanding how cracks nucleate and propagate is essential to delineating dissipative energy and failure pathways. In crystalline-amorphous systems, cracks propagate in the crystalline phase and typically terminate at the crystalline-amorphous interface, and there is generally a material competition between dynamic crack propagation and plasticity. [29, 30]

Experimental work by Bouma et al. [24]has shown that energetic RDX crystals contain cracks and voids due to processing. Palmer and Field [26] showed experimentally that under compressive loading of HMX energetic crystals, twinning occurs, and this typically precedes crystal fracture. Sharma et al. [27] has shown that RDX energetic crystals undergo large scale nano-fracturing that breaks up crystals into nano-crystallites with sizes ranging from 500 to 20 nm for dynamic shock loading conditions. Modeling and experimental work by Bouma et al. [25] has also shown, for dynamically deformed energetic materials, that fracture and crystal debonding are major failure mechanisms. Smith and Thorpe [28] showed that fracture in the energetic material, Composition B, occurred by cracking in the RDX phase followed by cracking in the TNT matrix phase. Experimental characterization work by Voevodin and Zabinski [31] has also indicated that dynamic

fracture of crystalline-amorphous composites occurs due to cracks nucleating in the crystalline phase, and then terminating at the crystalline-amorphous boundaries. Zhang et al. [30] also demonstrated that in a crystalline Cu and amorphous system that cracks nucleate and propagate in the crystalline phase and terminate at the amorphous phase boundary. Wang et al. [29] showed that fracture in a ductile crystalline-amorphous nano-laminate occurs by cracking in the crystalline region where cracks terminate at the amorphous phase boundary.

1.2 General Research Objectives and Approach

The objectives of this research were to identify the microstructural defects and mechanisms that were associated with hot spot formation and local failure in energetic materials, and to qualify the temporal evolution of these failure mechanisms. This allows for the identification of microstructural defects and mechanisms such as voids, grain boundaries, grain morphology, grain misorientation, dislocation densities, inelastic deformation, crack nucleation, crack propagation, and interfacial effects in energetic materials to be associated with hot spot formation and local and global failure in the material.

The effects of voids, high dynamic pressure loading conditions, high dynamic strain rate loading conditions, grain boundary misorientations, crack nucleation and propagation, and viscous flow behavior in polymer binder materials were investigated by means of a crystalline plasticity finite element method which had been tailored to include the effects of thermal decomposition in energetic materials.

The microstructural mechanisms associated with hot spot formation specific to the energetic material, RDX-PCTFE, were determined. However, the effects of the PCTFE binder were studied using a hypo-elastic constitutive law, and therefore neglected the effects

of viscous deformation in polymer binders, which are typical in energetic materials. Therefore, the effects microstructural defects were investigated under the influence of a viscous binder, estane, and the mechanisms that led to hot spot formation were realized. Next, the effects of crack nucleation in an aggregate were studied to determine how intra-crystalline porosity affects crack nucleation. The mechanisms for crack nucleation on the microstructural scale were obtained for local failure of the material aggregate. Next, energetic material interfaces were studied to understand how interfaces affect crack propagation and the mechanisms by which crack arrest occurs in energetic materials.

1.3 Dissertation Organization

This dissertation is outlined as follows: Chapter 2 presents the crystalline plasticity and dislocation density formulation, the finite viscoelasticity formulation, and thermo-mechanical coupling. Chapter 3 presents the numerical method used for obtaining quantities used in the formulation presented in Chapter 2. Chapter 4 contains the results from an investigation into the effects of microstructural defects on hot spot formation in RDX-PCTFE energetic aggregates. Chapter 5 covers the investigation into the effects of a polymer binder on hot spot formation mechanisms for an RDX-Estane aggregate. Chapter 6 outlines results from an investigation into the crack nucleation behavior and mechanisms of RDX-Estane energetic aggregates. Chapter 7 outlines results on how interfaces in energetic materials are paramount to crack arrest and how GB misorientations affects crack propagation.

CHAPTER 2: Crystalline Plasticity Formulation, Finite Viscoelasticity Formulation, and Thermo-Mechanical Coupling

2.1 Multiple Slip Crystal Plasticity Kinematics

The constitutive formulation for rate-dependent multiple-slip crystalline plasticity, coupled to evolutionary equations for the dislocation densities, will be outlined below [32, 33].

The velocity gradient tensor, L_{ij} , is calculated from the deformation gradient as

$$L_{ij} = \dot{F}_{ij} F_{ij}^{-1}. \quad (2.1)$$

It is assumed that the velocity gradient can be additively decomposed into elastic and plastic parts, L_{ij}^e and L_{ij}^p . These will be further decomposed into the symmetric deformation rate tensors, D_{ij}^e and D_{ij}^p , and antisymmetric spin tensors, W_{ij}^e and W_{ij}^p , as

$$D_{ij} = D_{ij}^e + D_{ij}^p, \quad W_{ij} = W_{ij}^e + W_{ij}^p. \quad (2.2)$$

The plastic parts are related to the crystallographic slip rates as

$$D_{ij}^p = P_{ij}^{(\alpha)} \dot{\gamma}^{(\alpha)}, \quad W_{ij}^p = \omega_{ij}^{(\alpha)} \dot{\gamma}^{(\alpha)}, \quad (2.3)$$

where α is summed over all slip-systems, and $P_{ij}^{(\alpha)}$ and $\omega_{ij}^{(\alpha)}$ are the symmetric and antisymmetric parts of the Schmid tensor, defined in terms of the slip planes and directions as

$$P_{ij}^{(\alpha)} = \frac{1}{2} \left(s_i^{(\alpha)} n_j^{(\alpha)} + s_j^{(\alpha)} n_i^{(\alpha)} \right) \text{ and } \omega_{ij}^{(\alpha)} = \frac{1}{2} \left(s_i^{(\alpha)} n_j^{(\alpha)} - s_j^{(\alpha)} n_i^{(\alpha)} \right). \quad (2.4)$$

As a measure of plastic strain, the effective plastic shear slip is calculated from the plastic deformation rate tensor as

$$\gamma_{eff} = \frac{2}{3} \int \sqrt{D_{ij}^p D_{ij}^p} dt . \quad (2.5)$$

The stress is updated using the Jaumann stress rate corotational with the lattice, $\sigma_{ij}^{\Delta,e}$,

as

$$\sigma_{ij}^{\Delta,e} = C_{ijkl} D_{kl}^e, \quad (2.6)$$

where C_{ijkl} is the fourth-order isotropic elastic modulus tensor defined by

$$C_{ijkl} = \mu(\delta_{ik}\delta_{jl} + \delta_{jk}\delta_{il}) + \lambda\delta_{ij}\delta_{kl} \quad (2.7)$$

The Jaumann stress rate is related to the material stress rate, $\dot{\sigma}_{ij}$, in the reference coordinate system as

$$\dot{\sigma}_{ij} = \sigma_{ij}^{\Delta,e} + W_{ik}^e \sigma_{kj} + W_{jk}^e \sigma_{ki}. \quad (2.8)$$

Power law hardening is assumed, relating the slip rates on the various slip systems to the resolved shear stress as

$$\dot{\gamma}^{(\alpha)} = \dot{\gamma}_{ref}^{(\alpha)} \left[\frac{\tau^{(\alpha)}}{\tau_{ref}^\alpha} \right] \left[\frac{|\tau^{(\alpha)}|}{\tau_{ref}^\alpha} \right]^{(1/m)-1} \quad \text{no sum on } \alpha, \quad (2.9)$$

where $\dot{\gamma}_{ref}^{(\alpha)}$ is the reference shear strain-rate which corresponds to a reference shear stress,

τ_{ref}^α , and m is the strain-rate sensitivity parameter,

$$m = \frac{\partial \ln \tau^{(\alpha)}}{\partial \ln \dot{\gamma}^{(\alpha)}}. \quad (2.10)$$

The reference shear stress includes forest hardening associated with the immobile dislocation density, which accounts for the interaction between slip systems through the

coefficient, a_{cj} , and thermal softening through the negative thermal softening exponent, ζ , and reference temperature T_r (293 K) [34].

$$\tau_{ref}^\alpha = \left(\tau_s^\alpha + \mu b \sum_{j=1,nss} \sqrt{a_{cj} \rho_{im}^j} \right) \left(\frac{T}{T_r} \right)^\zeta \quad (2.11)$$

For high strain-rate investigations under the assumption of adiabatic heating, the temperature is updated using

$$\dot{T} = \frac{\chi}{\rho c_p} \sigma_{ij}^D D_{ij}^p, \quad (2.12)$$

where χ is the fraction of plastic work converted to heat, ρ is the mass density, c_p is the specific heat of the material, and σ_{ij}^D is the deviatoric stress.

2.2 Dislocation Density Evolution

It will be assumed that the total dislocation density can be decomposed additively into mobile and immobile components.

$$\rho^{(\alpha)} = \rho_{im}^{(\alpha)} + \rho_m^{(\alpha)} \quad (2.13)$$

During an increment of slip, mobile dislocations may be generated, immobile dislocations may be annihilated, or junctions may be formed or destroyed coupling the mobile and immobile dislocation densities, leading to the coupled differential equations governing dislocation density evolution,

$$\dot{\rho}_m^{(\alpha)} = \dot{\rho}_{generation}^{(\alpha)} - \dot{\rho}_{interaction-}^{(\alpha)} \quad (2.14)$$

$$\dot{\rho}_{im}^{(\alpha)} = \dot{\rho}_{interaction+}^{(\alpha)} - \dot{\rho}_{annihilation}^{(\alpha)}. \quad (2.15)$$

The dislocation density evolution follows the formulation of Shanthraj and Zikry [35]. Dislocation density generation is related to the distance, y_{back} , traversed by a dislocation emitted from a source with density, ρ_{source} , both related to the spacing of immobile forest obstacles, i.e., Frank Read mechanism. The average velocity of mobile dislocations, $v^{(\alpha)}$, is used to determine the generation rate as

$$\dot{\rho}_{generation} = \rho_{source}^{(\alpha)} \frac{v^{(\alpha)}}{y_{back}}. \quad (2.16)$$

The Orowan equation, $\dot{\gamma}^{(\alpha)} = \rho_m^{(\alpha)} b^{(\alpha)} v^{(\alpha)}$, allows the generation rate to be recast as

$$\dot{\rho}_{generation} = \frac{\phi \sum_{\beta} \sqrt{\rho_{im}^{(\beta)}}}{b^{(\alpha)}} \left(\frac{\rho_{im}^{(\alpha)}}{\rho_m^{(\alpha)}} \right) \dot{\gamma}^{(\alpha)}, \quad (2.17)$$

where ϕ is a geometric parameter and $b^{(\alpha)}$ is the magnitude of the Burger's vector on slip system α .

Dislocation density interaction involves the immobilization of mobile dislocation segments due to junction formation that occurs when dislocation densities on different slip systems interact. The frequencies of interaction between mobile dislocation densities on slip system α and mobile and immobile dislocations on slip system β are defined as $\rho_m^{(\alpha)} \rho_m^{(\beta)} v^{(\alpha\beta)}$ and $\rho_m^{(\alpha)} \rho_{im}^{(\beta)} v^{(\alpha)}$, where the relative velocity between the slip systems, $v^{(\alpha\beta)}$, is defined using the Orowan equation as

$$v^{(\alpha\beta)} = \frac{\dot{\gamma}^{(\alpha)}}{\rho_m^{(\alpha)} b^{(\alpha)}} + \frac{\dot{\gamma}^{(\beta)}}{\rho_m^{(\beta)} b^{(\beta)}}. \quad (2.18)$$

The length of the formed junction is assumed to be proportional to the spacing of immobile dislocations as

$$l_c = \frac{1}{\sum_{\beta} \sqrt{\rho_{im}^{(\beta)}}}, \quad (2.19)$$

and only a fraction of these junctions, f_0 , are stable. The rates of immobilization of dislocation densities on slip system α due to mobile and immobile dislocations on slip system β are therefore $f_0 \rho_m^{(\alpha)} \rho_m^{(\beta)} l_c v^{(\alpha\beta)}$ and $f_0 \rho_m^{(\alpha)} \rho_{im}^{(\beta)} l_c v^{(\alpha)}$, respectively. The rate of immobilization of mobile dislocation densities on slip system α is therefore

$$\dot{\rho}_{interaction-}^{(\alpha)} = f_0 \sum_{\beta} \left(\rho_m^{(\beta)} l_c \frac{\dot{y}^{(\alpha)}}{b^{(\alpha)}} + \rho_m^{(\alpha)} l_c \frac{\dot{y}^{(\beta)}}{b^{(\beta)}} \right) + f_0 \sum_{\beta} \rho_{im}^{(\beta)} l_c \frac{\dot{y}^{(\alpha)}}{b^{(\alpha)}} \quad (2.20)$$

The addition of immobile dislocation densities due to interactions also takes into account the possibility of dislocation interaction forming immobile junctions. Frank's rule is used to determine energetically favorable interactions for immobile junction formation. A dislocation density interaction tensor for junction formation on slip system α due to interaction of slip systems β and γ is defined as

$$n_{\alpha}^{\beta\gamma} = \begin{cases} 1 & \text{if } \mu b^{(\alpha)2} < \mu b^{(\beta)2} + \mu b^{(\gamma)2} \text{ and } b^{(\alpha)} = b^{(\beta)} + b^{(\gamma)} \\ 0 & \text{otherwise} \end{cases}. \quad (2.21)$$

The rates of junction formation on slip system α are then defined as

$$n_{\alpha}^{\beta\gamma} f_0 \rho_m^{(\beta)} \rho_m^{(\gamma)} l_c v^{(\beta\gamma)} \quad \text{and} \quad n_{\alpha}^{\beta\gamma} f_{\beta\gamma} l_c \left(\rho_m^{(\beta)} \rho_{im}^{(\gamma)} v^{(\beta)} + \rho_m^{(\gamma)} \rho_{im}^{(\beta)} v^{(\gamma)} \right) \quad (2.22)$$

for mobile/mobile and mobile/immobile interactions. The total addition of immobile dislocation densities due to interactions then becomes

$$\dot{\rho}_{interaction+}^{(\alpha)} = f_0 \sum_{\beta,\gamma} \left(\rho_m^{(\beta)} l_c \frac{\dot{\gamma}^{(\gamma)}}{b^{(\gamma)}} + \rho_m^{(\gamma)} l_c \frac{\dot{\gamma}^{(\beta)}}{b^{(\beta)}} \right) + f_0 \sum_{\beta,\gamma} \left(\rho_{im}^{(\beta)} l_c \frac{\dot{\gamma}^{(\gamma)}}{b^{(\gamma)}} + \rho_{im}^{(\gamma)} l_c \frac{\dot{\gamma}^{(\beta)}}{b^{(\beta)}} \right). \quad (2.23)$$

The interaction tensor for RDX crystals is determined using the 6 energetically favorable interactions: self-interaction, co-linear interaction, co-planar interaction, Lomer locks, glissile junctions, Hirth locks [36]. For RDX crystals, only self-interaction occurs. Table 2.1 summarizes self-interaction where a_{ij} is assumed to be 0.6 only for self interaction. Dislocation density annihilation due to recovery is modeled using an Arrhenius relationship [37] as

$$\dot{\rho}_{annihilation}^{(\alpha)} = \nu^{(\alpha)} e^{\left(\frac{-H}{kT}\right)}, \quad (2.24)$$

where the frequency of which immobile dislocations are intersected by mobile dislocations on other slip systems is related to the attempt frequency, $\nu^{(\alpha)}$, as

$$\nu^{(\alpha)} = f_0 \sum_{\beta} \rho_{im}^{(\alpha)} l_c \frac{\dot{\gamma}^{(\beta)}}{b^{(\beta)}}. \quad (2.25)$$

The activation enthalpy, H , is related to the immobile dislocation density and saturation density, ρ_s , as

$$H = H_0 \left(1 - \sqrt{\frac{\rho_{im}^{(\alpha)}}{\rho_s}} \right). \quad (2.26)$$

The annihilation rate of dislocation densities on slip system α becomes

$$\dot{\rho}_{annihilation}^{(\alpha)} = \left(f_0 \sum_{\beta} \rho_{im}^{(\alpha)} l_c \frac{\dot{\gamma}^{(\beta)}}{b^{(\beta)}} \right) e^{\left(\frac{-H_0 \left(1 - \sqrt{\frac{\rho_{im}^{(\alpha)}}{\rho_s}} \right)}{kT} \right)}. \quad (2.27)$$

The generation, interaction, and annihilation rates are then substituted into equations 2.14 and 2.15 to obtain a coupled nonlinear set of evolutionary equations for the dislocation densities. The evolutionary equations can be expressed as

$$\frac{d\rho_m^\alpha}{dt} = \dot{\gamma}^\alpha \left(\frac{g_{sour}^\alpha}{b^2} \left(\frac{\rho_{im}^\alpha}{\rho_m^\alpha} \right) - g_{minter-}^\alpha \rho_m^\alpha - \frac{g_{immob-}^\alpha}{b} \sqrt{\rho_{im}^\alpha} \right) \quad (2.28)$$

$$\frac{d\rho_{im}^\alpha}{dt} = \dot{\gamma}^\alpha \left(g_{minter+}^\alpha \rho_m^\alpha + \frac{g_{immob+}^\alpha}{b} \sqrt{\rho_{im}^\alpha} - g_{recov}^\alpha \rho_{im}^\alpha \right) \quad (2.29)$$

to delineate the dislocation activities such as generation, interaction, immobilization, and annihilation[33]. The coefficients, not known a priori, are summarized in Table 2.2. The dislocation activity is coupled to the stress response through the Taylor relationship (eq. 2.11).

2.3 Finite Viscoelasticity Formulation

The finite viscoelasticity formulation for the polymer binder used is based on the approach of Kaliske and Rothert [38]. Finite viscoelasticity is employed to account for the general viscous nonlinear behavior of estane at operating temperatures that are generally above the glass transition temperature. The glass transition temperature of estane is approximately -40°C [39], which indicates that the binder would be in a viscoelastic response state for the prescribed dynamic loading conditions that have been considered in this investigation. The finite viscoelastic constitutive model is based on a generalized Maxwell model (Figure 2.1). It is assumed that the stresses can be decomposed into deviatoric and hydrostatic components as the deviatoric component exhibits rate-sensitivity and the hydrostatic component exhibits rate-insensitivity as

$$\sigma^{n+1} = \sigma_{DEV}^{n+1} + \sigma_{HYD}^{n+1}, \quad (2.30)$$

where the superscript, n, is the current timestep.

The hydrostatic stresses are updated using finite elasticity by using the deformation-rate tensor and the Jaumann rate of Cauchy stress as

$$\hat{\sigma}_{HYD}^n = \mathbb{C}^{HYD} \cdot D^{HYD} + \sigma_{HYD}^n \cdot W - W \cdot \sigma_{HYD}^n, \quad (2.31)$$

where D^{HYD} is the hydrostatic component of the rate of deformation tensor, σ_{HYD}^n is the hydrostatic stresses at the current timestep, W is the total spin tensor, and \mathbb{C}^{HYD} is the isotropic elastic material matrix, and is given as

$$\mathbb{C}^{HYD} = \frac{3K}{1+\nu} \begin{bmatrix} 1-\nu & \nu & 0 \\ \nu & 1-\nu & 0 \\ 0 & 0 & 1-2\nu \end{bmatrix}, \quad (2.32)$$

where K is the bulk modulus, and ν is Poisson's ratio.

The deviatoric component of stress is updated by summing the contributions from each of the elements in the Maxwell model as

$$\sigma_{DEV}^{n+1} = \sigma_{0DEV}^{n+1} + \sum_{j=1}^{\# Elements} H_j^{n+1}, \quad (2.33)$$

where σ_{0DEV}^{n+1} is the deviatoric component of the lone spring in the Maxwell model, H_j^{n+1} is the viscous stress in each of the spring-dashpot elements, and j is the corresponding number associated with each spring-dashpot in the Maxwell model. The viscous stresses are updated as

$$H_j^{n+1} = H_j^n \cdot e^{-\frac{\Delta t}{\tau_j}} + \left(\frac{G_j}{G_0} \right) \cdot \left(\frac{1-e^{-\frac{\Delta t}{\tau_j}}}{\frac{\Delta t}{\tau_j}} \right) \cdot (\sigma_{0DEV}^{n+1} - \sigma_{0DEV}^n), \quad (2.34)$$

where H_j^n is the viscous stress at the current timestep, Δt is the timestep size, τ_j is the relaxation time, G_j is the shear modulus of the spring-dashpot element, G_0 is the shear modulus of the lone spring, and σ_{0DEV}^n is the deviatoric component of the lone spring at the current timestep. The deviatoric stresses in the lone spring are updated using a finite elasticity formulation as used for the hydrostatic component (equations 2.30-2.32). Time-temperature superposition is used to modify the relaxation times through the use of a shift factor, a_T , as

$$\log(a_T) = \frac{-6.5(T-T_0)}{120+(T-T_0)}, \quad (2.35)$$

where T_0 is a reference temperature and T is the current temperature.

2.4 Thermo-Mechanical Coupling

The heat generation due to mechanical energy is given as

$$q_{mechanical} = \chi \sigma'_{ij} D_{ij}^P, \quad (2.36)$$

where χ is the fraction of plastic work converted to heat, and σ'_{ij} is the deviatoric stress, and D_{ij}^P is the plastic deformation rate tensor. The heat generated due to thermal decomposition in the energetic regions can be given in terms of an Arrhenius, exothermic process [40] as

$$q_{decomposition} = \rho \Delta H Z e^{\frac{-E_a}{RT}}, \quad (2.37)$$

where ρ is the mass density, ΔH is the heat of decomposition, Z is a pre-exponential factor, E_a is the energy of thermal decomposition activation, R is the universal gas constant, and T is the current temperature. The heat generated due to viscous dissipation in the viscoelastic regions can be given by summing the viscous losses over the entire Maxwell model [41] as

$$q_{viscous} = \sum_{j=1}^{22} \frac{H_j^{n+1} : H_j^{n+1}}{4 G_j \tau_j}. \quad (2.38)$$

For high strain-rate simulations, equations (2.36 – 2.38) can then be used to determine the adiabatic temperature rate as follows,

$$\dot{T} = \frac{1}{\rho c_p} (q_{mechanical} + q_{decomposition} + q_{viscous}), \quad (2.39)$$

where c_p is the specific heat. Equations (2.36 – 2.38) can also be used as heat sources to the heat conduction equation (2.40). The mechanical energy is coupled to the thermal energy and the three internal heat generation sources as follows,

$$\rho c_p \left(\frac{\partial T}{\partial t} \right) = \lambda \nabla^2 T + q_{mechanical} + q_{decomposition} + q_{viscous}. \quad (2.40)$$

2.5 Tables and Figures

Table 2.1: Summary of interactions and coefficient values in an RDX crystal

Interaction type	Dissipation ($\propto \sqrt{a_{ij}}$)	a_{ij}
Self	$2kGb^2$	0.6

Table 2.2: Summary of g-coefficients for dislocation density evolution equations

g Coefficients	Expression
g_{sour}^α	$b^\alpha \phi \sum_\beta \sqrt{\rho_{im}^\beta}$
$g_{minter-}^\alpha$	$l_c f_0 \sum_\beta \left[\frac{\rho_m^\beta}{\rho_m^\alpha b^\alpha} + \frac{\dot{\gamma}^\beta}{\dot{\gamma}^\alpha b^\beta} \right]$
g_{immob-}^α	$\frac{l_c f_0}{\sqrt{\rho_{im}^\alpha}} \sum_\beta \rho_{im}^\beta$
$g_{minter+}^\alpha$	$\frac{l_c f_0}{\dot{\gamma}^\alpha \rho_m^\alpha} \sum_{\beta, \gamma} n_\alpha^{\beta\gamma} \left[\frac{\rho_m^\gamma \dot{\gamma}^\beta}{b^\beta} + \frac{\rho_m^\beta \dot{\gamma}^\gamma}{b^\gamma} \right]$
g_{immob+}^α	$\frac{l_c f_0}{\dot{\gamma}^\alpha \sqrt{\rho_{im}^\alpha}} \sum_\beta n_\alpha^{\beta\gamma} \rho_{im}^\gamma \dot{\gamma}^\beta$
$g_{re cov}^\alpha$	$\frac{l_c f_0}{\dot{\gamma}^\alpha} \left(\sum_\beta \frac{\dot{\gamma}^\beta}{b^\beta} \right) e^{\left(-H_0 \left(1 - \sqrt{\frac{\rho_{im}^\alpha}{\rho_s}} \right) \right) / kT}$

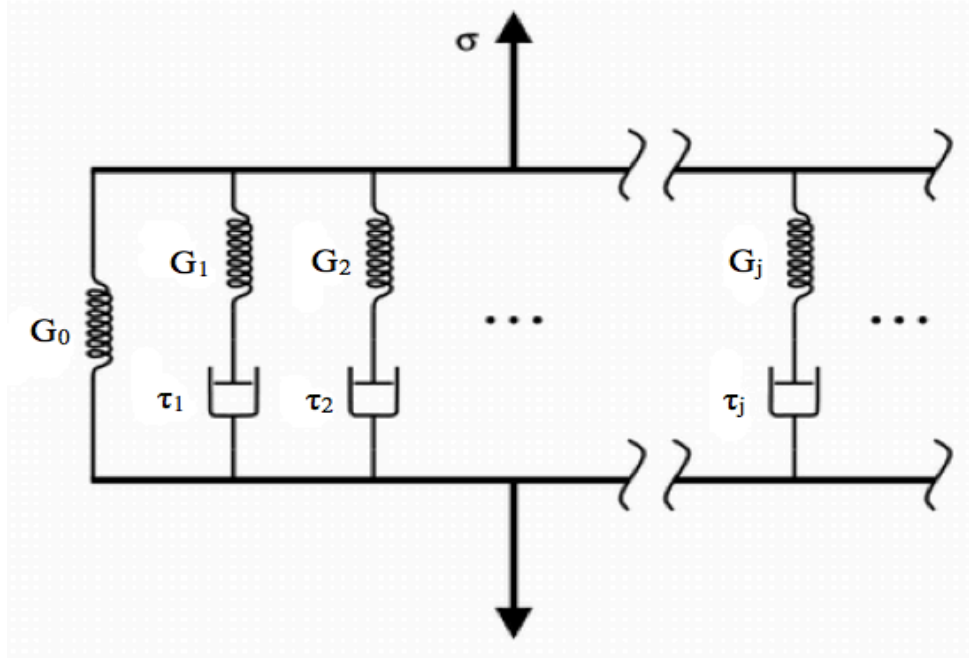


Figure 2.1: Generalized Maxwell Model for Viscoelastic Materials

CHAPTER 3: Numerical Methods

The stress state of the crystalline materials can be updated by means of the constitutive relationship prescribed in Chapter 2 once the total velocity gradient, L_{ij} , and plastic velocity gradient, L_{ij}^P , are known. The specialized finite element scheme implemented for the determination of the velocity gradient tensors will be outlined below.

3.1 Determination of the Total Velocity Gradient

The total velocity gradient can be obtained by means of finite element analysis. For quasi-static analysis, an incremental, iterative approach taking advantage of the quasi-Newton BFGS scheme is used to determine the nodal displacements. For dynamic analyses, an implicit Newmark- β , iterative approach using BFGS to solve the finite element equations linearized about t_n at each timestep is used. Trapezoidal values of $\beta = 1/4$ and $\gamma = 1/2$ were chosen for unconditional stability of the finite element method. The deformation calculated by the finite element method is used to calculate the total velocity gradient in accordance with equation 2.1.

To avoid numerical locking due to incompressible pressure constraints, 1-point integration of the Q4 quadrilateral element is used, which has the added benefit of reduced computational time. However, reduced integration can lead to the zero-energy numerical instability of hourgassing. Stiffness-based hourglass control is implemented to control the hourglass instability.

Following the method of Flanagan and Belytschko [42], an hourglass base vector $\mathbf{h}^T = [1 \ -1 \ 1 \ -1]$ is used to describe the hourglass mode for a one point integrated Q4 element. The hourglass shape vector, which is orthogonal to the linear velocity field when defined in the corotational frame, is

$$\gamma_i = \frac{1}{4} [\mathbf{h} - (\mathbf{h}^T \mathbf{x}_i) \mathbf{b}_i], \quad i = x, y, \quad (3.1)$$

where \mathbf{b}_i are the shape function derivatives, and \mathbf{x}_i are the nodal coordinates. The generalized hourglass velocity strains are given in terms of the nodal velocities, \mathbf{v}_i , as (expressed in the corotational frame)

$$\dot{q}_x = \gamma^T \mathbf{v}_x \text{ and } \dot{q}_y = \gamma^T \mathbf{v}_y. \quad (3.2)$$

For stiffness based hourglass control, generalized hourglass stress rates are defined as

$$\dot{\mathcal{Q}}_x = C^Q \dot{q}_x \quad \text{and} \quad \dot{\mathcal{Q}}_y = C^Q \dot{q}_y, \quad (3.3)$$

The stress rates are integrated and used to augment the force vector through a stabilization force,

$$\mathbf{f}^{stab} = A \begin{Bmatrix} \mathcal{Q}_x \gamma \\ \mathcal{Q}_y \gamma \end{Bmatrix} \quad (3.4)$$

where A is the element area. A corresponding stabilization augments the stiffness matrix as

$$\mathbf{K}_e = \mathbf{K}_{e,1pt} + C^Q A \begin{bmatrix} \gamma \gamma^T & \gamma \gamma^T \\ \gamma \gamma^T & \gamma \gamma^T \end{bmatrix} \quad (3.5)$$

The coefficient for the stabilization force and stiffness is defined as

$$C^Q = \frac{1}{2} \alpha_s c^2 \rho A \mathbf{b}_i^T \mathbf{b}_i, \quad (3.6)$$

where the input parameter is α_s , and c is the shear wavespeed of the material. An effective modulus is used to account for the lower wavespeed of plastic elements as follows:

$$\frac{\Delta\sigma_{ii}/3}{D_{ii}dt}; \quad \hat{\mu} = \frac{1}{2} \frac{\hat{\sigma}_{ij}^{el} D_{ij}}{D_{ij} D_{ij}}; \quad \hat{\lambda} = \hat{\kappa} - \frac{2}{3} \hat{\mu} \quad (3.7)$$

$$c = \sqrt{\frac{(\hat{\lambda} + 2\hat{\mu})}{\rho}}. \quad (3.8)$$

3.2 Determination of the Plastic Velocity Gradient

The objective stress rate is coupled with the time derivative of the resolved shear stresses to determine the resolved shear stresses on each slip plane.

$$\dot{\tau}^{(\alpha)} = \frac{d}{dt} (P_{ij}^{(\alpha)} \sigma_{ij}) \quad (3.9)$$

$$\dot{\tau}^{(\alpha)} = C_{ijkl} P_{ij}^{(\alpha)} D_{kl}^{el} \quad (3.10)$$

Eq. 3.10 can be expanded to

$$\dot{\tau}^{(\alpha)} = 2\mu P_{ij}^{(\alpha)} \left[D_{ij} - \sum_{\xi=1,nss} P_{ij}^{(\xi)} \dot{\gamma}_{ref}^{(\xi)} \left(\frac{\tau^{(\xi)}}{\tau_{ref}^{(\xi)}} \right)^{\frac{1}{m}} \right], \quad (3.11)$$

where the reference stress is a function of the immobile dislocation density. The slip rates can be determined using the resolved shear stress (equation 2.9). The plastic deformation rate tensor and spin rate tensor can then be used along with the Schmid tensor and slip rates to determine the plastic velocity gradient (equation 2.3).

The elastic spin rate tensor can be determined as a function of the total spin rate tensor and the plastic spin rate tensor using equation 2.2. It was assumed in the derivation of equation 3.11 that the time rate of change of the slip normals and directions is related to the lattice spin as

$$\dot{n}_i^{(\alpha)} = W_{ij}^{el} n_j \quad \text{and} \quad \dot{s}_i^{(\alpha)} = W_{ij}^{el} s_j. \quad (3.12)$$

3.3 Solving Systems of ODE's

The non-linear ODE's governing the resolved shear stresses and dislocation density evolution necessitate a solution method that is both accurate and stable due to their non-linear nature and the possibility of numerical stiffness [43]. The non-linear nature of the problem requires a solution method with high order accuracy, while the possibility of numerical stiffness requires a solution method that is stable and will not propagate error due to stiff behavior.

An adaptive timestep fifth-order accurate step halving Runge-Kutta method is employed. Two approximate solutions are taken using the fourth-order Runge-Kutta method, one at step length h and a second with two steps of length $h/2$.

$$\tau(t+h) = \hat{\tau}_1 + (h)^5 \phi + O(h^6) + \dots \quad (3.13)$$

$$\tau(t+2(h/2)) = \hat{\tau}_2 + 2(h/2)^5 \phi + O(h^6) + \dots \quad (3.14)$$

The two solutions are combined to yield

$$\tau(t+h) = \hat{\tau}_2 + \frac{\Delta_1}{15} + O(h^6), \quad (3.15)$$

where $\Delta_1 = \hat{\tau}_1 - \hat{\tau}_2$ is the local truncation error, which is used to measure the accuracy of the solution. If the accuracy is not less than a specified tolerance, Δ_0 , the timestep size is reduced by

$$h_{new} = F h_{old} \left| \frac{\Delta_0}{\Delta_1} \right|^{0.20}, \quad (3.16)$$

where h_{new} is the new timestep size, h_{old} is the initial timestep size, and F is used to keep the new timestep small enough to be accepted.

When the timestep is becomes excessively small, the timestep restriction can be due to stability issues caused by numerical stiffness [43]. The integration method is switched to the first-order accurate, unconditionally stable, backward Euler method,

$$\tau_{n+1}^{(\alpha)} = \tau_n^{(\alpha)} + hf\left(\tau_{n+1}^{(\alpha)}, t_{n+1}\right), \quad (3.17)$$

which is solved using quasi-Newton iteration.

3.4 Finite Element Representation of Thermal Conduction

The discretized finite element heat conduction equation is given as

$$[C][\dot{T}] + [K][T] = [R], \quad (3.18)$$

where $[C]$ is the matrix of rate of change of temperature proportional coefficients, $[\dot{T}]$ is the vector of change in nodal temperatures, $[K]$ is a matrix of temperature proportional coefficients, $[T]$ is the vector of nodal temperatures, and $[R]$ is the vector of nodal input heat sources for mechanical and decomposition energies.

The elemental matrix of rate of change of temperature proportional coefficients is given as

$$[C_{ele}] = \int [N^T][N] \rho c_p dV, \quad (3.19)$$

where $[N]$ is the vector of shape functions, and the integral is over the element volume, V .

The elemental matrix of temperature proportional coefficients is given as

$$[K_{ele}] = \int [B^T][\kappa][B] dV, \quad (3.20)$$

where $[B]$ is the strain-displacement matrix, and the integral is over the elemental volume, V .

The matrix, $[\kappa]$, is matrix of thermal conductivities and is given as the following for an isotropic material

$$[\kappa] = \begin{bmatrix} k & 0 \\ 0 & k \end{bmatrix}. \quad (3.21)$$

The vector of nodal input heat sources is given as

$$[R_{ele}] = \int [N^T] Q dV, \quad (3.22)$$

where Q is the elemental heat generation rate, and the integral is over the elemental volume, V .

The temperatures at the next time step are determined using the following equation,

$$\left(\frac{1}{\Delta t} [C] + \beta [K] \right) \{T\}_{n+1} = \left(\frac{1}{\Delta t} [C] - (1 - \beta) [K] \right) \{T\}_n + (1 - \beta) \{R\}_n + \beta \{R\}_{n+1}, \quad (3.23)$$

where Δt is the time step size, β was taken as 0.5 for Crank-Nicolson (trapezoidal) integration.

CHAPTER 4:The Effects of Microstructural Defects on Hot Spot Formation in RDX-PCTFE Energetic Aggregates

4.1 Introduction

When the thermo-mechanical sensitivity of a general chemically unstable energetic material is large, detonations can occur. Hence, understanding and controlling the detonation sensitivity of energetic materials is critical. It is, therefore, essential to predict and identify inherent dominant microstructural sources of sensitivity due to thermo-mechanical stimuli and hot spot mechanisms.

The objective of this investigation is to predict what the interrelated microstructural effects of crystal-binder interactions, void distributions, dislocation-density evolution, and GBs have on hot spot formation in aggregates subjected to high pressure loading conditions. Hence, a recently developed dislocation-density based crystalline plasticity approach [35] and specialized dynamic finite-element techniques will be used to predict and understand how dislocation-density, thermal evolution, inelastic slip behavior, and high dynamic pressures affect hot spot formation in RDX-PCTFE aggregates.

4.2 Results

Computational analyses were undertaken to investigate and predict the effects of different dynamic pressure loading conditions and GB misorientations on hot-spot formation for a RDX energetic crystalline aggregate with a polymer binder. The finite element aggregate consisted of 25 grains of RDX crystals with an average grain size of 200 μm for an

aggregate size of 1mm x 1mm (Figure 4.1). The RDX crystalline morphology was generated utilizing a Voronoi tessellation scheme. Based on Gallagher, Halfpenny, et al. [44], the RDX grains were assumed to have the following three slip systems - (010) [001], (021) [100], (02 $\bar{1}$) [100] – with material properties given by Armstrong and Elban [1]. A polymer binder of Polychlorotrifluoroethylene (PCTFE), with a volume fraction of 10%, was randomly distributed between the RDX grains. The polymer properties, which are based on measurements by Brown, Rae, et al. [45], are given in Table II. The polymer binder has been modeled as a purely elastic material with a high strength to ensure plasticity does not occur because the glass transition temperature is approximately 50°C [45], which indicates that the binder would be in the glassy state for the dynamic loading conditions that have been considered in this investigation.

Porosity in RDX crystals can be controlled by changing the crystal processing parameters, which yields many different combinations of void sizes, distributions, and overall porosity volume fractions that are possible [7, 46]. In this investigation, circular voids, with an average diameter of 15 μm and an overall porosity volume fraction of 3% were used (Figure 4.1). Symmetry boundary conditions were applied to the model for two-dimensional plane-strain loading conditions. A constant dynamic pressure load was applied on the top surface, as shown in Figure 4.1, for pressure loads that varied from 750 MPa to 1 GPa for random low (misorientations less than 15°) and random high angle GB misorientations (misorientations greater than 30°).

4.2.1 750 MPa Pressure Loading and Random Low Angle GB Distributions

For a compressive pressure of 750 MPa, at a time of 630 nanoseconds, with random low angle GB misorientations, the lattice rotation, which is a measure of geometrical softening, varied from $+60^{\circ}$ to -60° (Figure 4.2(a)) where the maximum values occurred at the periphery of the voids. The normal stress was generally compressive in the bulk of the material. There were, however, localized regions at the top and bottom surfaces of the void peripheries where tensile normal stresses occurred (Figure 4.2(b)). The stresses and pressure were normalized by the static yield strength of RDX. The pressure was nominally compressive in the bulk of the material with regions around the entire void periphery that were tensile (Figure 2(c)). The tensile normal stresses and pressures most likely occurred due to wave reflections and interactions around the void peripheries [47]. The accumulated plastic shear strain (Figure 2(d)), which is the total inelastic slip on all active systems, had also localized around the peripheries of the voids with a maximum value of 160%.

The immobile dislocation densities for the three independent slip systems in RDX are shown in Figure 4.3(a-c). The dislocation density for the (010) [001] slip system, slip system one in Figure 4.3(a), had a maximum normalized value of 350. The dislocation densities were normalized by the initial dislocation density. The dislocation densities for slip systems (021) [100], slip system two, and (02 $\bar{1}$) [100], slip-system three in Figure 4.3(b-c), have maximum normalized values of 30. This indicates that for random low GB misorientations, slip system one was clearly dominant, and plastic deformation occurred by dislocation slip primarily due to this slip system.

Figure 4.4(a) shows the spatial temperature distribution, which includes the effects of thermal conduction, plastic work, and thermal decomposition. The temperature accumulated in the intervoid regions where multiple void deformations interacted and where the shear strains have localized, and the maximum temperature in this region was 460K. Therefore, the maximum temperature rise in the aggregate was 167K (the reference temperature was 293K) in the intervoid regions. Figure 4.4(b) shows the temperature rise profile due to decomposition, which indicates that thermal decomposition had occurred for this pressure loading and GB distribution. The maximum decomposition temperature rise was 3K, which occurred at the periphery of one specific void, and the maximum adiabatic plastic work temperature (Figure 4.4(c)) was 700K. This substantiates that even at small time scales and high loading rates, the effects of thermal conduction were not negligible, because the maximum adiabatic plastic work temperature (Figure 4.4(c)) was not comparable to the maximum temperature of the aggregate (Figure 4.4(a)) that included heat conduction. If these two temperatures were of comparable magnitude, then the assumption of thermal conduction being negligible would have been physically acceptable.

The temperature and normal stress evolution, as a function of time, for the element that had the highest temperature rise is shown in Figure 4.5. This element was between two voids, where the shear strain had localized. As the plot indicates, the temperature was constant until plastic deformation occurred, and then it increased sharply to 460K over a time-span of approximately 20 nanoseconds. The normal stress in this region attained a maximum normalized compressive value of -7, the temperature increased, and the normal stress increased rapidly to a compressive value of -2. According to Bruckman and Guillet[48]

and Field, Borne, et al. [5] a hot spot can form or initiate when the heat generated due to decomposition exceeds the heat dissipated to the surroundings, thus causing a run-away temperature build-up. Therefore, based on these results, we can predict hot spot initiation when the local temperature becomes unbounded due to decomposition. For these loading conditions and GB misorientations, the temperature (Figure 4.5) was bounded, and therefore it is predicted that hot spot initiation would not occur.

4.2.2 1 GPA Pressure Loading and Random Low Angle GB Distributions

For a compressive loading of 1 GPa, at a time of 430 nanoseconds, with random low angle misorientations, the lattice rotations (Figure 4.6(a)) varied between $+60^\circ$ and -60° , where the maximum values occurred around the void peripheries. The normal stress (Figure 4.6(b)) had a maximum normalized tensile stress of 3 and a normalized maximum compressive stress of 8. The aggregate was nominally compressive, but tensile stress regions occurred at the top and bottom surfaces of the void peripheries, which, as in the 750 MPa case, was likely due to wave reflections and wave interactions around void peripheries.

Figure 4.6(c) shows the pressure distribution throughout the aggregate. The maximum normalized tensile pressure was 1.5, and the maximum normalized compressive pressure was 4.5. The maximum accumulated plastic shear strain was 100%, and it occurred adjacent and around the void peripheries (Figure 4.6(d)), and it is less than the maximum shear strain for the 750 MPa loading by approximately 60%. This decrease in plastic slip was likely due to the increased strain hardening associated with the higher dynamic loading.

The immobile dislocation density for slip system one (Figure 4.7(a)), (010) [001], attained a maximum normalized value of 160, while the dislocation densities for slip systems

two (Figure 4.7(b)), (021) [100], and three (Figure 4.7(c)), $(02\bar{1})$ [100], had maximum normalized values of 16, and the maximum dislocation densities accumulated around the void peripheries. Slip system one is clearly dominant, which as with the lower pressure case of 750 MPa, indicates that this slip-system clearly dominated the overall plastic deformation.

The temperature (Figure 4.8(a)) had a maximum value of 520K, the maximum decomposition temperature rise (Figure 4.8(b)), before becoming unbounded, was 13K, and the temperature due to plastic work (Figure 4.8(c)) was 580K. The temperature temporal evolution (Figure 4.9) in the element where the temperature was the largest remained constant until plastic deformation occurred at which point the temperature increased sharply to 520K. Then the temperature became unbounded due to thermal decomposition, and this indicated hot spot initiation. The temperature became unbounded 450 nanoseconds after the application of the compressive pressure load. The normal stress was initially zero, until the stress wave reached the critical element, at which point the stress increased to a normalized compressive value of 1.5. When the temperature increased due to plastic deformation, the stress transitioned from compressive to tensile. The hot spot formation, at this higher pressure loading case, is in contrast with the 750 MPa loading case (Figure 4.5), where the temperature was bounded, and therefore hot spot initiation would not have occurred. This would further indicate that as thermal decomposition becomes more dominant with increases in dynamic pressure loading, hot spot initiation is more likely to occur.

4.2.3 750 MPa Pressure Loading and Random High Angle GB Distributions

For a compressive loading of 750 MPa, at a time of 600 nanoseconds, with random high angle GB misorientations, the lattice rotation (Figure 4.10(a)) was bounded by +60° and -60°, similar to the low GB misorientations with a pressure load of 750 MPa. The normal stresses and pressures (Figure 4.10(b-c)) were generally compressive in the bulk of the aggregate with localized regions of tensile stresses that occurred around the void peripheries. The accumulated plastic shear strain (Figure 4.10(d)) had a maximum of 130% within localized deformation regions.

The dislocation density for slip system one (Figure 4.11(a)), (010) [001] had a maximum normalized value of 240. The dislocation density for slip system two (Figure 4.11(b)), (021) [100], had a maximum normalized value of 100, and slip system three (Figure 4.11(c)), (02 $\bar{1}$) [100], had a maximum normalized value of 26. Slip system one is clearly the dominant slip system, but slip system two had more activity in comparison with the random low angle GB case at a loading of 750 MPa, which is an indication that slip behavior is no longer dominated solely by one slip system, as was the case for the random low angle GB cases. The activation of this slip system can be an indication of larger stresses and stress gradients that cross between the binder and the RDX crystals, and these higher stresses would result in the activation of slip systems.

The maximum temperature of 550K (Figure 4.12(a)) occurred at the intervoid region as indicated in the figure. The maximum decomposition temperature rise (Figure 4.12(b)) was 77K, which occurred in the localized deformation region. The maximum temperature rise due to plastic work (Figure 4.12(c)) was 357K, which also occurred in the intervoid

localized deformation region. Based on these results, it is clear that GB misorientations affected hot spot formation since hot spot formation did not occur with lower GB misorientations for the same loading conditions. This is likely due to the possibility that slip can be impeded, and that high stresses would then occur.

The temporal evolution of the temperature (Figure 4.13) in the critical element where the temperature rise was the largest was initially constant for 450 nanoseconds at which time the temperature gradually increased until it became unbounded approximately 600 nanoseconds after the application of loading. In conjunction with the thermal buildup, the normal stress was initially zero until 200 nanoseconds at which point it increased compressively to a normalized value of 2. As the temperature increased, the normal stress transitioned from compressive to tensile. It is important to note that the temperature became unbounded 600 nanoseconds after the application of the applied load, and this would then result in hot spot initiation in the critical element.

Compared with experimental studies [2, 3, 7, 8, 11, 49], our predictions further substantiate the relation between void population, dynamic pressure loading conditions, and the sensitivity to hot spot formation. Hot spot formation would occur more rapidly with increases in incident pressure. Our predictions have indicated that at lower pressure loads, the temperature was bounded, and therefore, hot spot initiation would not occur. Conversely, for higher dynamic pressure loads, unbounded temperatures would result in hot spot initiation, and this is also consistent with the above investigations.

4.3 Summary

A dislocation-density based crystalline plasticity and specialized finite-element formulations were used to investigate hot spot formation due to dynamic thermo-mechanical loading conditions in RDX-PTCFE energetic aggregates. At a dynamic pressure load of 750 MPa, for the aggregate with low angle GB misorientations, the bulk of the aggregate was generally compressive with localized regions of tensile pressure around the void peripheries. Accumulated plastic shear strain deformation occurred in localized regions around the void peripheries, and this plastic deformation was mainly due to the dominance by one slip-system. The temperature also accumulated in regions around the voids where the shear strain had localized. For this pressure loading and GB misorientation distribution, hot spot formation did not occur since there was no extensive thermal decomposition and no unbounded increases in temperature.

For the 1 GPa loading with low GB misorientations, the shear strain deformation had also localized around the void peripheries, and the plastic deformation was also due to one dominant slip-system. The temperature built up in intervoid regions, and became unbounded due to increases in the thermal decomposition. These unbounded temperatures would result in hot spot initiation.

For the 750 MPa compressive loading with random high angle GB misorientations the shear strain localized in banded regions, and plastic deformation occurred primarily on two of the three slip-systems. The temperature accumulated in the banded deformation regions where the shear strain had localized. The temperature became unbounded, due to thermal decomposition, which would also result in hot spot initiation. Plastic deformation

occurred by the domination of dislocation-density slip on two slip systems, whereas for the low misorientation simulation, plastic deformation occurred dominantly on the first slip system. The high misorientation simulation also indicates that hot spot initiation will occur, whereas for low misorientations, hot spot initiation would not occur. The differences in sensitivity of the high and low angle GB misorientation cases indicates that an energetic material that has its loading axis oriented with more available slip systems could be used to lower the sensitivity of the energetic material to hot spot formation. The high angle GB case also indicated that high angle GBs may impede slip on a specific slip-system, which would increase local stresses, which can then activate other slip-systems.

Results from this study indicate that the interrelated effects of dynamic pressure loading, GB distributions, and void populations affect thermal decomposition and hot spot initiation. Unbounded temperatures resulted from heat released during the decomposition reaction, which was thermally activated by heat generation from plastic deformation. Hot spot formation resulted because the heat generated by plastic deformation and decomposition was greater than the heat dissipated to the surrounding material through thermal conduction. This indicates that for certain dynamic pressure loading conditions, the heat generated by plastic deformation can provide the thermal activation required for hot spot initiation by thermal decomposition.

4.4 Tables and Figures

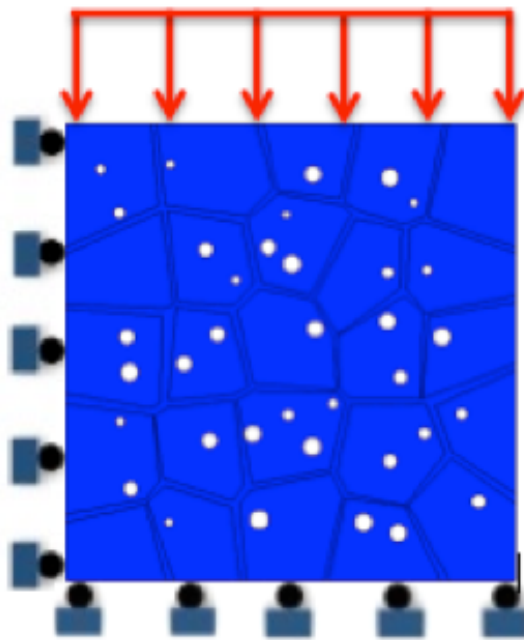


Figure 4.1: The RDX-polymer aggregate with loading, boundary conditions, and void distribution

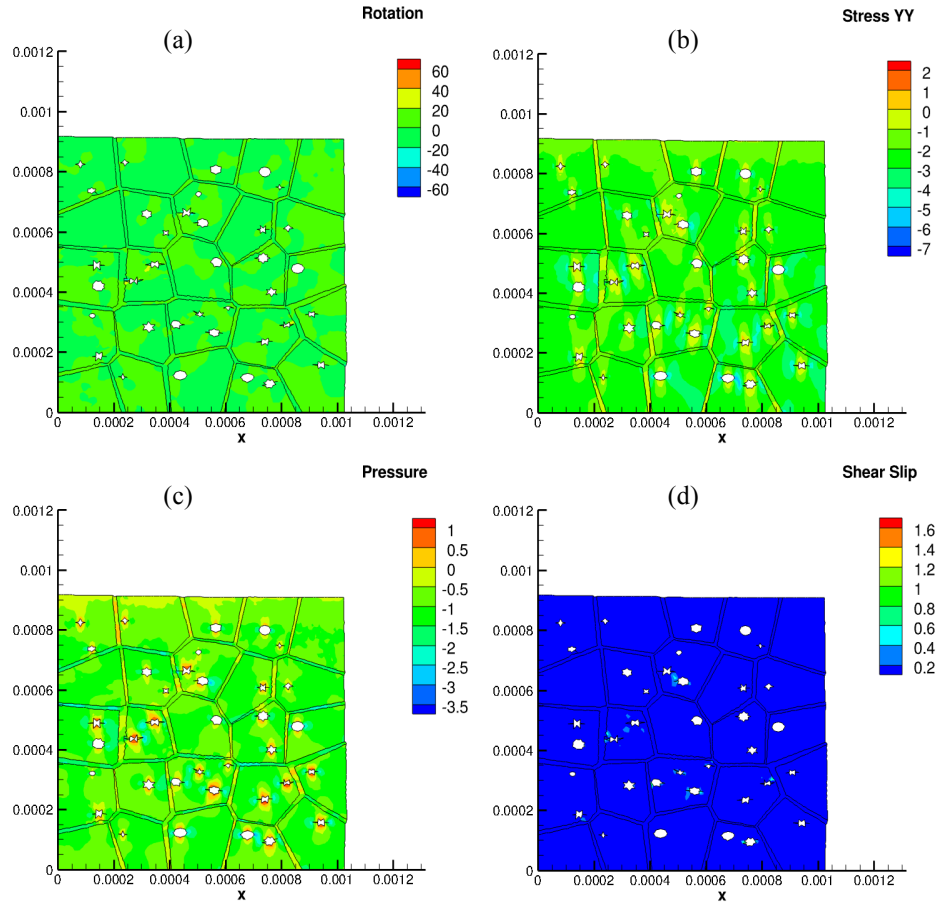


Figure 4.2. (a) Rotation, (b) Normal Stress, (c) Pressure, and (d) Accumulated plastic shear strain for a 750 MPa compressive loading with low misorientations.

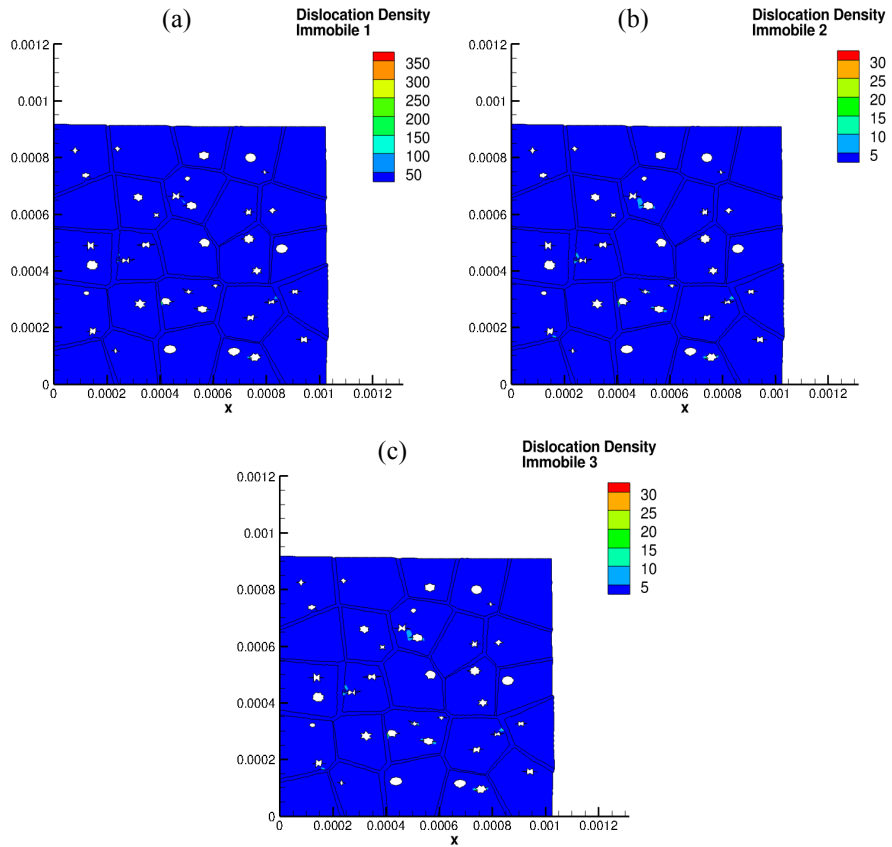


Figure 4.3. (a) Immobile dislocation density 1, (b) Immobile dislocation density 2, (c) Immobile dislocation density 3 for a 750 MPa compressive loading with low misorientations.

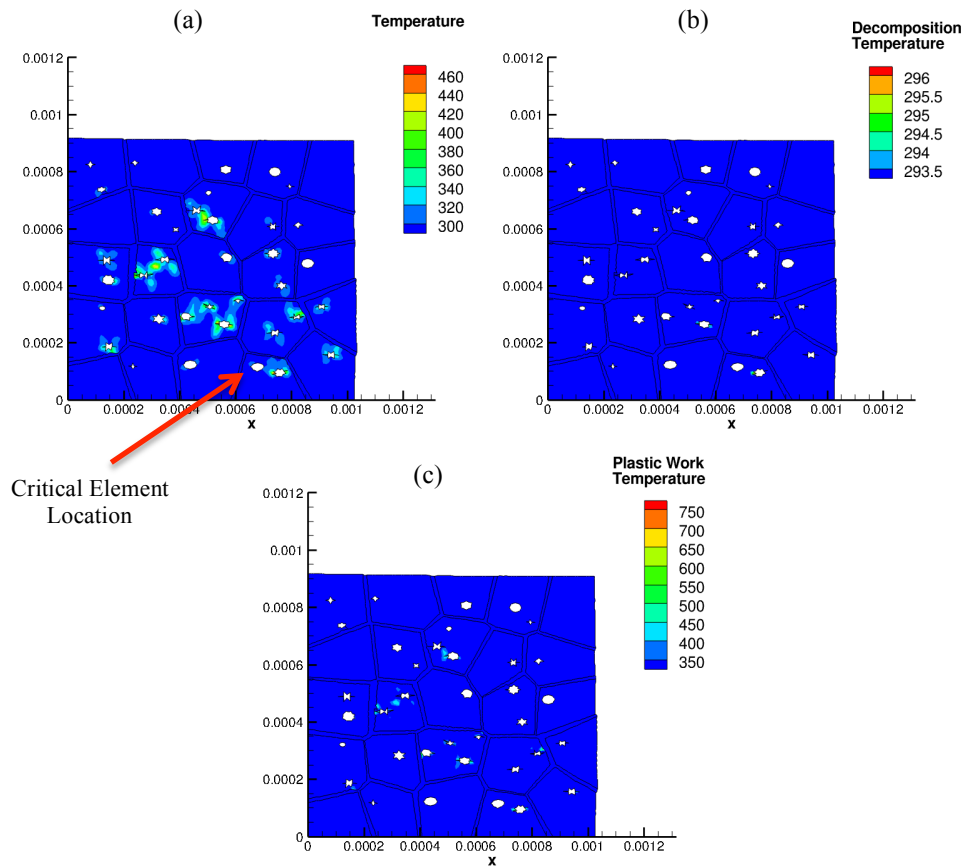


Figure 4.4. (a) Total temperature, (b) Decomposition temperature, (c) Plastic work temperature for a 750 MPa compressive loading with low misorientations.

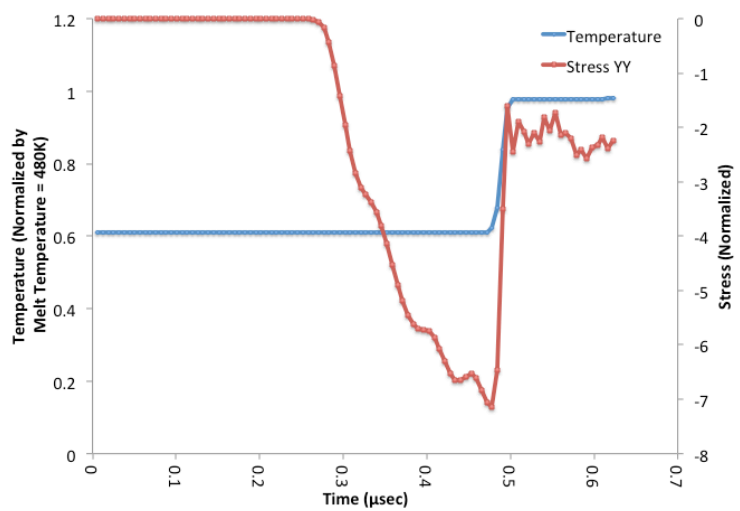


Figure 4.5. Temperature and normal stress as a function of time for a 750 MPa compressive loading with low GB misorientations.

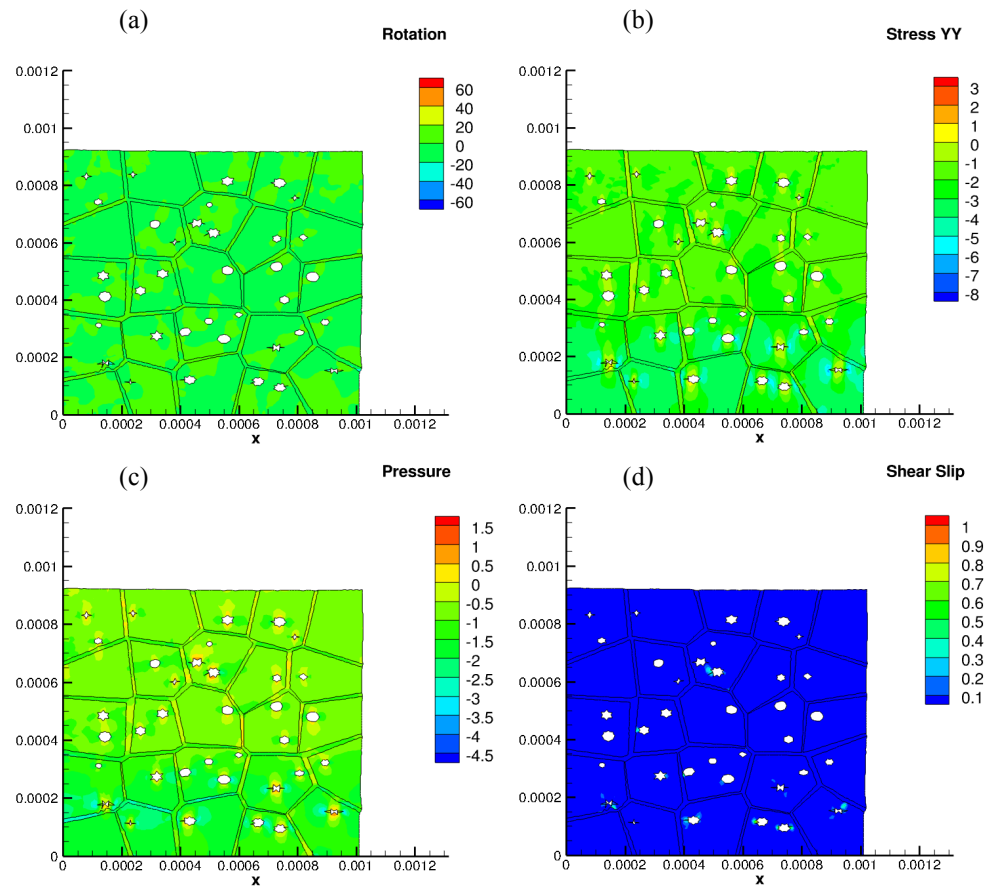


Figure 4.6. (a) Rotation, (b) Normal Stress, (c) Pressure, and (d) Accumulated plastic shear strain for a 1 GPa compressive loading with low angle GB misorientations.

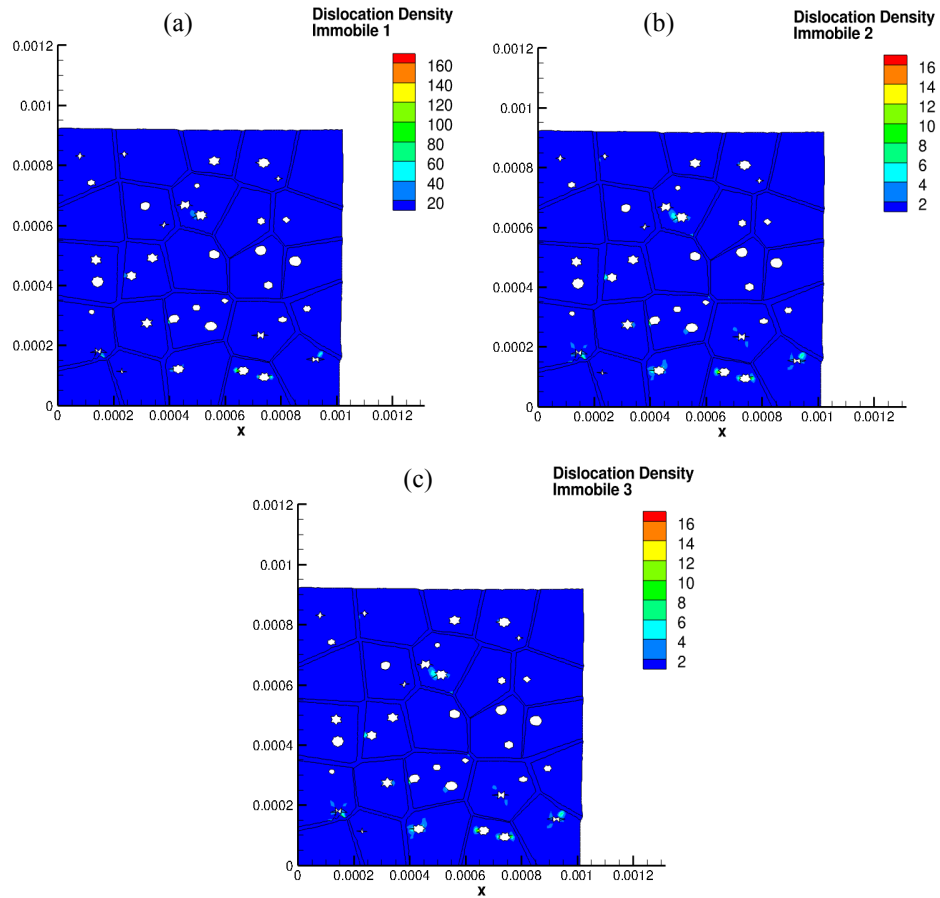


Figure 4.7. (a) Immobile dislocation density 1, (b) Immobile dislocation density 2, (c) Immobile dislocation density 3 for a 1 GPa compressive loading with low GB misorientations.

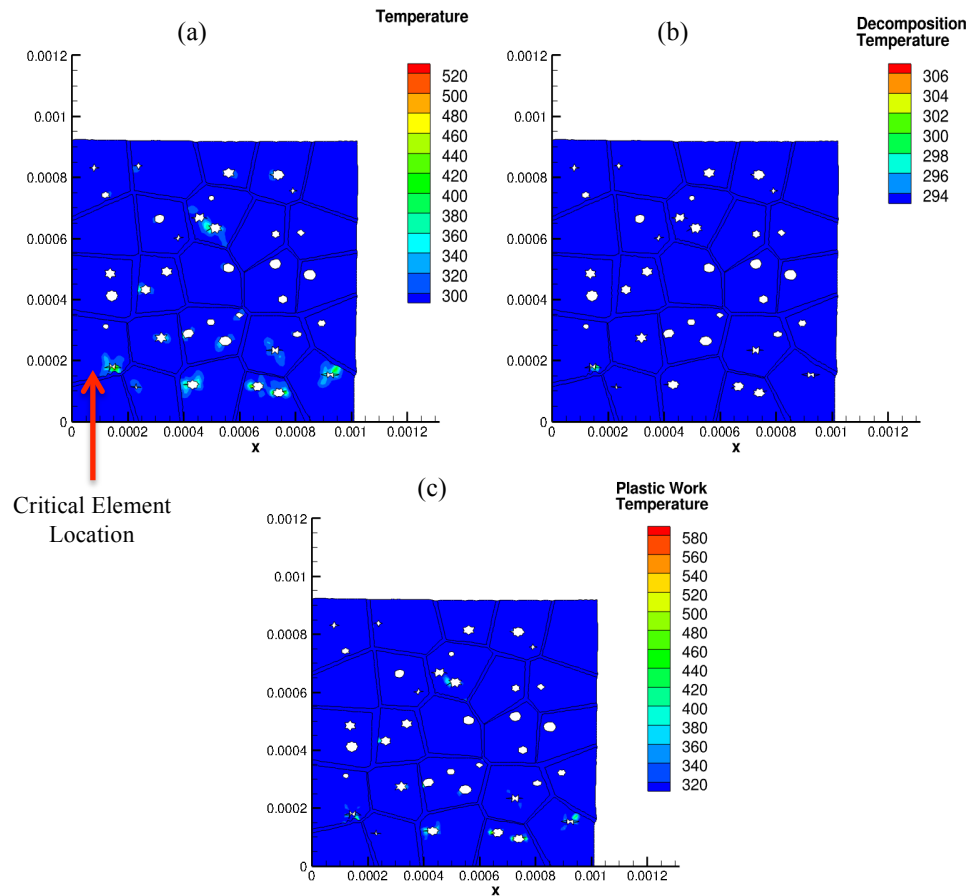


Figure 4.8. (a) Total Temperature, (b) Decomposition Temperature, (c) Plastic Work Temperature for a 1 GPa Compressive loading with low misorientations.

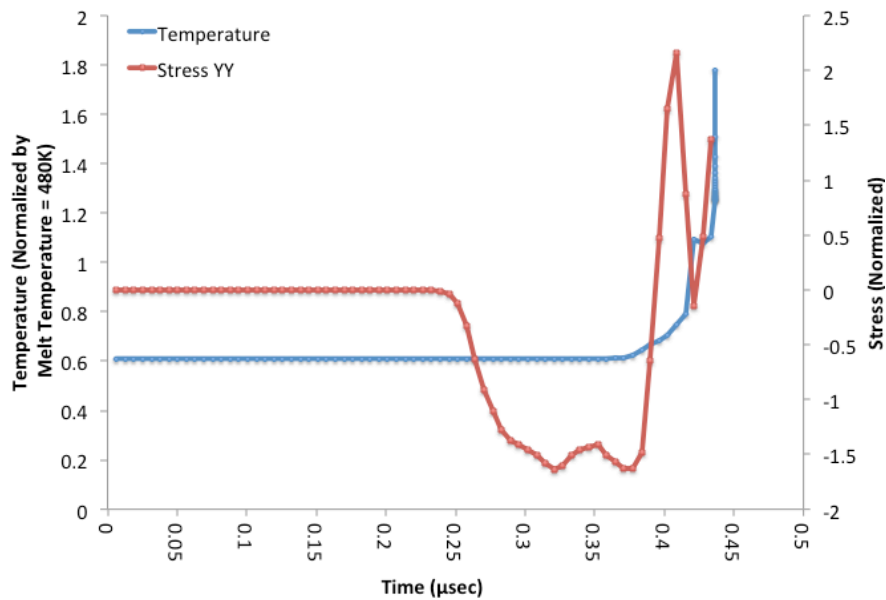


Figure 4.9. Temperature and normal stress as a function of time for a 1 GPa compressive loading with low angle GB misorientations. Hot spot initiation occurs due to an unbounded temperature caused by increases in thermal decomposition.

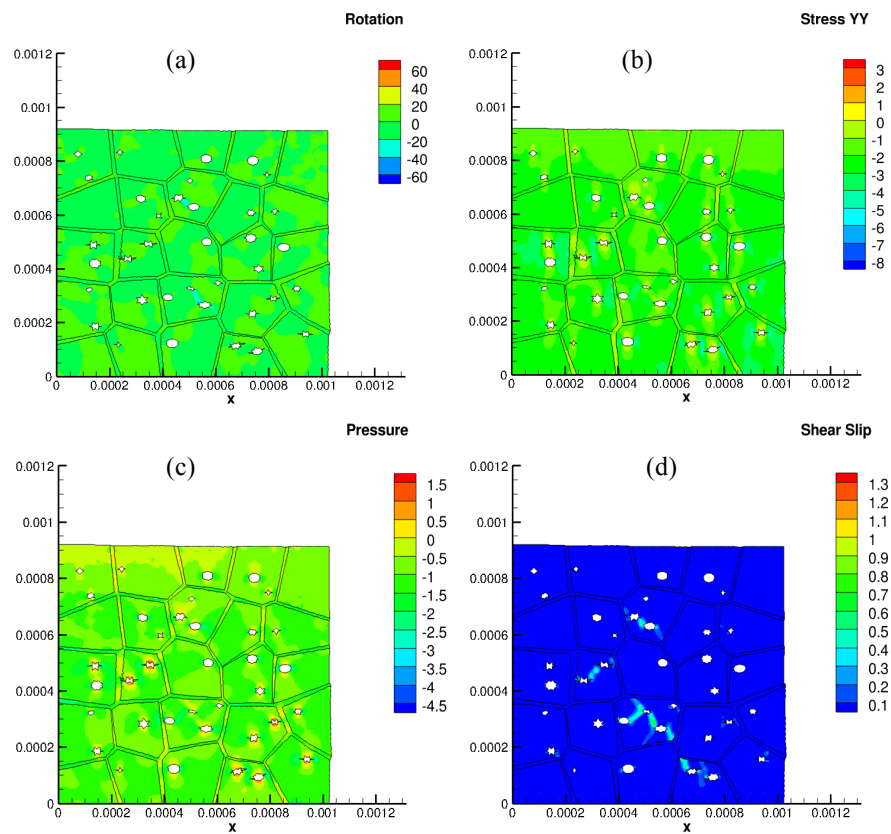


Figure 4.10. (a) Rotation, (b) Normal Stress, (c) Pressure, and (d) Accumulated plastic shear strain for a 750 MPa compressive loading with high angle GB misorientations.

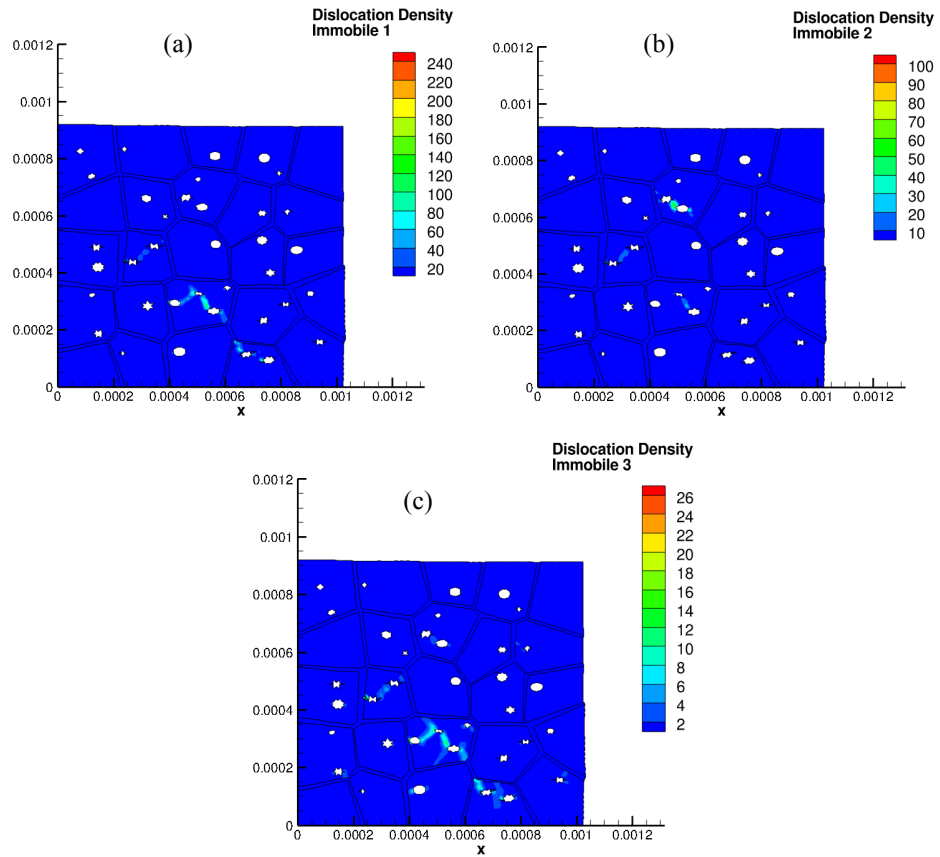


Figure 4.11. (a) Immobile dislocation Density 1, (b) Immobile dislocation density 2, (c) Immobile dislocation density 3 for a 750 MPa compressive loading with high angle GB misorientations.

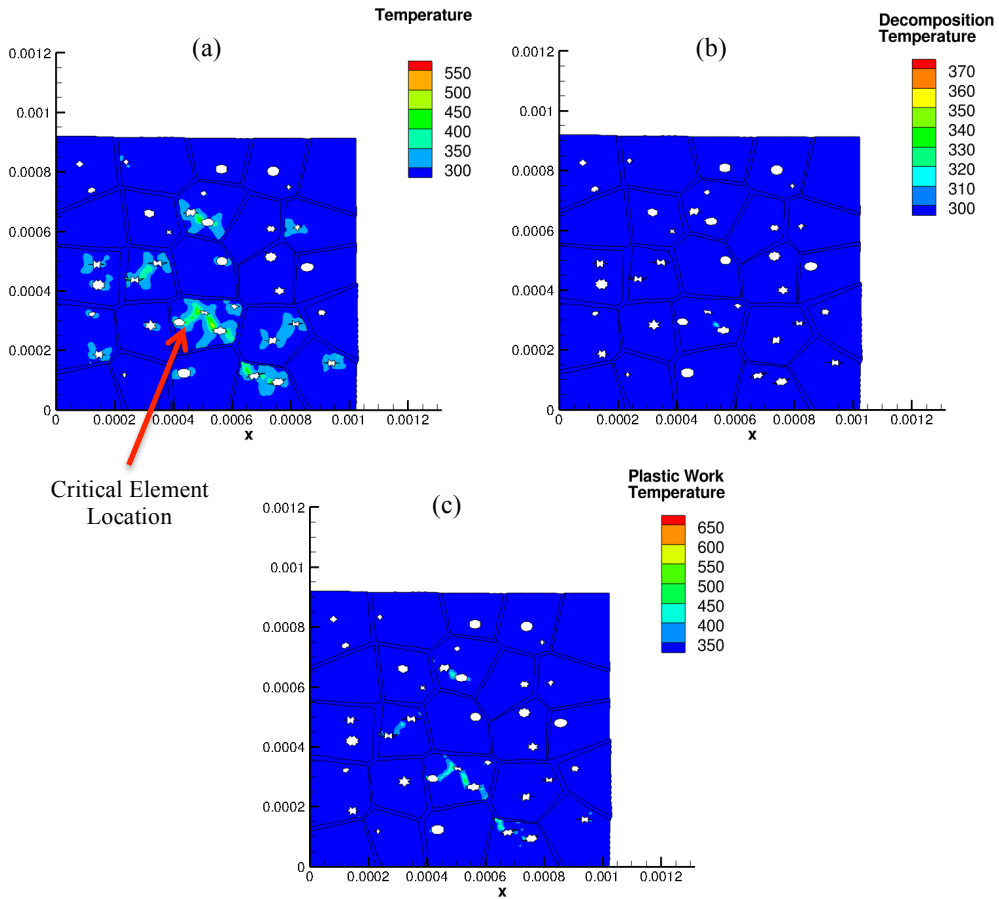


Figure 4.12. (a) Total Temperature, (b) Decomposition Temperature, (c) Plastic Work Temperature for a 750 MPa Compressive loading with high misorientations.

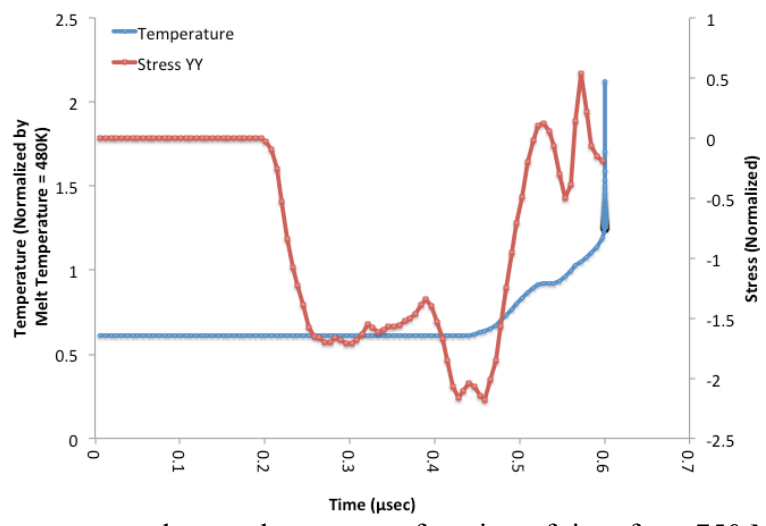


Figure 4.13. Temperature and normal stress as a function of time for a 750 MPa compressive loading with high misorientations.

CHAPTER 5: Heterogeneous Thermo-Mechanical Behavior and Hot Spot Formation in RDX-Estane Energetic Aggregates

5.1 Introduction

The heterogeneous crystalline-amorphous structure of energetic materials, the defects that span different spatial scales, and the dynamic thermo-mechanical loading conditions underscore that a fundamental understanding of behavior and hot spot formation is needed. Therefore, the objective of this investigation is to formulate a predictive framework that accounts for the interrelated microstructural effects of crystalline plasticity, polymer binder relaxation, and inherent microstructural defects and features such as void distribution, dislocation-density evolution, and GBs on hot spot formation mechanisms in aggregates subjected to high pressure mechanical loads. A recently developed dislocation-density based crystalline plasticity[35] approach, which has been coupled to a finite viscoelasticity formulation and specialized dynamic finite-element techniques will be used to predict hot spot formation mechanisms in RDX-estane aggregates.

5.2 Results

Computational analyses were undertaken to investigate and predict the effects of dynamic loading conditions on system behavior and hot spot formation for a RDX energetic crystalline aggregate with a viscoelastic polymer binder. The finite element aggregate consisted of 64 grains of RDX crystals with an average grain size of 125 μm for an overall aggregate size of 1mm x 1mm (Figure 5.1). The RDX crystalline morphology was generated utilizing a Voronoi tessellation scheme. Based on Gallagher et al. [44], the RDX grains were

assumed to have the following three independent slip systems – (010) [001], (021) [100], (02-1) [100] – with material properties given by Armstrong and Elban[1] and Annapragada et al. [50] in Table 5.1. A polymer binder of estane, with volume fraction of approximately 17%, was randomly distributed between the RDX grains. The material properties for the estane polymer binder were obtained from measurements by Mas et al. [39] and Barua and Zhou [23], as shown in Table 5.1.

Porosity in RDX crystals can be controlled by changing the crystal processing parameters, which can result in different combinations of void morphology, sizes, and distributions [7, 46]. In this investigation, circular voids, with an average diameter of 10 μm and an overall porosity volume fraction of 2.5% were used (Figure 5.1), which is consistent with energetic material microstructures [7, 46, 49, 51, 52]. Symmetry boundary conditions were applied to the model for two-dimensional plane-strain loading conditions. A constant dynamic pressure load was applied on the top surface, as shown in Figure 5.1, for a dynamic tensile pressure load of 1 GPa and a dynamic compressive pressure load of 1 GPa, with random GB misorientations of less than 15°.

5.2.1 Validation of the Viscoelastic Model

For the estane polymer binder, the model was validated with the experimental results of Mas et al. [39] for quasi-static and dynamic behavior. A pure estane model with dimensions of 1mm x 1mm was used, and symmetry boundary conditions were applied for two-dimensional plane-strain loading conditions. A constant strain rate displacement condition was applied on the top surface, as shown in Figure 5.2, for a quasi-static strain rate of 0.005 s^{-1} and a dynamic strain rate of 2000 s^{-1} .

For a quasi-static strain rate of 0.005 s^{-1} and an initial temperature of 20°C , predicted and experimental results were both non-linear (Figure 5.3a). The predicted results, at a nominal strain of 15%, were within approximately 10% of the experimental value, and the percent difference of the average stresses was 6.5%. For the dynamic strain rate of 2000 s^{-1} and an initial temperature of 0°C , the percent average difference between the experimental and predicted results was approximately 6.9% (Figure 5.3b).

The differences in the experimental results are likely due to the experimental cylindrical specimen geometry, while the analysis was for a plane strain simulation. Furthermore, the specimen size was never specified in [39], therefore, a size of 1 mm x 1 mm, that is consistent with a split Hopkinson specimen was used (see, for example[53, 54]). The viscoelastic stress evolutions as a function of strain, however, were consistent with both the quasi-static and dynamic experimental results and the average differences were less than 10%. Hence, this validation is another indication of the predictive capabilities of the computational approach.

5.2.2 Dynamic Tensile Pressure Loading of 1 GPa

Local microstructural behavior was investigated by using a 64 grain aggregate that was 1mm x 1mm, which was subjected to a dynamic tensile pressure load of 1 GPa. At a time of $.465\text{ }\mu\text{s}$, the spatial temperature distribution, which included the effects of thermal conduction, adiabatic heating, and thermal decomposition, is shown in Figure 5.4a. The temperatures accumulated at the crystal edges where the shear strains had localized, as well as in the highly sheared regions of the polymer binder, and the maximum normalized temperature in this region was 1.87 (the temperatures were normalized by the initial

temperature of 293 K). The maximum temperature rise in the aggregate was 257 K over a span of .465 μ s. The normal stress was generally tensile in the aggregate (Figure 5.4b) with a maximum normalized stress (the stresses were normalized by the yield stress) of 6. However, there were regions of compressive normal stress within the aggregate that occurred at the crystal edges and in the adjoining binder with a maximum normalized compressive normal stress of 6. The compressive normal stress at the crystal edges and binder occur due to the viscosity of the polymer, which facilitated crystal sliding and crystal interaction with other crystals. The lateral stress was generally tensile in the horizontal ligaments of binder (Figure 5.4c) with a maximum value of 4. A major region of compressive lateral stress occurred at the right edge of the model. This is due to the effects of the free boundary and associated release waves. High regions of shear stress were localized at the crystal edges and the associated binder regions that had extensively sheared (Figure 5.4d). The maximum normalized shear stress was 2.5 and the minimum value was -2.

Figure 5.5a shows the spatial distribution of dissipated energy due to plasticity and viscous effects in the polymer binder. The dissipated energy was localized at the crystal edges where the temperatures had accumulated with a maximum value of 1.8E9 joules. The hydrostatic pressure was generally tensile in the aggregate with a maximum normalized value of 3 occurring in the binder regions that were fully constrained by neighboring RDX grains (Figure 5.5b). The minimum normalized pressure of -6 occurred in the binder region that was under compression due to crystal sliding. These regions of high compressive pressure are due to the dominance of hydrostatic stress in the binder (see Equations 10 and 11). The plastic deformation, therefore, at the neighboring crystal edges, occurs due to the incompressibility

and relative ease of polymer shearing. This underscores how crystal binder interfaces play an integral role in the aggregate deformation. Crystal sliding has been shown to be important in the deformation of crystalline aggregates as predicted by Van Swygenhoven and Derlet [55] and Kim et al. [56] and this results in stress accumulations. These results, furthermore, are consistent with the computational modeling results of Barua et al. [22, 23], which indicate that hot spots occur due to intense regions of shear deformation in the binder for an HMX and estane aggregate. The accumulated plastic shear strain (Figure 5.5c), which is the total inelastic slip on all slip systems, had a maximum of 80%, which occurred at crystal edges where the maximum temperatures accumulated. This results in heat from the binder, due to viscous dissipation, diffusing into the RDX crystal and thus increasing the temperature and crystalline plastic deformation at crystal-estane interfaces.

The mobile dislocation densities for the three independent slip systems in RDX are shown in Figure 5.6 (a-c). The dislocation density for the (010) [001] slip system, slip system one (Figure 5.6a), had a maximum normalized value of 8000 (the dislocation densities were normalized by the initial dislocation density), which occurred at the crystal edges where the temperatures accumulated. The dislocation density for slip systems (021) [100], slip system two (Figure 5.6b), had a maximum normalized value of 1000 and the dislocation density for (02 $\bar{1}$) [100], slip-system three (Figure 5.6c), had a maximum normalized value of 22.

The immobile dislocation densities are shown in Figure 5.7(a-c). The dislocation density for the slip system one (Figure 5.7a) had a maximum normalized value of 800. The dislocation density for slip system two (Figure 5.7b) had a maximum normalized value of 100 and the dislocation density for slip-system three (Figure 5.7c) had maximum normalized

values of 6. This indicates that for low angle misorientations, the inelastic deformation is dominated by slip system one. Experiments by Hooks et al. [57] and Gallagher et al. [44] indicate that RDX deformation is highly anisotropic and orientation dependent. This further substantiates that for random low GB misorientations that one slip system can be the dominant slip system. Hence, for the random low GB misorientations used in this study, the predictions indicate that the primary pathway for plastic deformation is dominated by one slip system, and based on the experimental observations and measurements, this is due to the highly orientation-dependent dominance of specific RDX slip-systems.

The temperature, normal and shear stresses, and pressure temporal evolutions for the region where the temperature becomes unbounded is shown in Figure 5.8. The spatial location on this region is given in Figure 5.4a. The temperature was initially constant until plastic deformation initiated at approximately 200 ns, and then sharply increased and became unbounded at approximately 470 ns. As noted by LaBarbera and Zikry [58], this unbounded thermal increase is an indication of hot spot formation, and this is also the region where there was maximum shear strains and temperature buildup as well as viscous sliding of the estane binder. The normal stress, shear stress, and pressure increased shortly before 50 ns. Then, when the plastic deformation initiated, the normal stress, shear stress, and pressure continued to increase significantly. This large increase in temperatures leads to thermal decomposition, unbounded temperature buildup, and hot spot formation.

The experiments of Bruckman and Guillet [48] and Field et al. [59] indicate that a hot spot can form or initiate when the heat generated due to decomposition exceeds the heat dissipated to the surroundings, which results in run-away or unbounded temperatures. As also

analyzed by LaBarbera and Zikry [58], the heating due to plastic work in RDX crystals is substantial, and it can result in hot spot formation for dynamic pressure loadings, and maximum localized thermal accumulation (Figure 5.4a). The mechanism for hot spot initiation for the amorphous elastic PCTFE binder is heating due to accumulated plasticity at the peripheries of the voids, within the RDX crystals, where the shear strain localizes [58]. However, the mechanism for hot spot initiation in RDX aggregates with a viscoelastic estane binder was heating due to plasticity at the crystal edges associated with crystal sliding due to the viscoelastic shearing of the polymer binder. Grain sliding induced regions of plastic deformation at the edges of the RDX crystals, which resulted in hot spot formation at the edges of the RDX crystals. Therefore, binder composition significantly influenced the mechanism for hotspot formation, where hot spot formation occurs by shear strain localization at void peripheries with a PCTFE binder or occurred by shear strain localization at crystal edges due to crystal sliding with the estane binder. Crystal sliding is also affected by the thermo-mechanical incompatibility with RDX crystals. Dislocations at the RDX-estane interface cannot transmit from the RDX crystal into the estane binder and therefore dislocations pileup at the crystal interface. Pileups can result in an avalanche release of the dislocations and potentially form a micro-crack at the RDX-estane interface as postulated by Armstrong and Elban [1]. These dislocation-density buildups result in a buildup of normal stress and flow stress, which activates slip behavior, and then results in increased plastic accumulation at the RDX-estane interfaces.

5.2.3 Dynamic Compressive Pressure Loading of 1 GPa

For a dynamic compressive loading of 1 GPa, at a time of .346 μ s, the temperatures accumulated at the crystal edges (Figure 5.9a) due to grain sliding. The maximum normalized temperature in the aggregate was 1.97, for a maximum temperature rise of 283 K over a time span of .346 μ s, which resulted in hot spot formation in the region of largest temperature rise, which is identified in Figure 5.9a. The normalized normal stress (Figure 5.9b) was generally compressive in the aggregate with a minimum normalized value of -7. Specific regions of tensile normal stress occurred both in the polymer binder and near the edges of the RDX crystals, with a maximum normalized value of 1. This is the result of dynamic wave reflections and stress incompatibilities due to the RDX-estane interfaces. The lateral stress (Figure 5.9c) was generally compressive with a maximum compressive normalized value of -4 that occurred within different RDX crystals. The maximum normalized value of tensile lateral stress was 3, and occurred at the interfaces of the binder and the RDX crystals. The maximum values of shear stress, also occurred at the crystal-binder interfaces, and the maximum value was -4 (Figure 5.9d). The maximum normal stress occurs at the interfaces due to the viscoelastic formulation for the estane binder while the lateral stress maximum occurs at the top of the aggregate where the crystals are under tensile lateral stress.

The energy dissipated (Figure 5.10a) in the aggregate was due to plasticity as well as viscous effects in the polymer with a maximum value of 1.1E9 joules. The hydrostatic pressure (Figure 5.10b) had a maximum tensile normalized value of 1 and a maximum compressive value of -3.5. All of these values occurred at the RDX- binder interfaces. The

plastic, inelastic, shear slip (Figure 5.10c) occurred at the crystal edges and had a maximum value of 65%.

The mobile dislocation density for slip system one (Figure 5.11a) had a maximum normalized value of 3500. The mobile dislocation density for slip system two (Figure 5.11b) had a maximum normalized value of 260, which is an order of magnitude less than slip system one. The mobile dislocation density for slip system three (Figure 5.11c) had a maximum normalized value of 13, which is an order of magnitude lower than slip system two. As shown in LaBarbera and Zikry [58], low random GB misorientations cause substantial slip activity to occur on slip system one with less substantial activity occurring on slip systems two and three. The immobile dislocation density for slip system one (Figure 5.12a) had a maximum normalized value of 350, while slip system two and three (Figure 5.12(b,c)) had maximum normalized values of 2.4 and 1.2, respectively.

The temperature, normal stress, shear stress, and pressure evolution, as a function of time history, for the element that had the highest temperature rise and subsequently lead to hot spot formation, is shown in Figure 5.13. This element was located on the edge of the specified crystal as shown in Figure 5.9a. The temperature was constant until plastic deformation occurred at approximately 210 ns after application of the load, and as a result the temperature increased. At approximately 290 ns, the temperature increased sharply and within 60 ns the temperature became unbounded due to the dominant effects of thermal decomposition. The normal stress becomes highly compressive at approximately 50 ns after the initial application of loading and remains highly compressive until the temperature increased sharply, at which time it began to unload. The shear stress had a relatively low

value of approximately -1, until plastic deformation occurred and the shear stress sharply increased to approximately -4.5 at a time of 340 ns. The hydrostatic pressure was initially compressive until the temperature became unbounded, at which time the pressure transitioned from compressive to tensile in the element where the hot spot resulted. This indicates that as hot spot formation occurs there is a complex interaction with the microstructure that results in an unbounded temperature, an unloading of normal stress, a buildup of shear stress, and a transition of pressure from compressive to tensile. This also indicates that the region where the hot spot formation occurs is dominated by a buildup of shear stress.

As noted earlier for the 1 GPa tensile pressure loading case, the primary mechanism for hot spot formation was inelastic deformation from the resulting dislocation motion due to energy dissipation associated with crystal sliding. Crystal sliding was facilitated by the application of a high dynamic pressure loading, which resulted in shear deformation of the polymer binder, and therefore caused crystal sliding and crystal- estane interaction. For the tensile loading case, the time to hotspot formation was greater in comparison with the compressive loading case, which is due to the incompressibility of the polymer binder, in the compression case, resulting in RDX plastic deformation at an earlier time.

The deformation that occurred as a result of the viscoelastic polymer binder led to complex interactions at RDX crystal to binder interfaces. Figure 5.14b shows the spatial temperature and pressure distribution across the RDX crystal – binder interface that is denoted in Figure 5.14a by the thick, dark straight line. The temperature had accumulated at the edges of the RDX crystal that is in contact with the polymer binder. As a result, the

pressure is highly compressive in the RDX crystals, and it increases until the polymer binder is encountered. This increase in pressure is due to the incompressibility of the polymer material. This is the main mechanism that results in crystal sliding due to the ease of polymer shearing and incompressibility of the polymer. This indicates that relatively small regions of the polymer, which are constrained between two neighboring crystals, are unable to compress but are easily sheared, and this facilitated RDX crystal sliding. This also indicates that as the crystal slides due to incompressibility, the large pressures resulted in plastic deformation at the crystal edges, which led to temperature accumulation, and this subsequently can lead to hot spot formation. For the tensile loading case, the regions of hydrostatic compression occurred in the vertical regions of the binder ligaments (Figure 5.5b) and for compressive loading the hydrostatic compression occurred in the horizontal binder regions (Figure 5.10b). For both the compressive and tensile loading cases, the hot spot formation mechanism is due to hydrostatic pressures, which resulted in plastic deformation and unbounded temperatures. Due to the tensile pressure, there is a material competition between plastic deformation and debonding at the RDX-estane interface that could lead to further incompatibilities at binder-RDX interfaces.

5.3 Summary

A dislocation-density based crystalline plasticity, viscoelasticity, and specialized finite-element formulations were used to investigate the mechanisms for hot spot formation due to dynamic thermo-mechanical loading conditions in RDX-estane energetic aggregates. For a 1 GPa dynamic tensile pressure loading, the temperature accumulated at the periphery of a specific crystal, where the shear strains had localized at the estane-RDX interfaces. The

temperature accumulation resulted in hot spot formation at the edges of crystals. The energy due to plastic deformation localized at the peripheries of the crystals and viscous dissipation was localized in the binder regions, which had extensively sheared, and resulted in crystal sliding. Plastic deformation was dominated by one dominant slip system due to the random low GB misorientations.

For the 1 GPa dynamic compressive loading, the temperature localized at the peripheries of the crystals, where extensive plastic deformation had accumulated. Plastic deformation was facilitated by crystal sliding due to extensive shearing and the incompressibility of the estane binder. At RDX-estane interfaces that had extensively sheared, the temperature accumulated and the magnitude of temperature and pressure buildup significantly increased as the interface was approached. This increase in hydrostatic pressure was due to a combination of the relative ease of polymer shearing and incompressibility. These regions of incompressibility in the binder facilitated crystalline deformations that resulted in localized plastic deformation and hot spot formation.

The mechanisms for hot spot formation, for both compressive and tensile loading conditions, for a plastically bonded explosive at an initial temperature that is significantly above the glass transition temperature, is RDX inelastic deformations at the crystal edges and is facilitated by crystal sliding at the RDX-estane interfaces. This results in localized plastic deformation at the periphery of the crystals. This is in contrast to a plastically bonded explosive at a temperature significantly less than the glass transition temperature (see, for example [58]), where shear strain localization at the peripheries of the voids results in hot spot formation. Incompatibilities between the RDX crystal and the estane binder exist due to

dislocation-density accumulation at crystalline interfaces, and this results in a buildup of inelastic deformation at the RDX-estane interface.

Results from this study indicate that the interrelated effects of dynamic loading, polymer binder response, and void porosity significantly affect hot spot formation mechanisms. Unbounded temperatures result from localized plastic deformation and heat released due to thermal decomposition, which was thermally activated by the heat generated due to plastic deformation and viscoelastic sliding. Different polymer binders with different glass transition temperatures will affect the thermo-mechanisms for hot spot formation due to thermo-mechanical interfacial incompatibilities with RDX crystals.

5.4 Tables and Figures

Table 5.1: Material Properties of RDX and Estane binder

	RDX	Estane Binder
Density ($\frac{kg}{m^3}$)	1820	1190
Yield Stress (MPa)	580	--
Elastic Modulus (GPa)	18.4	--
Poisson Ratio	0.22	.499
Thermal Conductivity ($\frac{W}{m K}$)	0.29	0.14
Specific Heat (c_p) ($\frac{J}{kg K}$)	1260	1500
Rate Sensitivity Parameter	.01	--
Initial Mobile Dislocation Density (m^{-2})	1e10	--
Initial Immobile Dislocation Density (m^{-2})	1e12	--

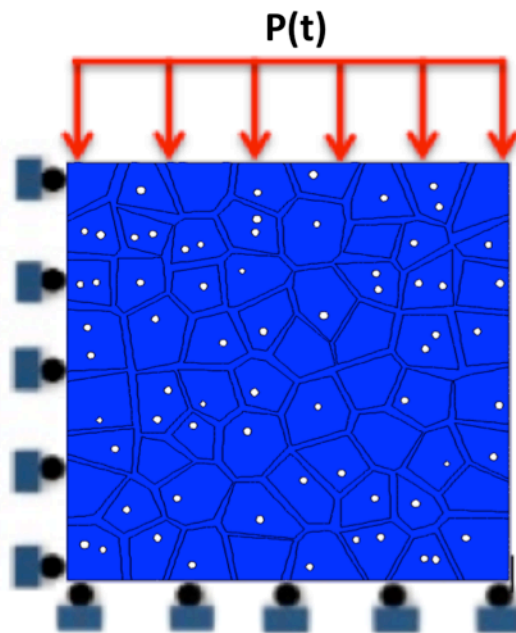


Figure 5.1: The RDX-Estane aggregate with loading, boundary conditions, and void distribution.

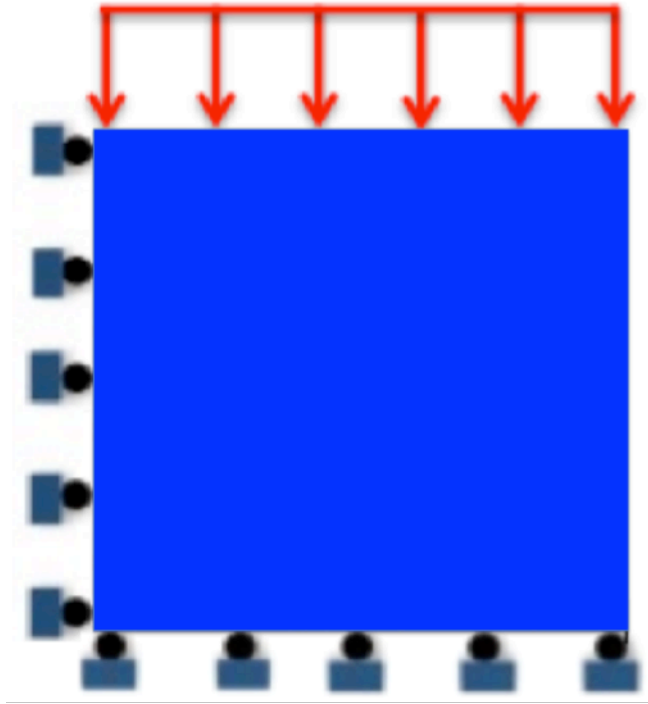


Figure 5.2: The Estane model with loading and boundary conditions used for model validation.

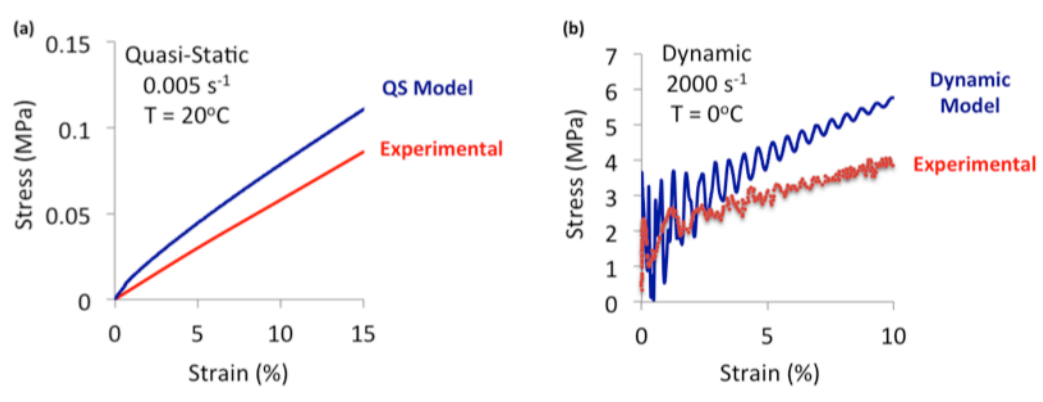


Figure 5.3: (a) Quasi-static strain rate of 0.005 s^{-1} , (b) dynamic strain rate of 2000 s^{-1} comparison of viscoelastic model with experimental data for estane.

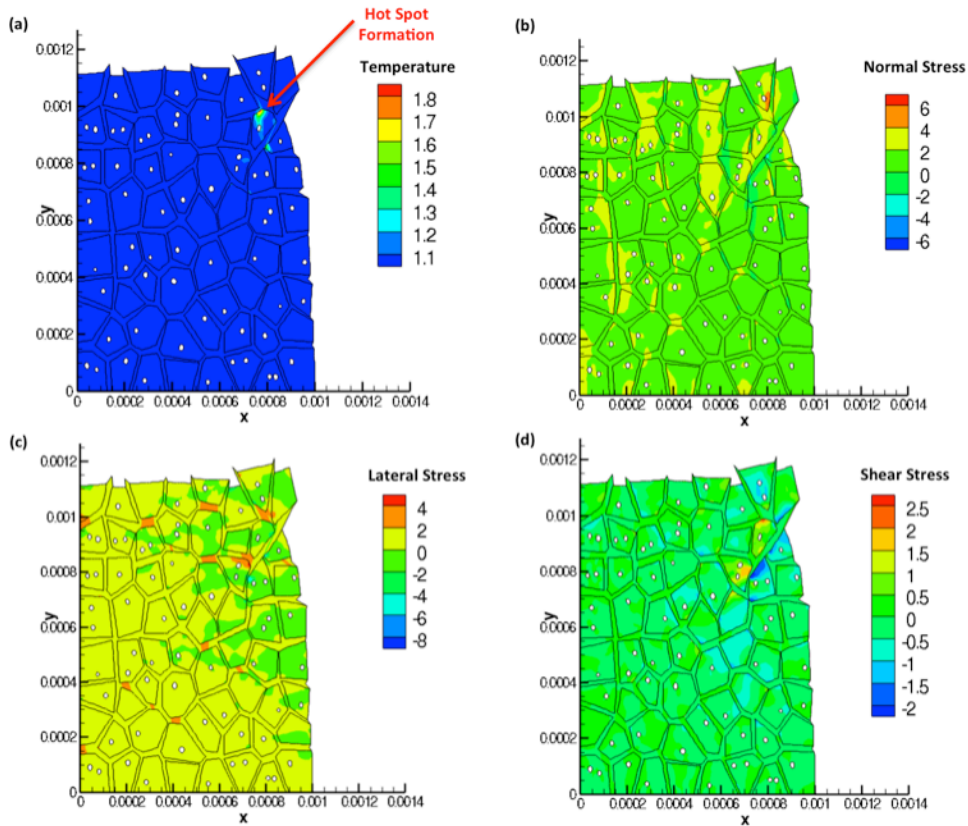


Figure 5.4: (a) Temperature, (b) normal stress, (c) lateral stress, and (d) shear stress for a 1 GPA tensile loading with low angle GB misorientations. (Spatial dimensions are in units of meters)

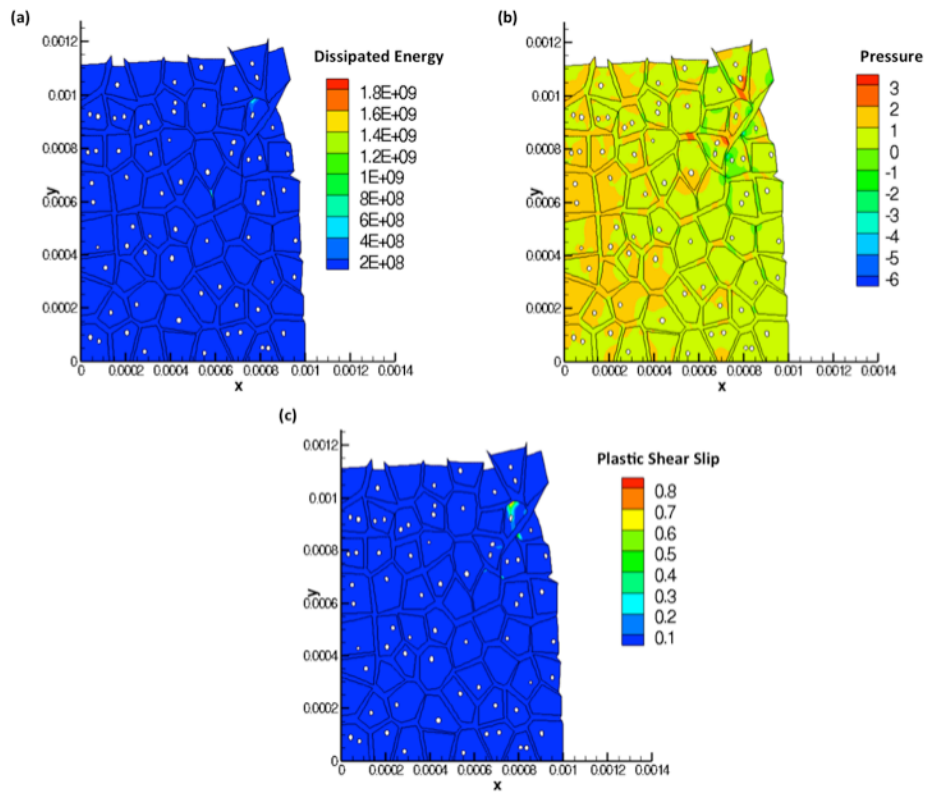


Figure 5.5: (a) Dissipated energy, (b) pressure, and (c) plastic shear slip for a 1 GPA tensile loading with low angle GB misorientations. (Spatial dimensions are in units of meters)

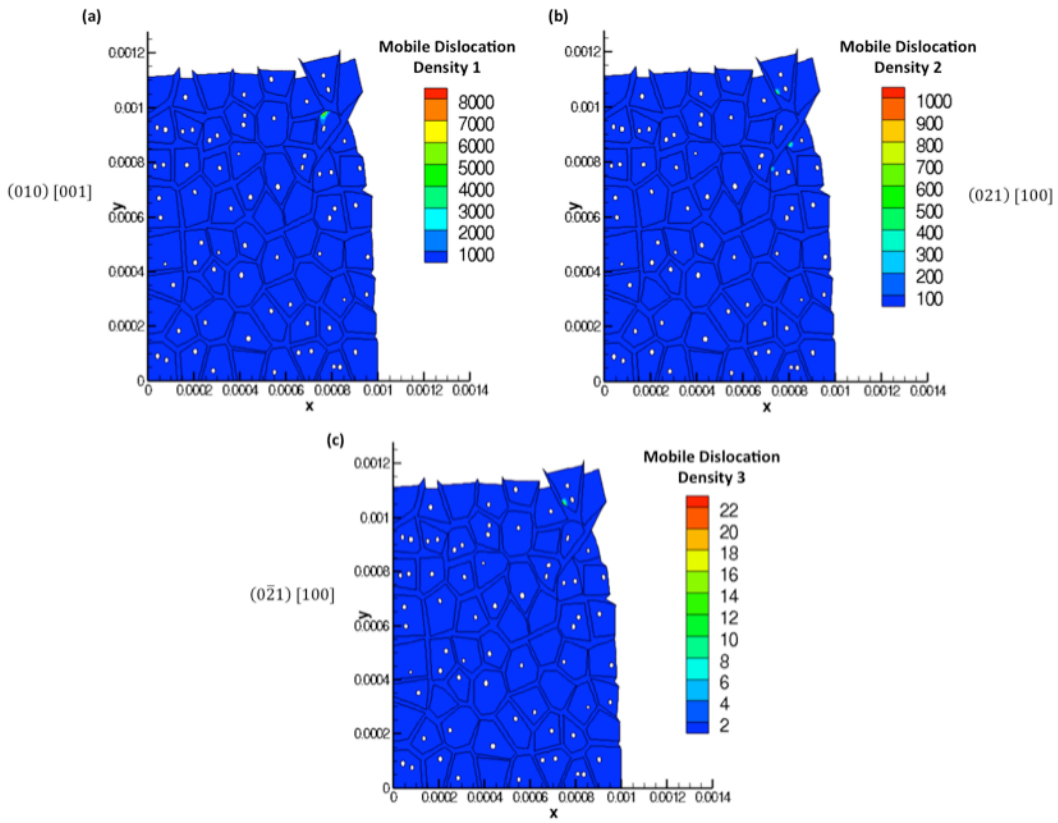


Figure 5.6: (a) Mobile dislocation density 1, (b) mobile dislocation density 2, and (c) mobile dislocation density 3 for a 1 GPA tensile loading with low angle GB misorientations. (Spatial dimensions are in units of meters)

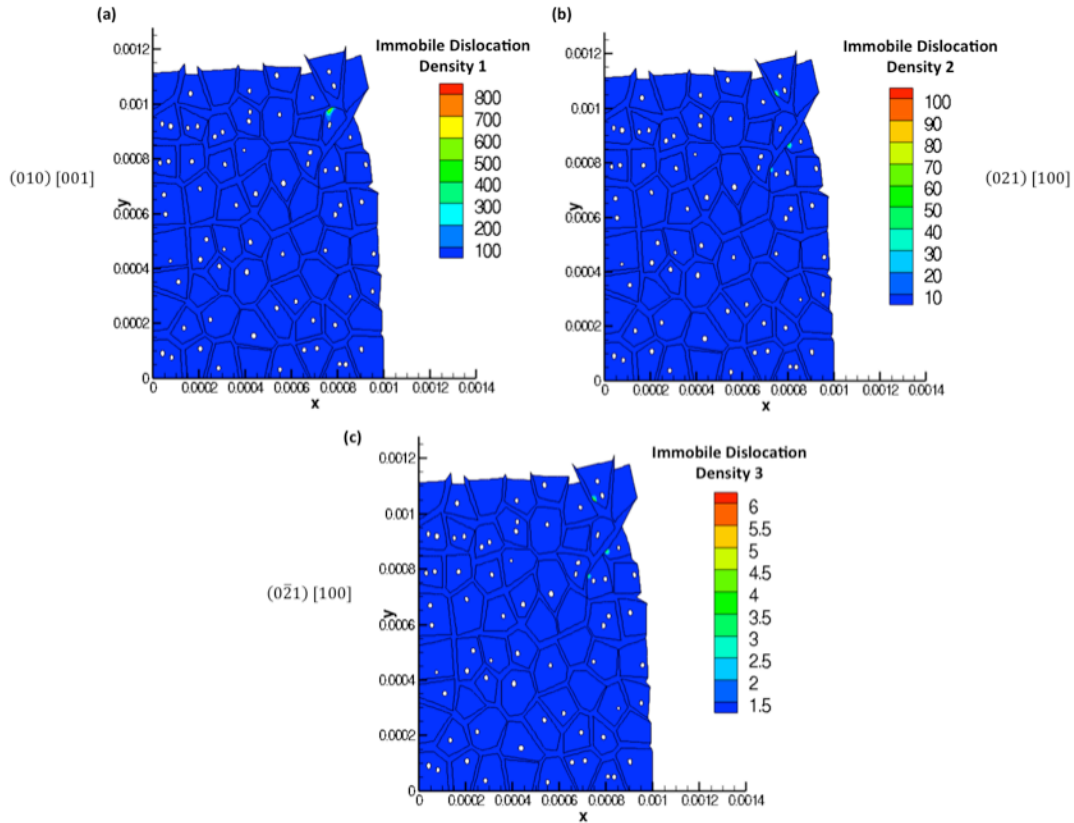


Figure 5.7: (a) Immobile dislocation density 1, (b) immobile dislocation density 2, and (c) immobile dislocation density 3 for a 1 GPA tensile loading with low angle random GB misorientations. (Spatial dimensions are in units of meters)

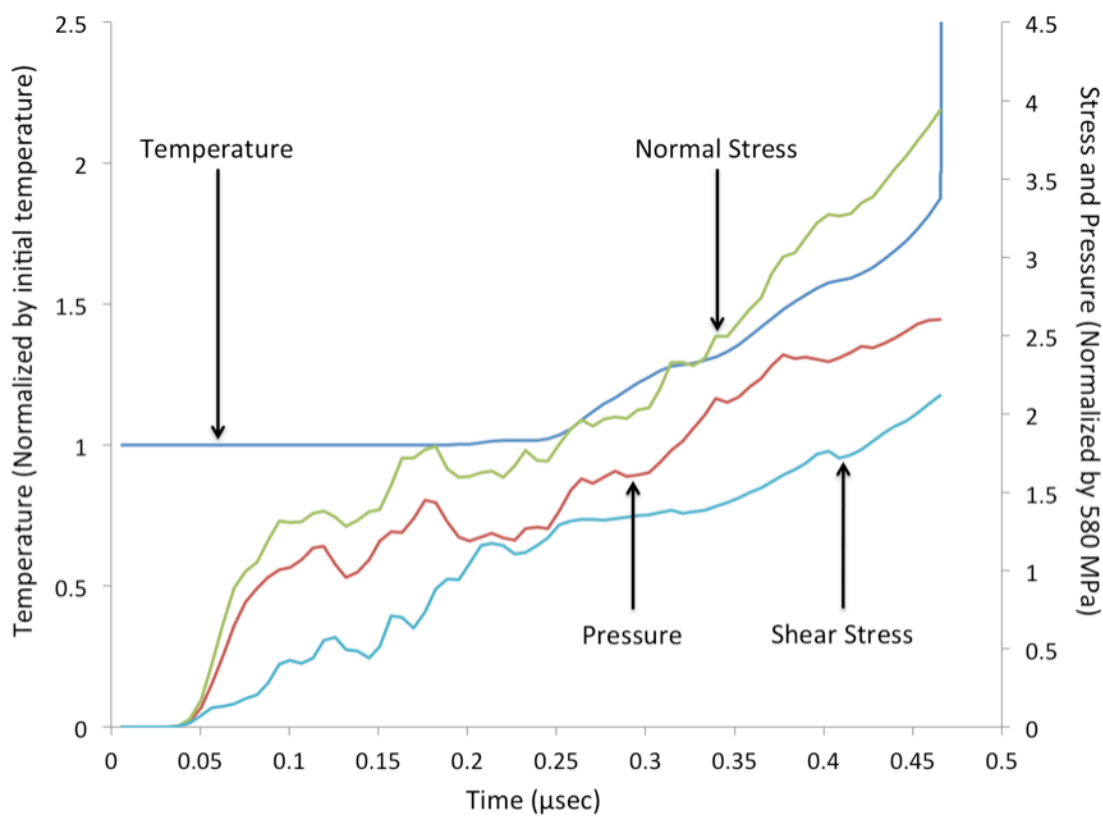


Figure 5.8: Temperature, normal stress, shear stress, and pressure time history for the region where a hotspot formation occurred for a 1 GPA tensile loading with low angle GB misorientations.

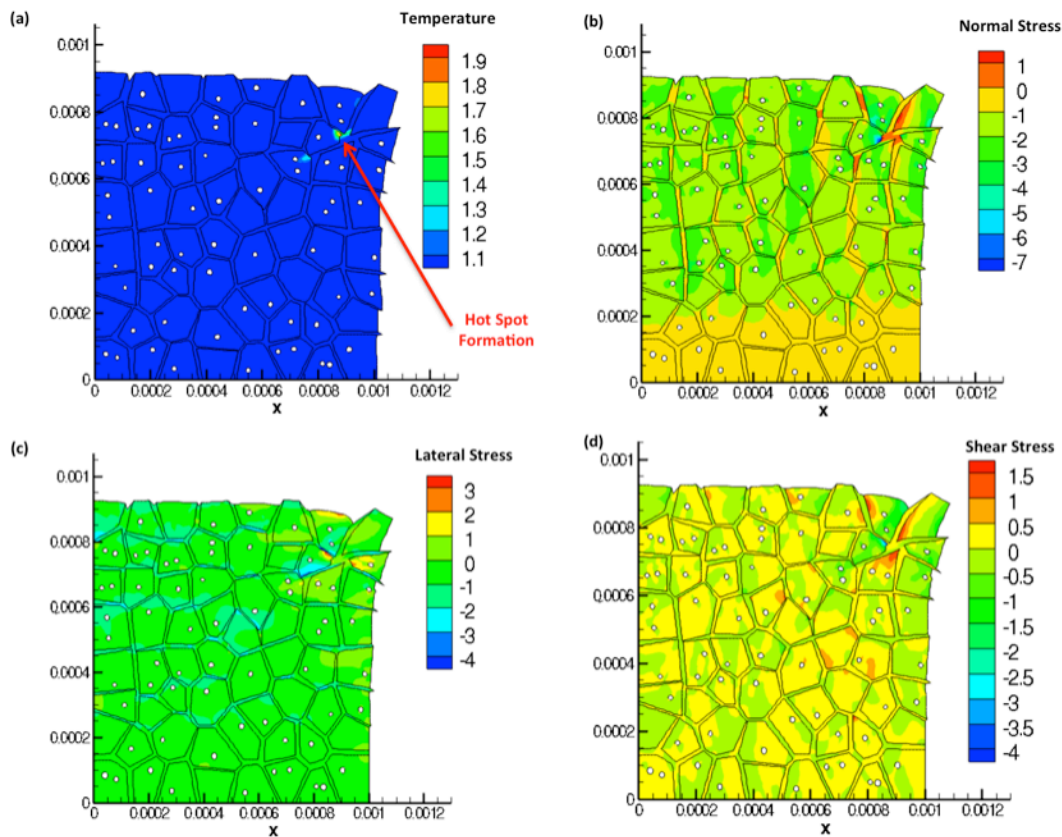


Figure 5.9: (a) Temperature, (b) normal stress, (c) lateral stress, and (d) shear stress for a 1 GPA compressive loading with low angle GB misorientations. (Spatial dimensions are in units of meters)

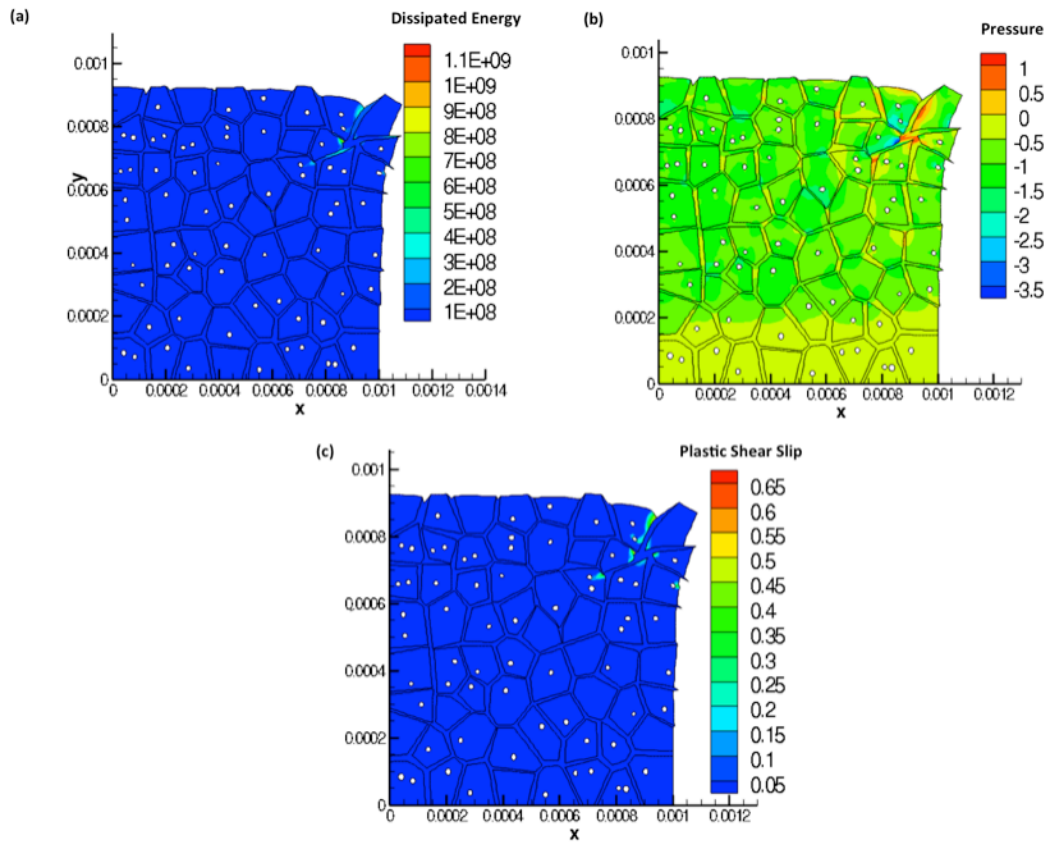


Figure 5.10: (a) Dissipated energy, (b) pressure, and (c) plastic shear slip for a 1 GPa compressive loading with low angle GB misorientations. (Spatial dimensions are in units of meters)

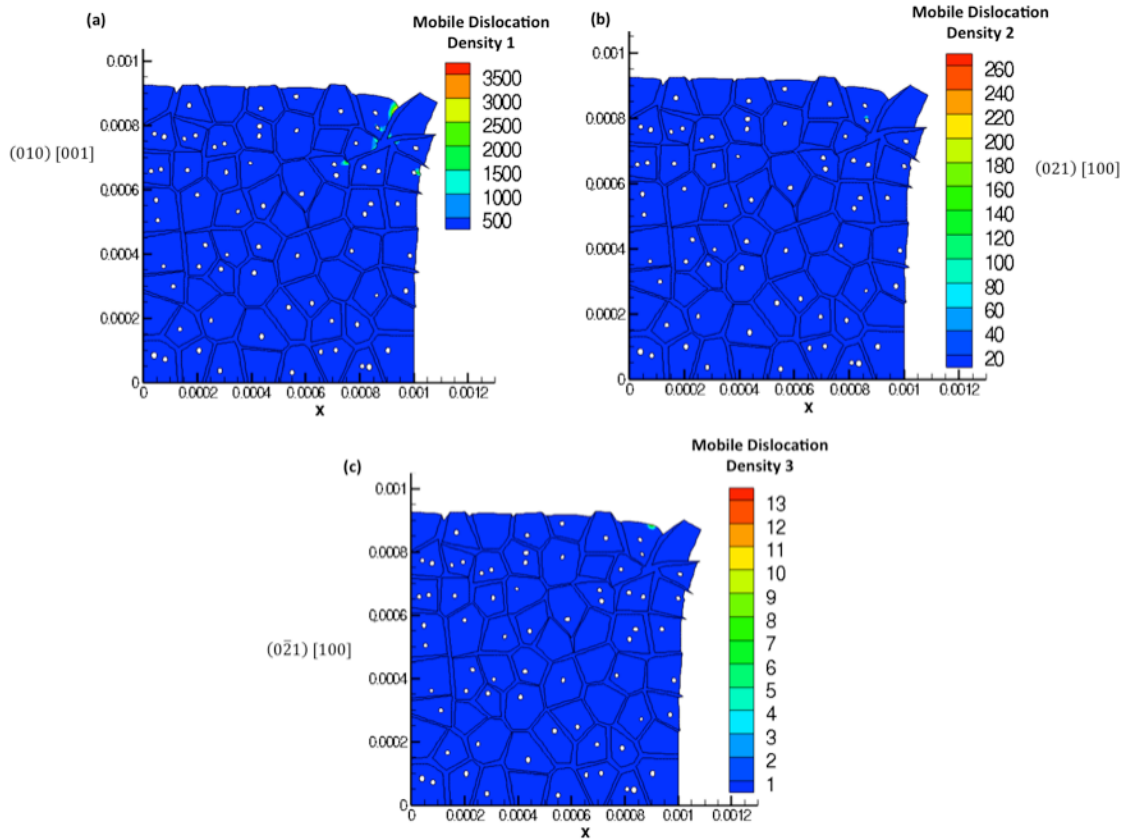


Figure 5.11: (a) Mobile dislocation density 1, (b) mobile dislocation density 2, and (c) mobile dislocation density 3 for a 1 GPA compressive loading with low angle GB misorientations. (Spatial dimensions are in units of meters)

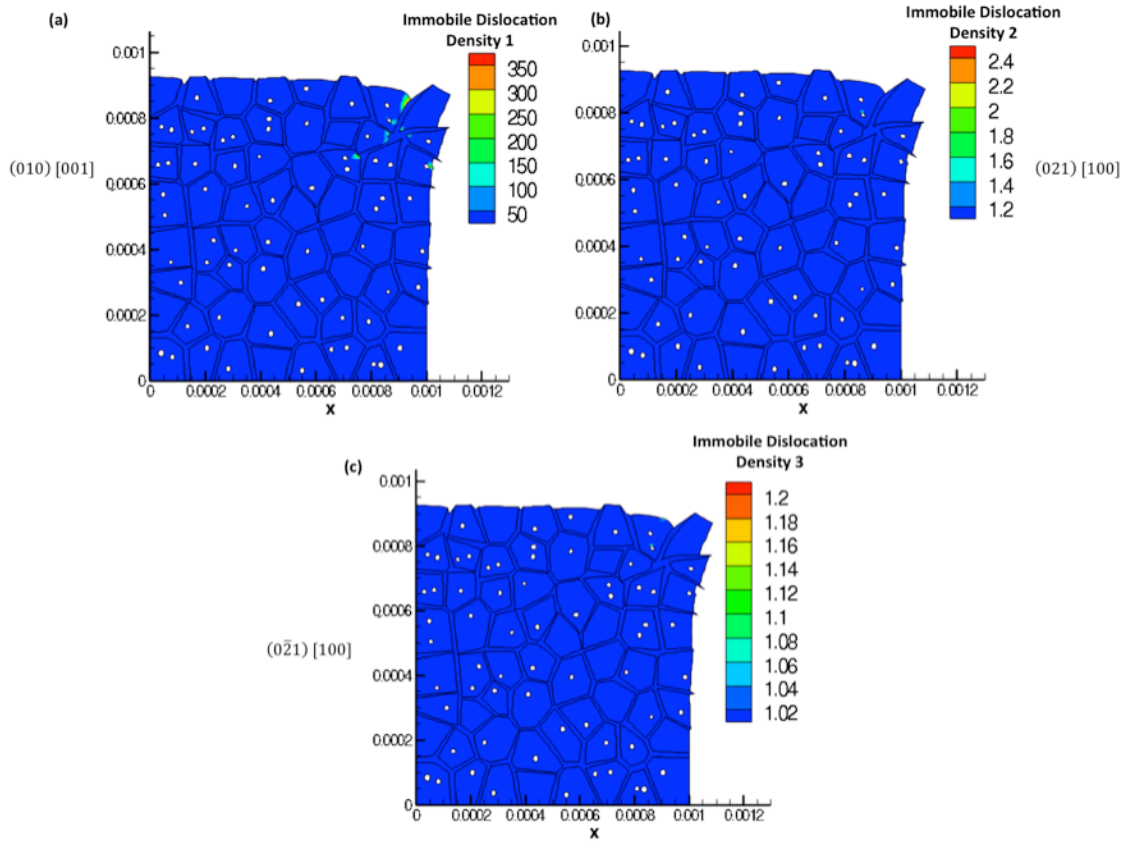


Figure 5.12: (a) Immobile dislocation density 1, (b) immobile dislocation density 2, and (c) immobile dislocation density 3 for a 1 GPA compressive loading with low angle GB misorientations. (Spatial dimensions are in units of meters)

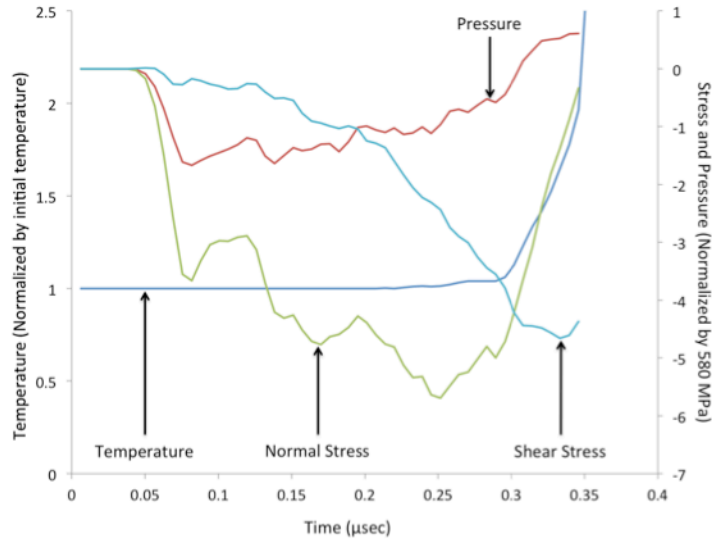


Figure 5.13: Temperature, normal stress, shear stress, and pressure time history for the region where a hotspot formation occurred for a 1 GPA compressive loading with low angle GB misorientations.

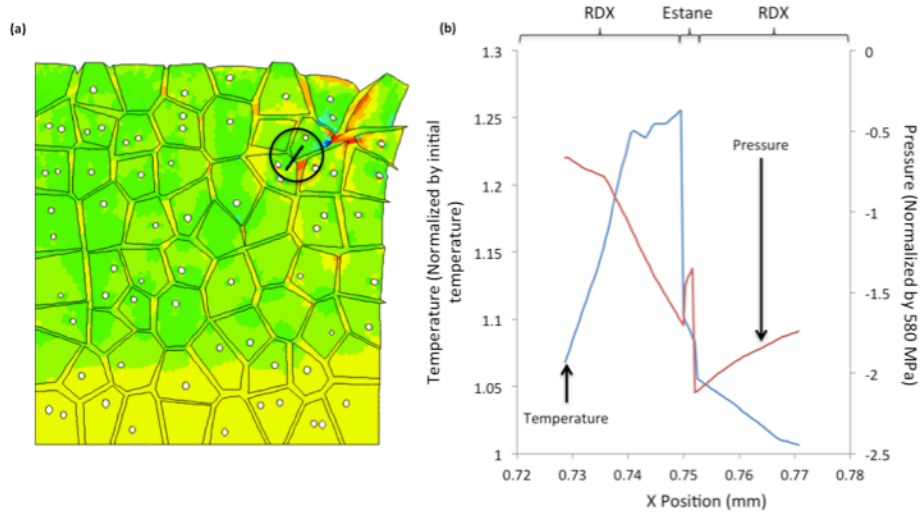


Figure 5.14: (a) The spatial location where temperature and pressure data were extracted (specifically along the straight line within the circled region) and (b) is the spatial distribution for temperature and pressure across the RDX-Estane interface.

CHAPTER 6: Dynamic Fracture and Local Failure Mechanisms in Heterogeneous RDX-Estane Energetic Aggregates

6.1 Introduction

The heterogeneous crystalline-amorphous structure of energetic materials, the defects that span different spatial scales, the fracture susceptibility of these crystalline-amorphous aggregates, and the dynamic thermo-mechanical loading conditions underscore that a fundamental understanding and prediction of local failure initiation behavior is needed. The objective of this investigation, therefore, is to formulate a predictive framework that accounts for the interrelated microstructural effects of crystalline plasticity, polymer binder relaxation, crystalline-amorphous fracture, and inherent microstructural defects and features, such as void distribution, dislocation-density evolution, and GBs on dynamic crack nucleation and growth in aggregates subjected to high strain rate loads. A recently developed dislocation-density based crystalline plasticity [35] approach, which has been coupled to a finite viscoelasticity formulation, dynamic fracture formulation, and dynamic finite-element techniques will be used to understand local failure mechanisms in RDX-estane aggregates.

6.2 Results

Computational analyses were undertaken to investigate and predict the effects of dynamic strain rate loading conditions on crack nucleation behavior and local failure for a RDX crystalline aggregate with a viscoelastic polymer binder. The finite-element aggregate of 100 grains of RDX crystals with an average grain size of 200 μm for an overall aggregate size of 2mm x 2mm (Figure 6.1) consisted of 13,382 quadrilateral elements.

The RDX crystalline morphology was generated utilizing a Voronoi tessellation scheme. Based on Gallagher et al. [44], RDX grains were assumed to have the following three independent slip systems – (010) [001], (021) [100], (02-1) [100] – with material properties given by Armstrong and Elban[1] and Annapragada et al. [50] in Table 6.1. A polymer binder of estane, with a volume fraction of approximately 19%, was randomly distributed between the RDX grains. Material properties for the estane polymer binder were based on measurements by Mas et al. [39] and Barua and Zhou [23], as shown in Table 6.1.

Porosity in RDX crystals can be controlled by varying crystal processing parameters, which can result in a vastly different combination of void morphologies, sizes, and distributions [7, 46]. In this investigation, circular voids, with an average diameter of 15 μm and an overall porosity volume fraction of 2.5% were used (Figure 6.1), which is consistent with energetic material microstructures [7, 46, 49, 51, 52]. The domain of influence radius for fracture nucleation was set to 15 μm . The fracture stress was set to approximately three times the yield stress of RDX for both RDX and estane binder. Fixed boundary conditions were applied to the model bottom for two-dimensional plane-strain loading conditions. A tensile velocity was applied on the top surface, as shown in Figure 6.1, for dynamic nominal strain rates of 1,000 s^{-1} and 10,000 s^{-1} , with random GB misorientations of less than 15°.

6.2.1 1,000 s^{-1} Nominal Strain Rate

For a nominal strain rate of 1,000 s^{-1} at a nominal strain of 9%, the maximum normalized normal stress (Figure 6.2a) was 5 (stresses were normalized by the static yield strength of RDX), which occurred at the interface of the RDX-estane where a crack had nucleated from the adjacent void periphery and subsequently propagated towards the

interface and then was arrested. The normalized normal stress was a minimum of -2, which occurred in the thin ligaments of binder that were under hydrostatic compression. From the normal stress spatial distribution in Figure 6.2a, multiple cracks have nucleated at the peripheries of the voids where the cleavage stresses were large and subsequently several of these cracks propagated to the estane binder where the cracks were arrested, which is consistent with experimental results [29-31]. The lateral stress (Figure 6.2b) had a maximum normalized value of 2.5, which occurred in the horizontal ligaments of the binder due to large tensile pressures in the binder and had a minimum of -4. The shear stress (Figure 6.2c) had a maximum normalized value of 1.2 and a minimum of -1.8, which both occurred at the corners of specific crystals that had undergone extensive shearing (Figure 3c) in the polymer binder. The hydrostatic pressure (Figure 6.2d) had a maximum normalized value of 2.2 and a minimum of -1.6 which both occurred in the binder ligaments due to the bulk incompressibility of the binder under hydrostatic conditions.

The temperature spatial distribution (Figure 6.3a) had an accumulation of temperatures at the peripheries of the crystals for a maximum normalized value of 1.22 (temperature was normalized by the initial temperature of 293 K). This buildup of temperature is due to the combined effects plastic work dissipation and thermal decomposition. The maximum buildup of thermal accumulation was located at the periphery of the specific grain shown in Figure 6.3c and had localized due to the competition between crack tip propagation and crack arrest at the interface which resulted in a large buildup of temperature. The interaction of crack-tip propagation and crack arrest is consistent with experimental results[29-31]. The shear slip, which is the sum of the plastic strains on all slip

systems, had localized in similar regions as the temperature accumulations had and was a maximum of 22%. Figure 6.3d shows the dissipated energy due to plastic work and viscous dissipation, where the maximum energy dissipated was approximately 2E8 joules and occurred at the same spatial location as the largest temperature accumulation.

The mobile dislocation densities for slip system one (Figure 6.4a), (010) [001], which was the most active slip system, had a maximum normalized accumulation of 1000. The dislocation densities were normalized by the initial density values. The buildups occurred at the peripheries of the crystals where the shear strains had localized. The immobile dislocation densities for slip system one (Figure 6.4b), (010) [001], had a maximum normalized value of 100 which also occurred at the periphery of a specific crystal.

Due to the material competition between crack propagation and crack arrest at the interface, a large buildup of temperature occurred at the interface as shown in Figure 6.3c. Therefore, the normal stress, pressure, shear stress, lateral stress, mobile dislocation density, and immobile dislocation density time history evolution for the interface-crack interaction region shown in Figure 6.3c is given in Figure 6.5. The normal stress, pressure, shear stress, and lateral stress increased linearly, in magnitude, for a time of approximately 85 μ sec. At which time a crack nucleated at the nearby void periphery and subsequently began to propagate towards the interface at a time of approximately 90 μ sec, which marked a sharp increase in the normal stress, pressure, shear stress, and lateral stress. The mobile and immobile dislocation densities were constant until a time of approximately 90 μ sec, when the crack propagated to the nearby interface and then the mobile dislocation densities increased sharply to 260 (the dislocation densities were normalized by the initial density values) and

the immobile dislocation densities increased sharply to approximately 25. The sharp increase in normal stress, pressure, shear stress, lateral stress, mobile dislocation density, and immobile dislocation density, at a time of approximately 90 μ sec is due to the interaction of the crack tip propagating to the interface and impeding further propagation due to the low stress barrier in the polymer binder, this subsequently resulted in a buildup of mobile and immobile dislocation densities at the interface. This crack tip interaction with interfacial regions underscores how crack arrest can be affected by the low stresses in the polymer regions as experimentally observed [27-31].

The stress-strain curve for a nominal strain rate of 1,000 s^{-1} is shown in Figure 6.6. The stress linearly increased with strain until a nominal strain of 7.5%, at which point the stress is approximately 0.95 (stress has been normalized by the static yield stress of RDX) and begins to unload due to localized plasticity and crack nucleation, which are both local failure mechanisms within the aggregate. Small dynamic oscillations in the stress-strain curve occurred at low nominal strains, which damped out after approximately at a nominal strain of 1%. The aggregate had a maximum stress of 1 at a nominal strain of 8.5%. At a nominal strain of 7.5%, multiple cracks nucleated and propagated, and this resulted in an unstable failure at a nominal strain of 9%. Therefore, the competing effects of plasticity, thermal decomposition, crack nucleation, dislocations, and voids led to unstable failure, as indicated by the stress unloading (Figure 6.5) where the local stresses and dislocation densities sharply increased as the crack impinged on the RDX-estane interface.

6.2.2 $10,000\text{ s}^{-1}$ Nominal Strain Rate

For a nominal strain rate of $10,000\text{ s}^{-1}$ at a nominal strain of 9.4% the normal stress (Figure 6.7a) had a maximum normalized value of 5.5 that occurred at the RDX crystal-estane interface. Crack nucleated from voids, and they subsequently propagated towards the estane interface. This is consistent with experimental observations that cracks can be impeded by viscoelastic or amorphous regions [29-31]. The buildup of normal stress at the interface is also similar with the $1,000\text{ s}^{-1}$ nominal strain rate case. The only difference is that the normal stresses were higher for the $10,000\text{ s}^{-1}$ case, which is due to dynamic strain rate hardening. The normal stress had a minimum normalized value of -1.5, which occurred in the vertical ligaments of the binder that were under hydrostatic compression (Figure 6.7d). The lateral stress (Figure 6.7b) had a maximum normalized value of 2.5, which occurred in the horizontal ligaments of the binder that were generally under hydrostatic tensile pressure as evidenced from Figure 6.7d. The lateral stress had a minimum normalized value of -5.5. The shear stress (Figure 6.7c) had a maximum normalized value of 1.2 and a minimum normalized value of -1.4, and these maximum values occurred at the peripheral regions of the RDX crystals where the adjacent estane binder had experience extensive shearing. The hydrostatic pressure (Figure 6.7d) had a maximum normalized value of 2.5, which occurred in the horizontal ligaments of the binder due to the large bulk modulus associated with the polymer binder. The hydrostatic pressure had a minimum normalized value -1.5 that occurred in the vertical ligaments of the binder that were under hydrostatic compression due to crystal sliding.

The temperature (Figure 6.8a) accumulated at the peripheries of the voids and crystals as well as in regions where crack-tip interaction with the interface had occurred with a maximum normalized value of 1.45 occurring at the crack-tip interaction region shown in (Figure 6.8c). The plastic shear slip (Figure 6.8b) accumulated a maximum value of 45%, which occurred at the crack-tip interaction region shown in (Figure 6.8c). Figure 6.8c shows a zoomed in view of the crack-tip interaction with the polymer binder and the resultant temperature rise. The dissipated energy (Figure 6.8d) had a maximum value of 4.5E8 joules of energy dissipated, which occurred at the crack-tip interaction region. Due to the localization of temperature, shear slip, and dissipated energy at the crack-tip interaction region, the system is dominated by crack nucleation at the void peripheries and the subsequent propagation to the binder where hotspot formation occurred as detailed by LaBarbera and Zikry [58].

The mobile dislocation densities for slip system one (Figure 6.9a), (010) [001], which was the most active slip system, had a maximum normalized value of 4200. The immobile dislocation densities for slip system one (Figure 6.9a), (010) [001], had a maximum normalized accumulation of 420. The maximum normalized values for the mobile and immobile dislocations densities occurred at the crack-tip interaction region as shown in Figure 6.8c.

Figure 6.10 shows the temporal evolution of the normal stress, lateral stress, shear stress, hydrostatic pressure, mobile dislocation density, and immobile dislocation density from the critical interface region as shown in Figure 6.8c. The normal stress, lateral stress, shear stress, and hydrostatic pressure all increased, in magnitude, up to a nominal strain of

8.5%. During this increase, there were wave reflections. At a nominal strain of 8.5%, the crack that has nucleated from the adjacent void (Figure 6.8c) has propagated into the critical fracture region and results in a sharp increase in the normal stress, lateral stress, shear stress, and hydrostatic pressure. During this sharp increase in normal stress, lateral stress, shear stress, and hydrostatic pressure, the mobile and immobile dislocation densities sharply increase. At a nominal strain of approximately 9.2%, local failure occurred and subsequent unloading of stresses began as indicated by the sharp drop in normal stress, lateral stress, shear stress, and hydrostatic pressure. Therefore, the crack propagated into the region and encountered the interface. Then subsequently, increased plasticity at the interface resulted in unstable local failure of the aggregate as indicated by the unloaded stresses (Figure 6.10).

The stress-strain curve for the overall aggregate response is shown in Figure 6.11. At a nominal strain of approximately 1.5%, initial high frequency dynamic wave reflections damped out. Up to 9% nominal strain, the stress increased with strain while also exhibiting dynamic wave reflections. At a nominal strain of 9%, local failure and dynamic localized plasticity began to occur which resulted in a subsequent lowering in the stress as the strain increased. The maximum global stress was approximately 1.1 at a nominal strain of 9% , which was higher than the maximum normalized stress of 1 for the $1,000\text{ s}^{-1}$ nominal strain rate case, and this is due to dynamic strain-rate hardening .

For both the $1,000\text{ s}^{-1}$ and $10,000\text{ s}^{-1}$ nominal strain rate cases, crack nucleation occurred primarily at the peripheries of the voids where the stresses on the cleavage planes exceeded the local fracture stress. Once crack nucleation occurred, the cracks propagated towards the binder where the cracks were arrested. This is due to the propagating crack

interacting with the interrelated effects of plasticity, temperature, dislocation densities, and shear slip. Crack bridging can also occur across the viscoelastic estane binder as noted by several experimental investigations [29-31].

6.3 Summary

The effects of local failure initiation through crack nucleation and propagation were investigated for nominal strain rates of $1,000\text{ s}^{-1}$ and $10,000\text{ s}^{-1}$. Cracks nucleated at void peripheries and propagated to the estane binder. Crack nucleation and propagation was affected by the heterogeneous nature of RDX energetic aggregate and the inherent interfaces within the material. The RDX-estane interfaces affected crack propagation and resulted in crack arrest at the binder. Thermal buildups were affected by crack nucleation and propagation and the RDX-estane interfaces. Large thermal buildups occurred at the interfaces where there was a competition between crack propagation through the interface and crack arrest at the interface.

For a nominal strain rate of $1,000\text{ s}^{-1}$, the normal stresses were a maximum at the crack-tip interface region. The shear stress was a maximum at the RDX crystal peripheries where extensive shearing had occurred in the adjacent viscoelastic estane binder. The lateral stress and hydrostatic tensile pressure were a maximum in the horizontal ligaments of the binder, and the hydrostatic compressive pressure was a maximum in vertical ligaments of the binder where crystal to crystal interaction and sliding had occurred. The temperature, shear slip, and dissipated energy were all maximums at the critical interface region where crack-tip interaction occurred. The mobile and immobile dislocation densities accumulated, at the peripheries of the voids and crystals, and at the crack-tip interaction region. The temperature

buildup was dominated by the competition between crack propagation through the RDX-estane interface and crack arrest at the interface. This resulted in an incompatibility, for crack propagation through the interface, which affected crack growth. For a nominal strain rate of $10,000\text{ s}^{-1}$, the results were similar when compared with a strain rate of $1,000\text{ s}^{-1}$. However, more pronounced dynamic wave reflections were shown in the stress-strain curve for a nominal strain rate of $10,000\text{ s}^{-1}$ in comparison to a nominal strain rate of $1,000\text{ s}^{-1}$.

Results from this study indicate that the interrelated effects of dynamic strain rate loading, polymer binder response, void porosity, and crack nucleation/propagation significantly affect local failure mechanisms. Voids facilitated the nucleation of cracks, which then resulted in local failure of the aggregate as the cracks propagate toward the binder. The polymer binder affected interfacial incompatibilities with RDX crystal fracture and resulted in local failure of the aggregate due to a buildup of inelastic deformation at the interface and subsequent failure.

6.4 Tables and Figures

Table 6.1: RDX and Estane binder Material Properties

	RDX	Estane Binder
Density ($\frac{kg}{m^3}$)	1820	1190
Yield Stress (MPa)	580	--
Elastic Modulus (GPa)	18.4	--
Poisson Ratio	0.22	.499
Thermal Conductivity ($\frac{W}{m K}$)	0.29	0.14
Specific Heat (c_p) ($\frac{J}{kg K}$)	1260	1500
Rate Sensitivity Parameter	.01	--
Fracture Stress (GPa)	1.8	1.8
Initial Mobile Dislocation Density (m^{-2})	1e10	--
Initial Immobile Dislocation Density (m^{-2})	1e12	--

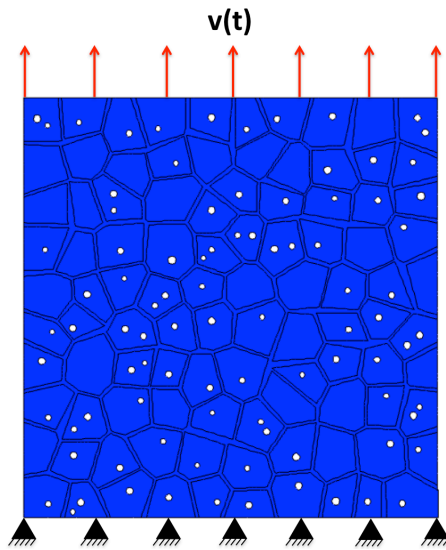


Figure 6.1: The RDX-estane aggregate with loading and boundary conditions, void distribution, and grain morphology.

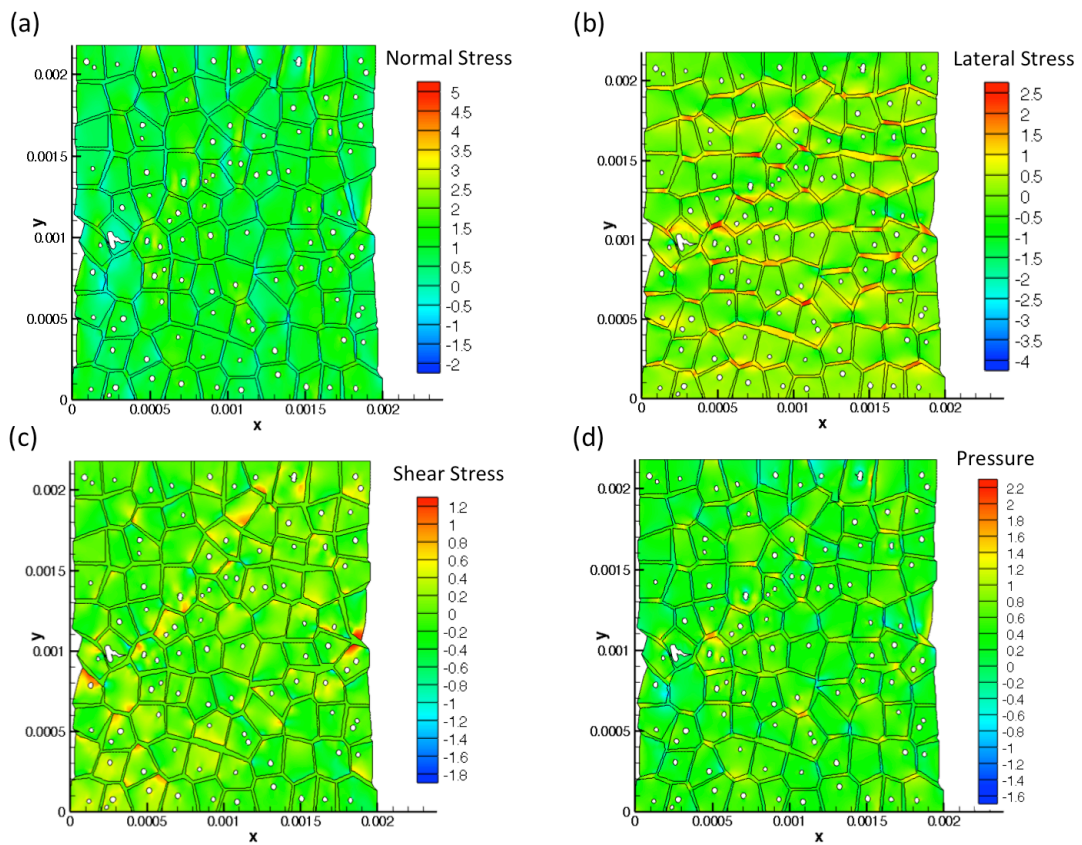


Figure 6.2: (a) Normal Stress, (b) lateral stress, (c) shear stress, and (d) pressure for a nominal strain rate loading of $1,000 \text{ s}^{-1}$ and at a nominal strain of 9.0%. (Spatial dimensions are in units of meters)

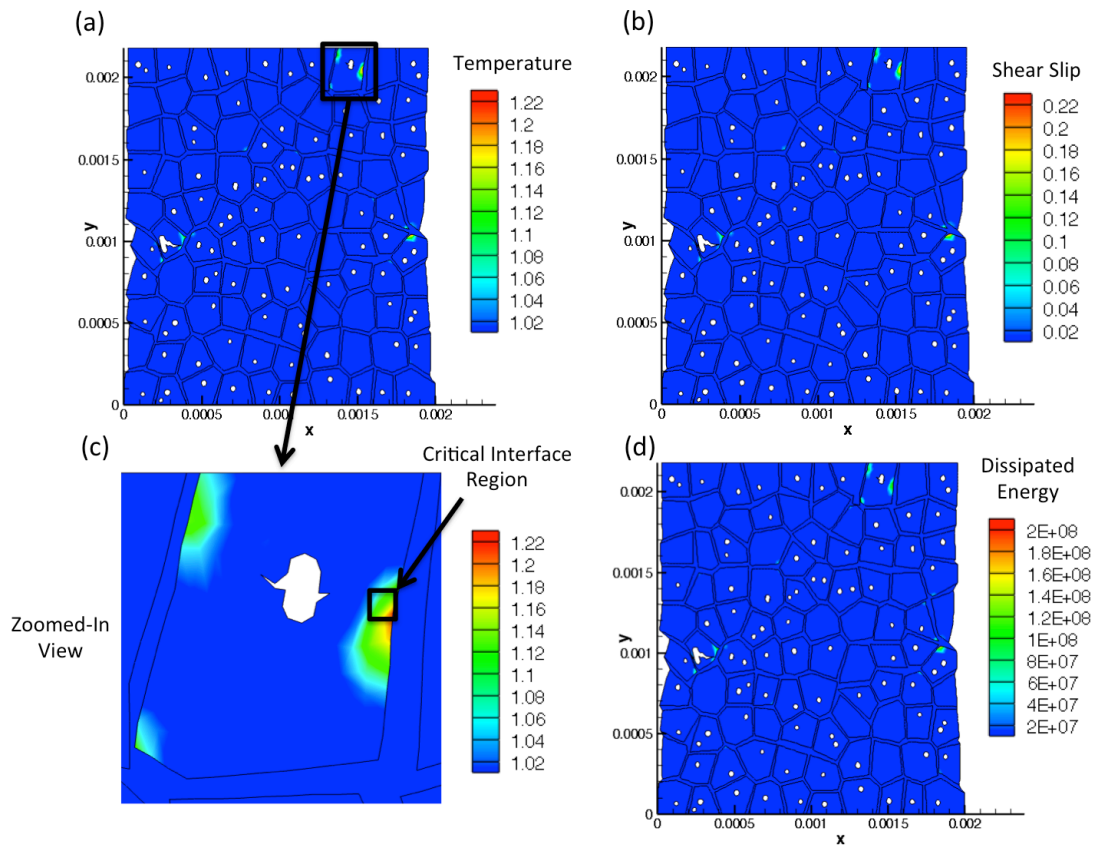


Figure 6.3: (a) Temperature, (b) shear slip, (c) zoomed in view of (a), and (d) dissipated energy for a nominal strain rate loading of $1,000 \text{ s}^{-1}$ and at a nominal strain of 9.0%. (Spatial dimensions are in units of meters)

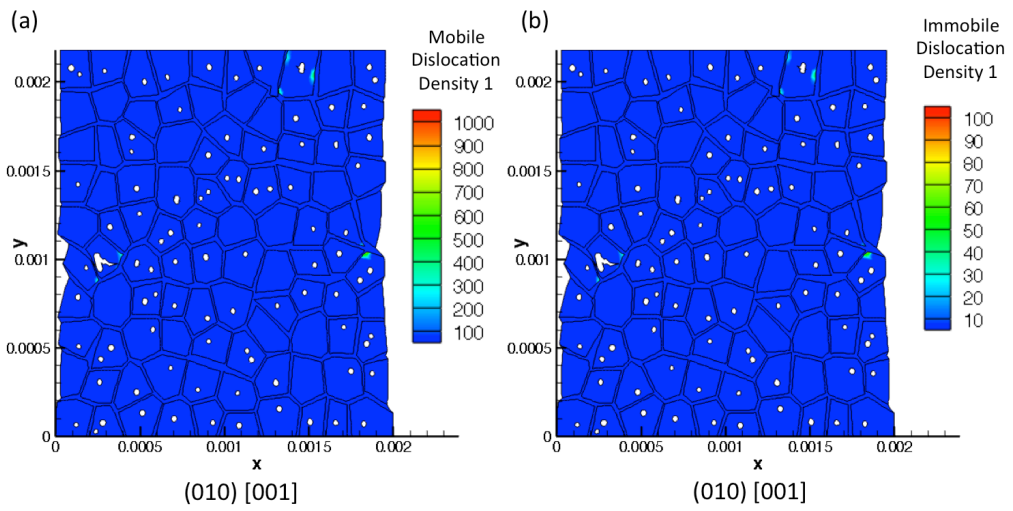


Figure 6.4: (a) Mobile and (b) immobile dislocation densities for the most active slip system for a nominal strain rate loading of $1,000 \text{ s}^{-1}$ and at a nominal strain of 9.0%. (Spatial dimensions are in units of meters)

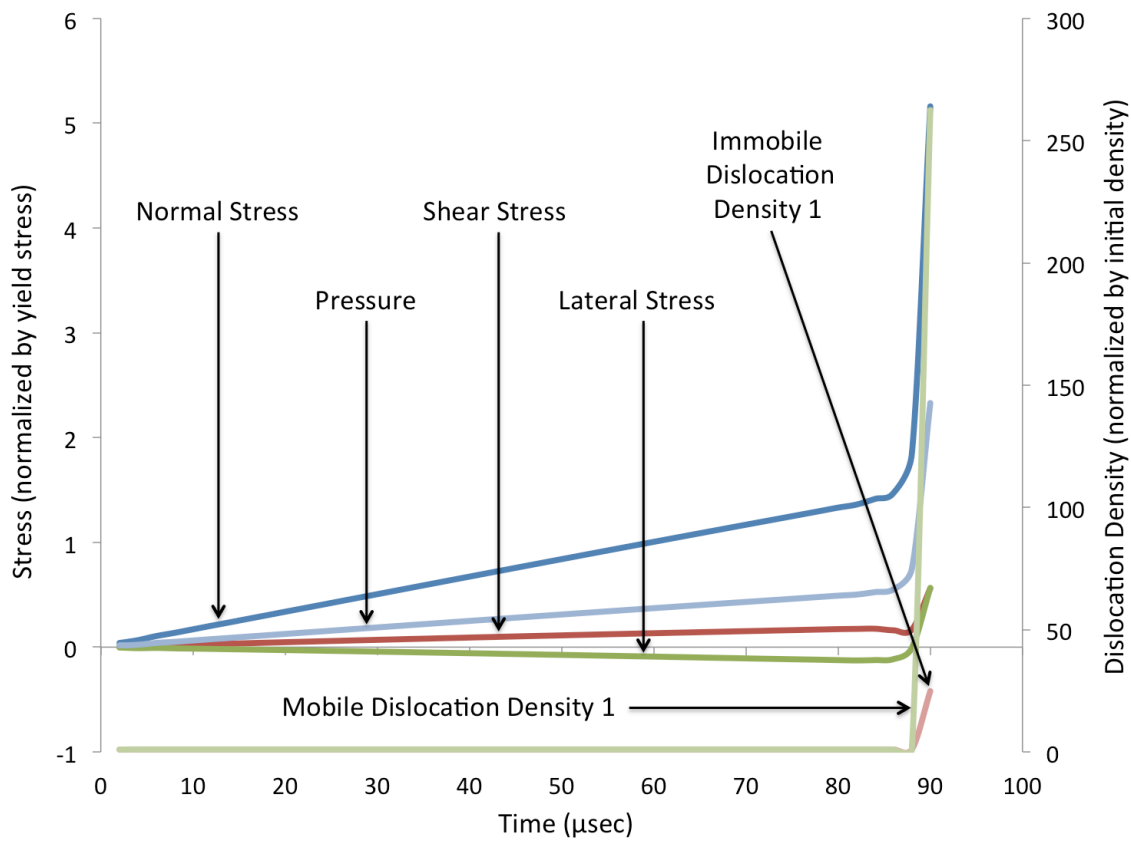


Figure 6.5: Normal stress, pressure, shear stress, lateral stress, mobile and immobile dislocation density, for slip system one, time history for the interface-crack interaction region for a nominal strain rate loading of $1,000 \text{ s}^{-1}$.

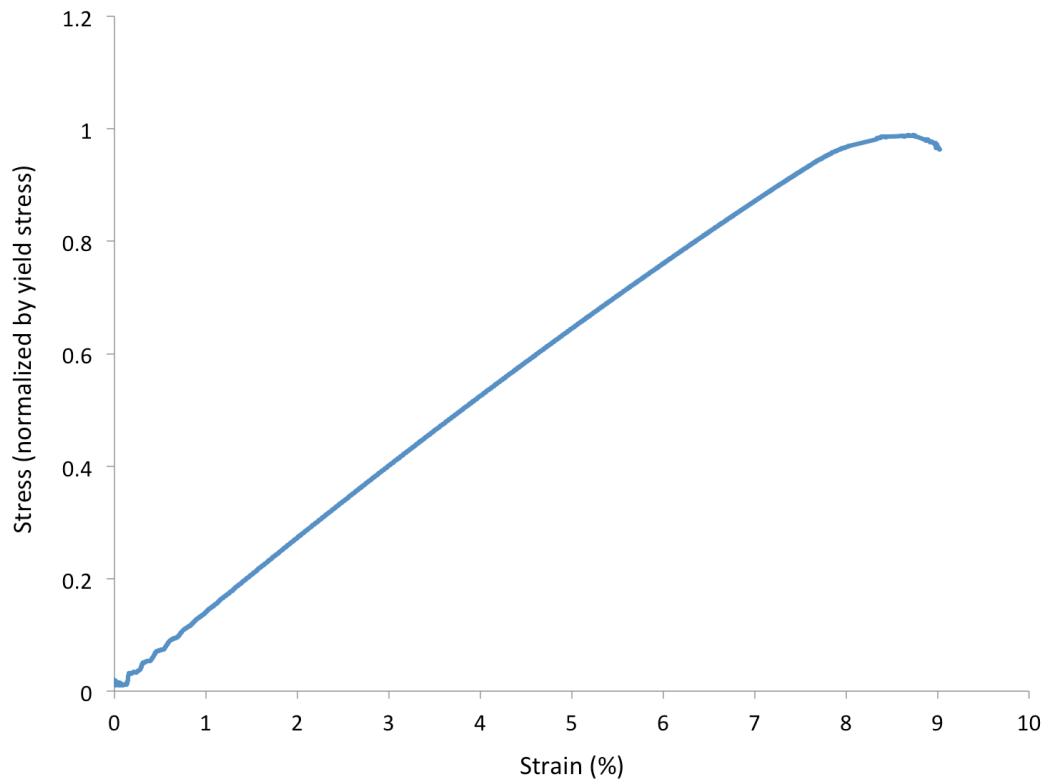


Figure 6.6: Stress-Strain curve for a nominal strain rate loading of $1,000 \text{ s}^{-1}$.

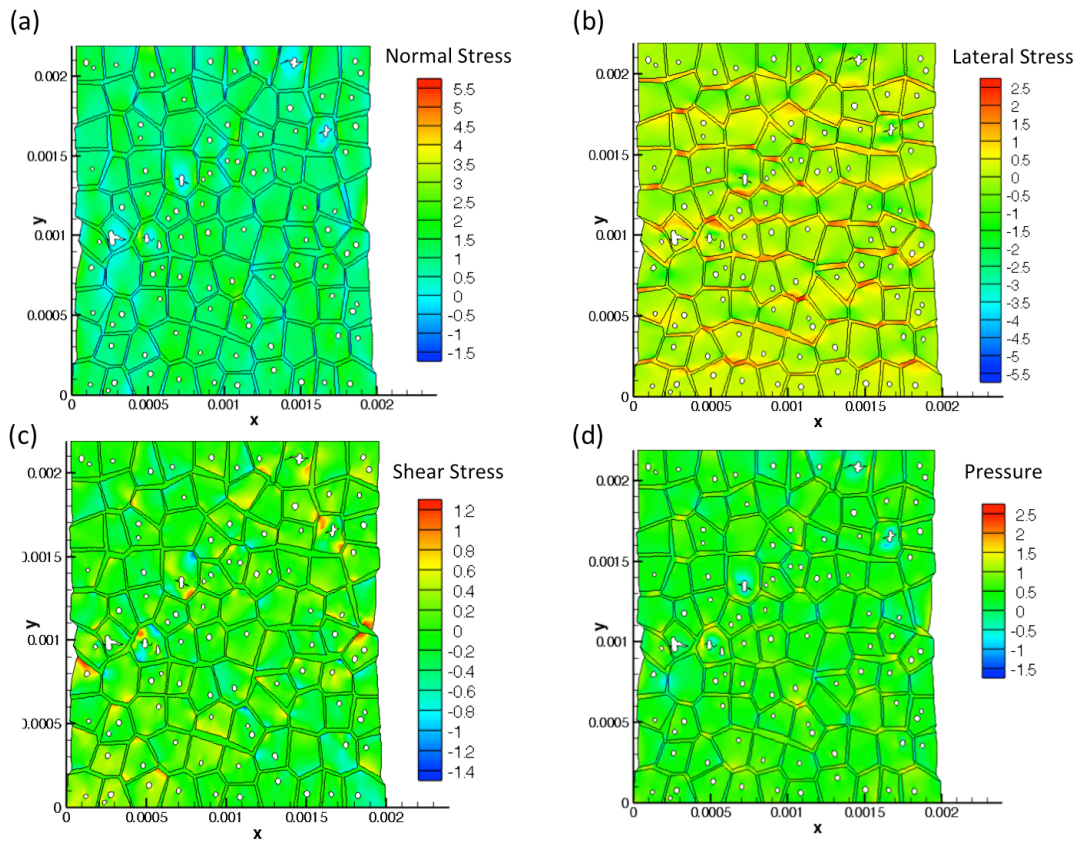


Figure 6.7: (a) Normal Stress, (b) lateral stress, (c) shear stress, and (d) pressure for a nominal strain rate loading of $10,000 \text{ s}^{-1}$ and at a nominal strain of 9.4%. (Spatial dimensions are in units of meters)

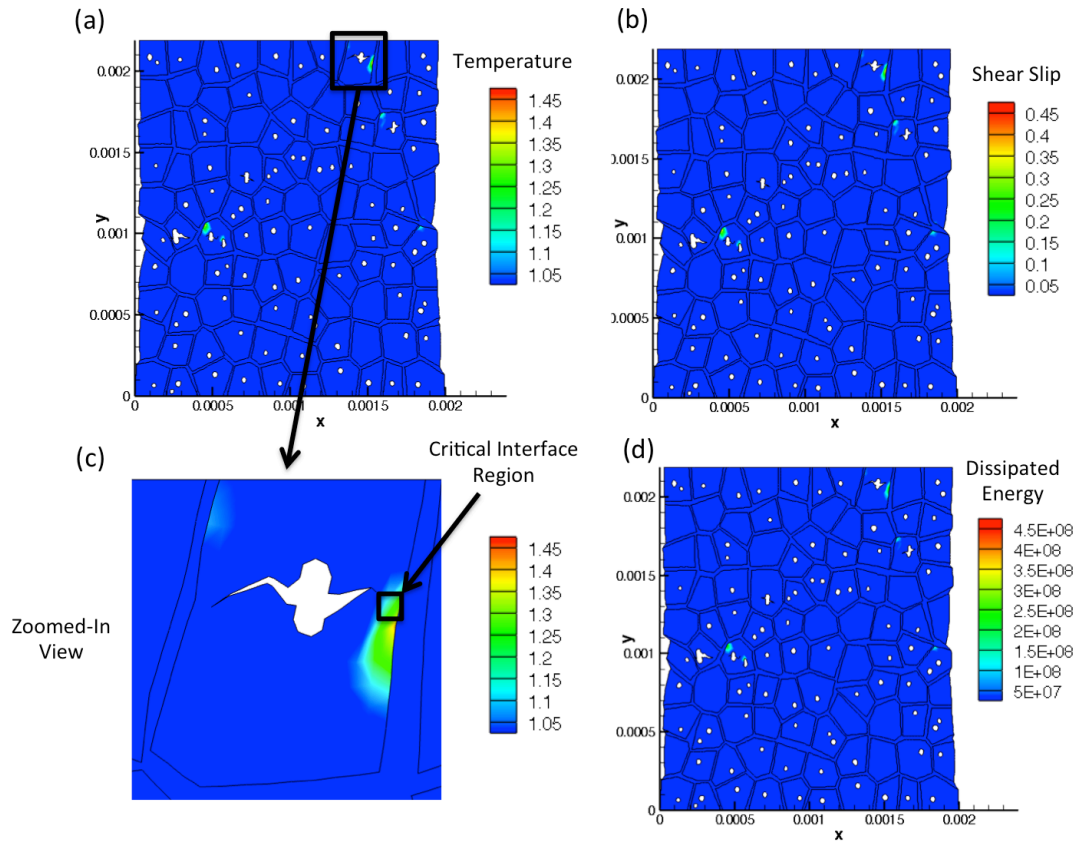


Figure 6.8: (a) Temperature, (b) shear slip, (c) zoomed in view of (a), and (d) dissipated energy for a nominal strain rate loading of $10,000 \text{ s}^{-1}$ and at a nominal strain of 9.4%.
(Spatial dimensions are in units of meters)

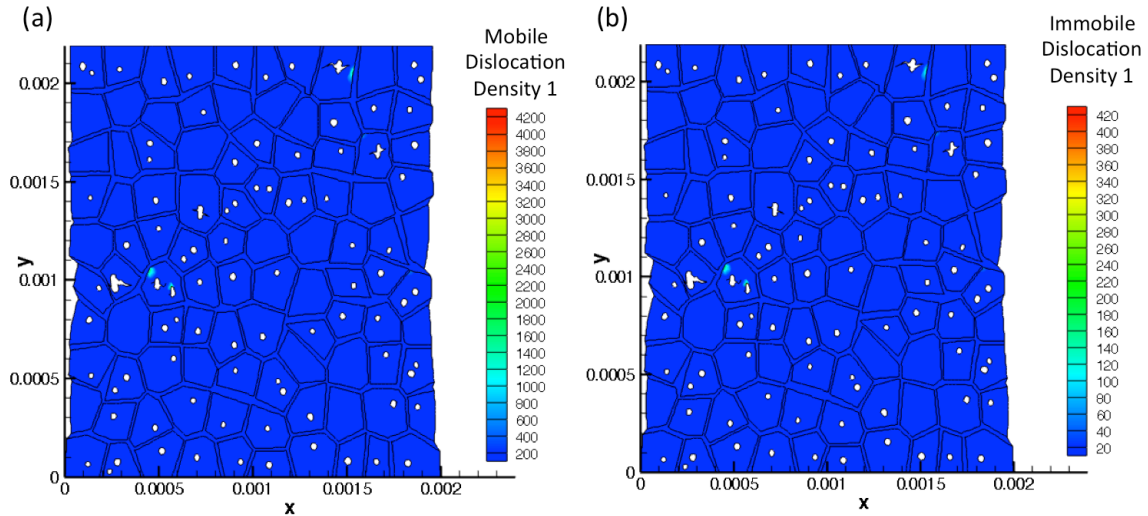


Figure 6.9: (a) Mobile and (b) immobile dislocation densities for the most active slip system for a nominal strain rate loading of $10,000 \text{ s}^{-1}$ and at a nominal strain of 9.4%. (Spatial dimensions are in units of meters)

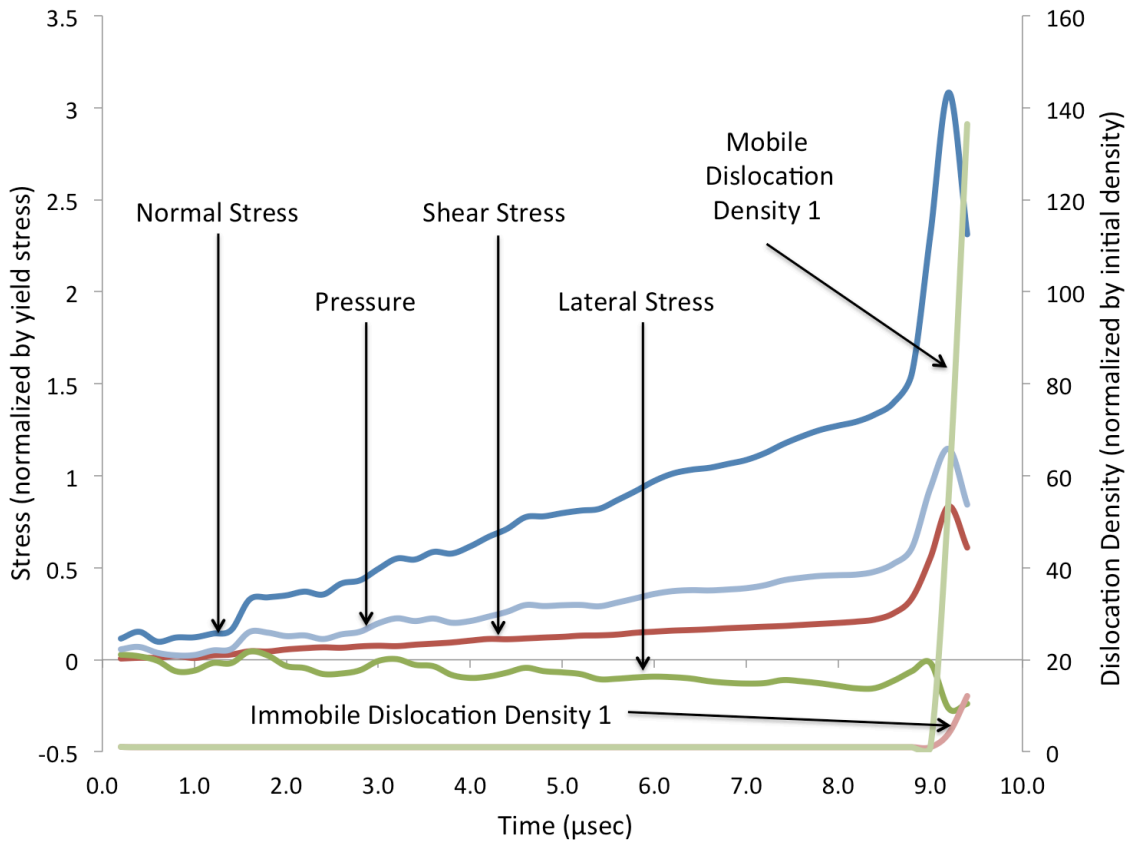


Figure 6.10: Normal stress, pressure, shear stress, lateral stress, mobile and immobile dislocation density time history for the interface-crack interaction region for a nominal strain rate loading of $10,000 \text{ s}^{-1}$.

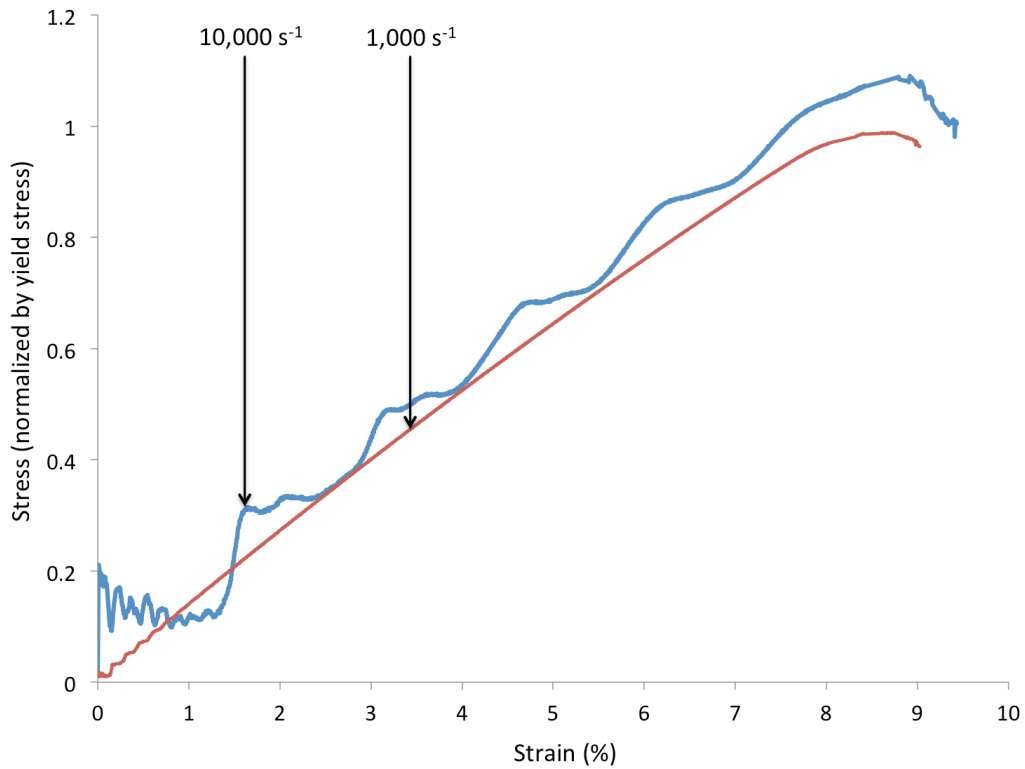


Figure 6.11: Stress-Strain curve for a nominal strain rate loading of $10,000 \text{ s}^{-1}$.

CHAPTER 7: The Effects of Grain Boundary Misorientations on Fracture Propagation and Crack Stability at Crystalline-Amorphous Energetic Interfaces

7.1 Introduction

Local failure in the heterogeneous crystalline-amorphous structure of energetic materials, the defects that span several spatial scales, and the dynamic thermo-mechanical loading conditions emphasize that a fundamental understanding of how local failure occurs, at the interfaces in energetic materials, occurs is needed. Therefore, the objective of this investigation is to formulate a predictive framework that accounts for the interrelated microstructural effects of crystalline plasticity, polymer binder relaxation, crystalline-amorphous fracture, inherent microstructural defects and features, and dynamic loading conditions on dynamic crack nucleation and growth near the interfaces in energetic materials. A recently developed dislocation-density based crystalline plasticity [35] approach, which has been coupled to a finite viscoelasticity formulation, dynamic fracture formulation, and dynamic finite-element techniques will be used to understand local failure at RDX-estane interfaces.

7.2 Results

Computational analyses were undertaken to investigate and predict the effects of low and high angle GB misorientations on crack propagation behavior at an interface for a RDX energetic bi-crystal with a viscoelastic polymer binder between the crystals. The finite element aggregate consisted of 2 grains of RDX crystals with an estane binder dispersed

between the crystals for an overall interface model of 1mm x 1mm (Figure 7.1) with a pre-crack length of 50 μm on the left edge of the model.

Based on Gallagher et al. [44], the RDX grains were assumed to have the following three independent slip systems – (010) [001], (021) [100], (02-1) [100] – with material properties given by Armstrong and Elban [1], Annapragada et al. [50], and Clayton and Becker [60] in Table 7.1. Clayton and Becker [60] give a range of yield stress for RDX, from approximately 160 to 640 MPa. Therefore, it was assumed that the yield stress is 300 MPa for this study. A polymer binder of estane was distributed between the RDX grains, for a spatially uniform interface. Material properties for the estane polymer binder were obtained from measurements by Mas et al. [39] and Barua and Zhou [23], as shown in Table 7.1.

The domain of influence radius for fracture nucleation was set to 50 μm , which is the width of the estane binder. The fracture stress was set to five times the yield stress of RDX for both RDX and the estane binder. Fixed boundary conditions were applied to the model bottom for two-dimensional plane-strain loading conditions. A tensile velocity was applied on the top surface, as shown in Figure 7.1, for dynamic nominal strain rate of 10,000 s^{-1} , with random low angle GB misorientations of less than 20° and random high angle GB misorientations between 20° and 70°.

7.2.1 Bi-Crystal, Random Low Angle GB Misorientations for a Nominal Strain Rate of 10,000 s^{-1}

For a nominal strain rate of 10,000 s^{-1} , at a nominal strain of 6.5%, with random low angle GB misorientations and a pre-existing crack of length 50 μm , the normal stress (Figure 7.2a) was a maximum at the interface opposite of where the pre-crack had propagated to the

estane binder and subsequently terminated. The maximum normalized normal stress was 4 and the minimum normalized normal stress was 0 in the regions that had unloaded due to crack propagation (stresses were normalized by the static yield stress). Another crack nucleated at the right, bottom free boundary of the model due to high stresses, which are most likely due to the local boundary conditions. The lateral stress (Figure 7.2b) had a maximum normalized value of 2, which occurred where the secondary crack was interacting with the estane binder, and a minimum normalized value of -0.5, which occurred in the binder where extensive polymer shearing occurred due to unloading associated with crack propagation. The shear stress (Figure 7.2c) had a maximum normalized value of 1, which occurred in the region of crack interaction with the polymer binder for the secondary crack, with a minimum normalized value of -0.2 occurring in the region dominated by shearing due to unloading associated with crack propagation. The pressure (Figure 7.2d) was a maximum in where the secondary crack interacted with the estane binder.

To further understand the mechanics of crack arrest at the interface, Figure 7.3 shows the spatial distribution of normal stress, shear stress, and lateral stress for the thick, dark line shown in Figure 7.2d. The normal stress, lateral stress, and shear stress on the left side of the RDX-estane interface (inside of the left RDX crystal) was low, with a maximum normalized value of 0.65 occurring for normal stress. As the spatial location moves into the binder, the normal stress, lateral stress, and shear stress begin to rise. At the right RDX-estane interface (at the inner edge of the right RDX crystal), the normal stress increases sharply, to a maximum normalized value of 4.25, and then decreases as the spatial location moves away from the interface. The lateral stress decreases as the spatial location moves away from the

right RDX-estane interface. Whereas, the shear stress increases slightly to a maximum normalized value of approximately 0.6, and then begins to decrease. Therefore, stresses in the binder region of the interface are lower than the fracture stress due to the viscous nature of the polymer binder. This further substantiates that crack propagation was arrested due to low stresses in the polymer binder, which is consistent with experimental results [29-31].

The temperature (Figure 7.4a), which includes the effects of thermal decomposition, plastic work heating, viscous dissipation, and thermal conduction, had a maximum normalized value of 1.08 (temperatures were normalized by the reference temperature, 293K), which occurred in the shear band in the right RDX crystal. The shear slip (Figure 7.4b), which is the plastic slip summed over all slip systems, had a maximum value of 16%, while small amounts of shear strain localization occurred directly on the opposing side of the interface from the crack that was impinging on the estane binder. The dissipated energy (Figure 7.4c), which includes the energy dissipated by plasticity and viscous dissipation, had a maximum of 2E8 joules. There was considerable build up of viscously dissipated energy in the binder directly ahead of the crack tip as a result of the impinging crack-tip.

The mobile dislocation density for slip system one (Figure 7.5a), (010) [001], which was the most active mobile slip system, had a maximum normalized value of 450 (mobile dislocation densities were normalized by the initial mobile dislocation density). The immobile dislocation density for slip system one (Figure 7.5b), (010) [001], which was the most active immobile slip system, had a maximum normalized value of 45. The deformation, for random low angle GB misorientations, was dominated by slip system one, (010) [001].

The crack tip normalized velocity (velocity was normalized by the dilatational wave speed of 3,379 m/s) for the crack that propagated from the pre-existing crack in the left side of the model is shown in Figure 7.6 as a function of time. The crack tip normalized velocity increases slowly until a time of approximately 3.1 μ sec, where the normalized velocity increased sharply to a peak of approximately 0.13 at a time of 4.75 μ sec. Peak crack tip velocity was attained as the crack approached the RDX-estane interface, where the velocity sharply decreased to zero at the interface at a time of approximately 5.05 μ sec. This further substantiates that crack arrest occurred as the crack tip approached the estane binder.

The nominal stress-strain curve (Figure 7.7) increases proportionally with strain up to a nominal strain of 4% and a nominal normalized stress of 2.25 (stress was normalized by the static yield stress). At 4% nominal strain, the stress sharply unloaded briefly due to crack propagation. At 5% nominal strain, the stress increased with strain until further crack propagation occurred and the stress unloaded. The after cracks propagated through both sides of the bi-crystal model, at a nominal strain of 7%, the nominal stress oscillated between 0 and 1. Unloading in the stress-strain curve was affected by dynamic crack propagation and nucleation as well as dynamic plasticity.

7.2.2 Bi-Crystal, Random High Angle GB Misorientations for a Nominal Strain Rate of 10,000 s⁻¹

For a nominal strain rate of 10,000 s⁻¹, at a nominal strain of 7.5% and random high angle GB misorientations, the normalized normal stress (Figure 7.8a) was a maximum of 4 and the minimum was 0, which occurred in the unloaded regions of the model, due to crack nucleation and propagation. Two cracks were present in the model; one propagated from the

pre-existing crack and the second nucleated at the bottom, right edge of the model. The crack that propagated from the pre-existing crack had two sharp regions, which are associated with a change in the cleavage plane that had maximum stress. One sharp change in crack path occurred approximately 150 μm from the estane binder, while the second occurred at the crack tip intersection with the estane binder. This is a result of the high random misorientations that affect the orientations of the cleavage normals, and further substantiates the importance of misorientations in aggregates, as compared with low misorientations, where smooth crack propagation occurred. The lateral stress (Figure 7.8b) had a maximum normalized value of 3 and a minimum value of -1, which occurred in the estane binder, between the two cracks. The shear stress (Figure 7.8c) had a maximum normalized value of 1.5 and a minimum value of -0.5 that occurred just above the crack tip region. The pressure (Figure 7.8d) had a maximum normalized value of 3 and a minimum value of -0.5.

Maximum temperature accumulation (Figure 7.9a) occurred at the two sites where the cleavage planes changed with a maximum normalized value of 1.3. The shear slip (Figure 7.9b) was a maximum in the first sharp change in crack path, with a maximum value of 90%. The maximum dissipated energy (Figure 7.9c) was 4E08 joules and occurred in the same region as the maximum temperature accumulation.

The immobile dislocation density buildup for slip system one (Figure 7.10a) had a maximum normalized value of 40, while slip system two (Figure 7.10b) had a maximum normalized accumulation of 600. Slip system three (Figure 7.10c) had a maximum normalized buildup of 50. The maximum buildup of dislocation densities and buildup for the low angle misorientations was an order of magnitude lower than the high angle

misorientations. This demonstrates that high angle misorientations facilitate more inelastic deformation for RDX crystals than low angle misorientations. This is consistent with experimental observations that deformation is highly anisotropic and orientation dependent for RDX crystals [57, 61] due to the low number of unique slip systems available for inelastic deformation.

To understand the sharp pointed crack path in the left RDX crystal, Figure 7.11 shows the temporal evolution of normal stress, lateral stress, pressure, and temperature for the critical element region shown in Figure 7.10c with the thick, dark circle. Normal stress, pressure, and lateral stress all increase up to a time of 4.5 μ sec, at which time, they sharply increased to a normalized value of 10, 6, and 4.75, respectively, which was a direct consequence of the resulting crack propagating near the critical element region and the subsequent changing the cleavage plane of crack propagation direction due to lattice rotations as a result of plastic deformation. The temperature remained at the initial temperature until approximately 4.5 μ sec, where the temperature sharply increased to a normalized value of 1.31 at a time of 7 μ sec. The temperature then gradually decreased to the effects of thermal conduction for the remaining time. Therefore, lattice rotation, due to deformation of high angle GB misorientations, raises the probability of switching cleavage plane propagation directions, which can result in large temperature buildups due to the temporary pinning of the crack tip.

The crack tip velocity for the crack in the left RDX crystal is shown in Figure 7.12. The crack tip velocity slowly increases until a time of 3 μ sec, at which time, the crack tip normalized velocity peaked at approximately 0.08 at a time of 5 μ sec. This peak in crack

velocity corresponds to the sharp increase in normal stress, lateral stress, pressure, and temperature shown in Figure 7.11 which is associated with the subsequent arresting of the crack which is evident due to the sudden drop in crack tip velocity after the first peak is attained. The crack tip velocity remains low until a time of approximately 6.75 μ sec, at which time the crack tip velocity becomes unbounded which is associated with unstable crack growth. The crack tip propagated to the interface where it was arrested due to low stresses in the binder regions. Therefore, the crack propagated to the critical element region shown in Figure 7.10c, and was arrested for approximately 2 μ sec due to a change in cleavage plane propagation direction. At which point the stress on the new cleavage plane built up. At a time of 6.75 μ sec, the stresses on the new cleavage plane violated the failure criterion and subsequently propagated unstably to the RDX-estane interface where it was arrested. This is in comparison to the low angle GB misorientations case, where the crack velocity continuously built up until the crack tip reached the RDX-estane interface, where it was arrested.

The nominal stress-strain behavior for low and high angle misorientations is shown in Figure 7.13. For high angle misorientations, the stress increased up to a nominal strain of 4%, and a nominal stress of 2.4. At 4% nominal strain, the pre-existing crack propagated, which is marked by sharp drop in stress at 5% nominal strain. The stress began to increase up to a strain of 7%, which indicates the crack has been arrested. Then, the crack continued to propagate, which is marked by a sharp drop in stress at a nominal strain of 7.5%. The stress-strain behavior (Figure 7.13) demonstrates that high angle misorientations lead to a larger build up of stress due to crack arrest as well as large regions of plasticity in comparison to the

low angle misorientation case. For low angle misorientations, the bi-crystal unloads due to fracture at an earlier strain in comparison to high angle misorientations. The peak stress for high angle misorientations is higher than that of low angle misorientations, which is due to the temporary arresting of the crack.

7.2.3 16 Crystal Aggregate, Random Low Angle GB Misorientations for a Nominal Strain Rate of 10,000 s⁻¹

The finite-element aggregate of 16 grains of RDX crystals with an average grain size of 250 μm for an overall aggregate size of 1mm x 1mm (Figure 7.14) consisted of approximately 7,000 quadrilateral elements. The RDX crystalline morphology was generated utilizing a Voronoi tessellation scheme. Based on Gallagher et al. [44], the RDX grains were assumed to have the following three independent slip systems – (010) [001], (021) [100], (02-1) [100] – with material properties given by Armstrong and Elban [1] and Annapragada et al. [50] in Table 7.1. A polymer binder of estane, with a volume fraction of approximately 15%, was randomly distributed between the RDX grains. The material properties for the estane polymer binder were based on measurements by Mas et al. [39] and Barua and Zhou [23], as shown in Table 7.1. A pre-existing crack of 100 μm was used in the left side of the model.

The pre-existing crack was placed to model a crack that has already nucleated. The immobile dislocation density for slip system one (Figure 7.15a), (010) [001], for a nominal strain rate of 10,000 s^{-1} , at a nominal strain of 10%, accumulated a maximum dislocation density of 180 (dislocation densities have been normalized by the initial densities). The dislocation density, which is a measure of inelastic activity on slip system one, had localized

at the crack tip and the crystal edges where shear deformation occurred in the polymer binder. Shear slip (Figure 7.15b) built up at the crack tip and the crystal facets associated with shear deformation in the polymer binder. The energy dissipated due to viscous dissipation and plasticity (Figure 7.15c) localized in the binder regions, where viscous shearing dominated the deformation, and at the crack tip and crystal facets.

The pre-crack in the aggregate, did not propagate, but localized plasticity did form at the tip of the crack tip. Shear deformation in the polymer allowed relaxation of the binder, which constrained the crack from propagating, due to limiting stresses to below the fracture stress. A combination of polymer shear relaxation and plasticity at the crack tip prevented the stresses on the cleavage planes from violating the failure criterion. Therefore, polymer binder relaxation and crack tip plasticity arrested the crack. These results, for an aggregate with crystal morphology, substantiate that, although, at the interfacial scale, cracks can propagate and blunt due to plasticity, but also cracks can be arrested due to the relaxation associated with the polymer binder.

7.3 Summary

The effects, of GB misorientations on crack propagation towards a polymer binder in a bi-crystalline model, have been studied at a nominal strain rate of $10,000\text{ s}^{-1}$. Pre-existing cracks propagated towards the binder and were arrested due to low stresses in the binder. The low binder stresses are a direct consequence of the polymer material, which illuminates why cracks propagate in crystalline regions and terminate at the binder.

For low angle GB misorientations, the pre-existing crack propagated in a straight line towards the estane binder. The crack tip velocity increased continuously until the crack

reached the estane binder, where it was arrested. The inelastic deformation was dominated by one slip system. For high angle misorientations, the pre-existing crack propagated towards the estane binder, but was arrested briefly while the crack propagation direction changed from one cleavage plane to another due to the high misorientations and further exacerbated by lattice rotations due to inelastic deformation. During this brief period of crack arrest, the inelastic deformation built up on three slip systems and the temperature increased at the crack tip. The stress on the new cleavage plane attained the failure stress and the crack unstably propagated towards the binder, where it was arrested. For an aggregate, the relaxation associated with the polymer binder can result in crack arrest due to the lowering of stresses on the cleavage planes by relaxing mechanical strains through viscous dissipation in the polymer.

Results from this study indicate that the interrelated effects of dynamic strain rate loading, polymer binder response, GB misorientation, and pre-existing cracks significantly affect crack propagation towards an interface. Pre-existing cracks propagate differently depending on the level of misorientation. Plasticity in RDX is dominated by different slip systems due to the highly anisotropic orientation dependent, inelastic deformation behavior. Cracks can be arrested due to plasticity and polymer binder relaxation.

7.4 Tables and Figures

Table 7.1: Material Properties for RDX and Estane

	RDX	Estane Binder
Density ($\frac{kg}{m^3}$)	1820	1190
Yield Stress (MPa)	300	--
Elastic Modulus (GPa)	18.4	--
Poisson Ratio	0.22	.499
Thermal Conductivity ($\frac{W}{m K}$)	0.29	0.14
Specific Heat (c_p) ($\frac{J}{kg K}$)	1260	1500
Rate Sensitivity Parameter	.01	--
Fracture Stress (GPa)	1.5	1.5
Initial Mobile Dislocation Density (m^{-2})	1e10	--
Initial Immobile Dislocation Density (m^{-2})	1e12	--

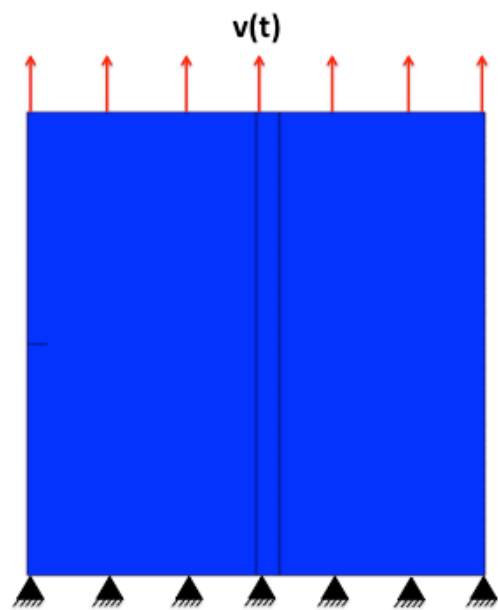


Figure 7.1: The RDX-estane bi-crystal with loading, boundary conditions, and grain morphology.

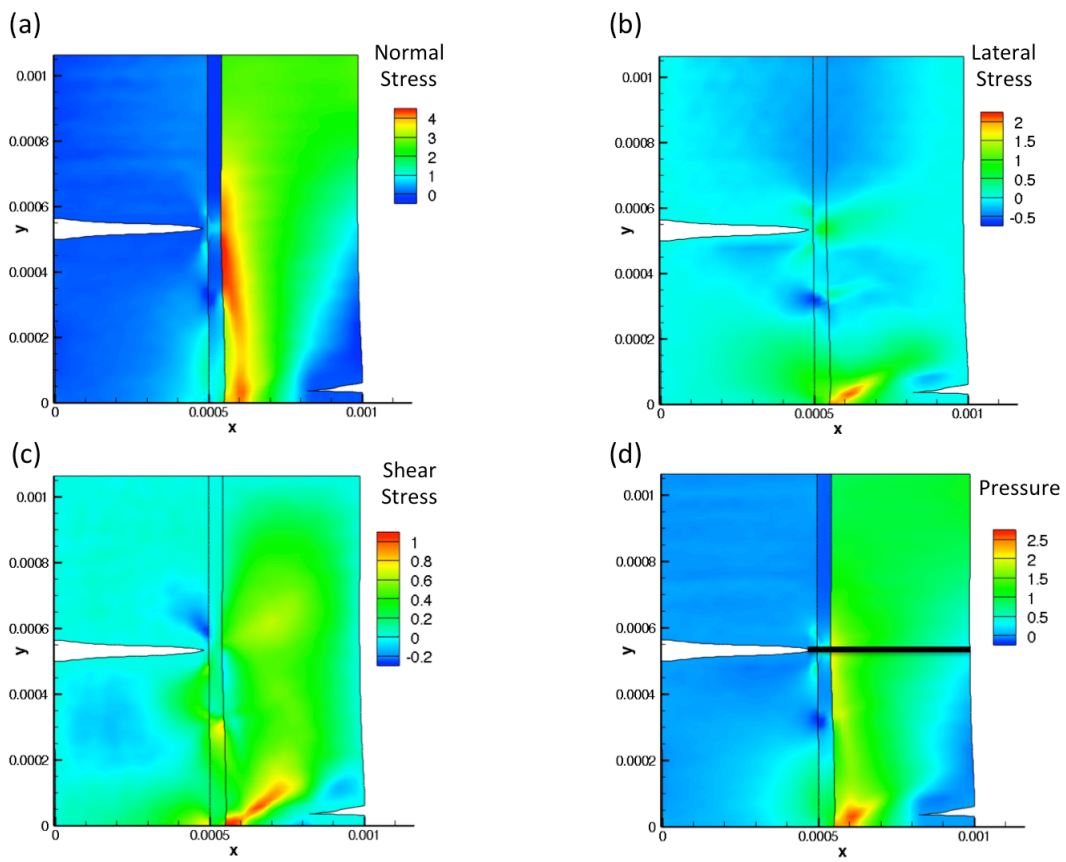


Figure 7.2: (a) Normal Stress, (b) lateral stress, (c) shear stress, and (d) pressure for a nominal strain rate loading of $10,000 \text{ s}^{-1}$, at a nominal strain of 6.5%, and random low angle GB misorientations. (Spatial dimensions are in units of meters)

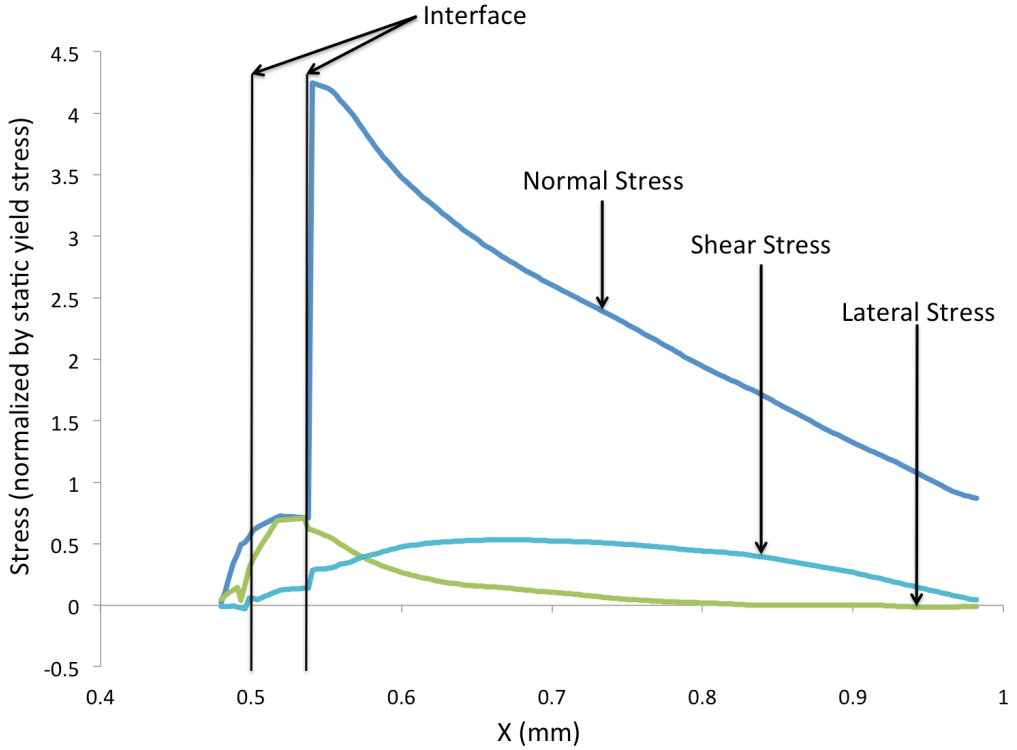


Figure 7.3: Normal stress, shear stress, and lateral stress spatial distribution across the RDX-estane interface for a nominal strain rate loading of $10,000 \text{ s}^{-1}$, at a nominal strain of 6.5%, and random low angle GB misorientations.

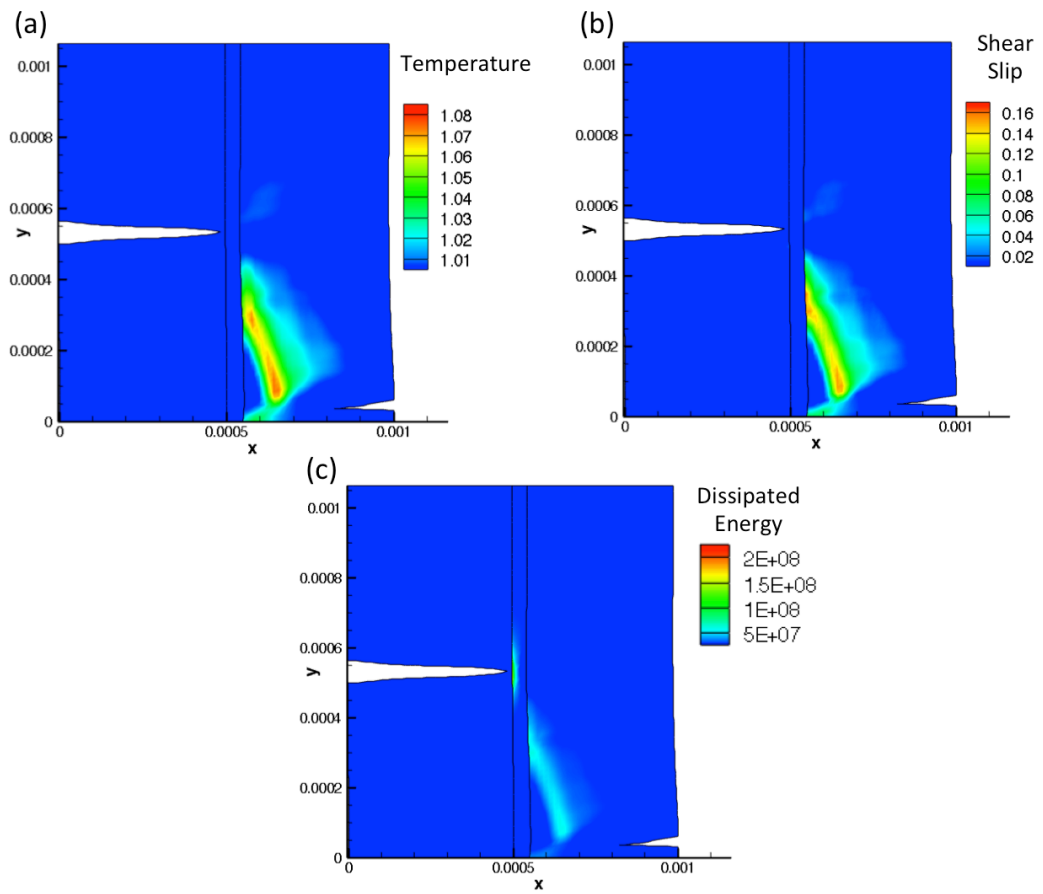


Figure 7.4: (a) Temperature, (b) shear slip, and (c) dissipated energy for a nominal strain rate loading of $10,000 \text{ s}^{-1}$, at a nominal strain of 6.5%, and random low angle GB misorientations.
 (Spatial dimensions are in units of meters)

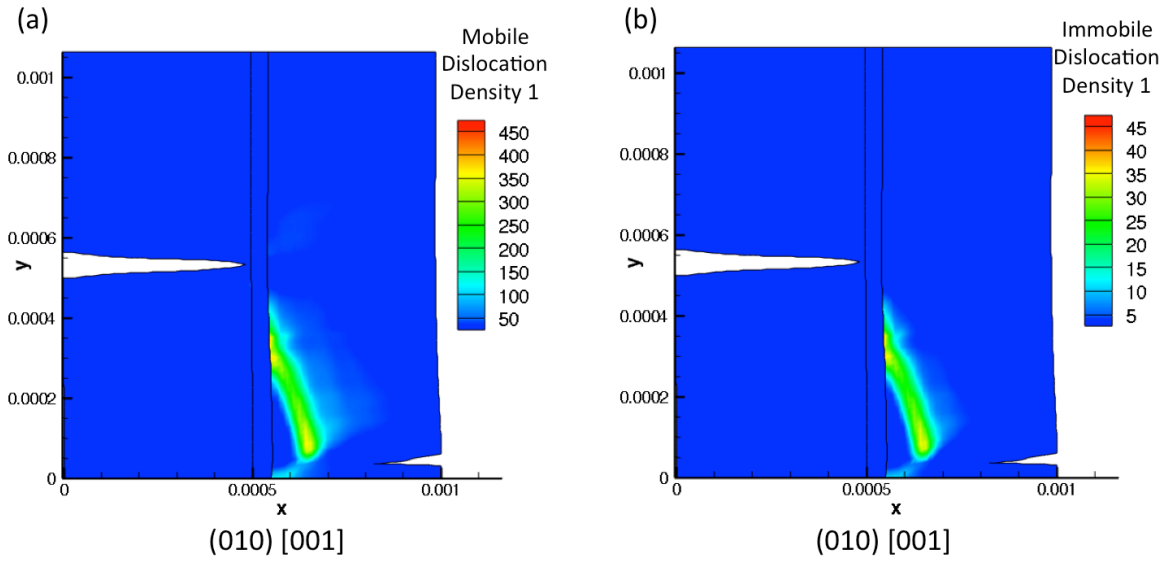


Figure 7.5: (a) Mobile dislocation density and (b) immobile dislocation density for slip system one, which was the most active slip system, for a nominal strain rate loading of $10,000 \text{ s}^{-1}$, at a nominal strain of 6.5%, and random low angle GB misorientations. (Spatial dimensions are in units of meters)

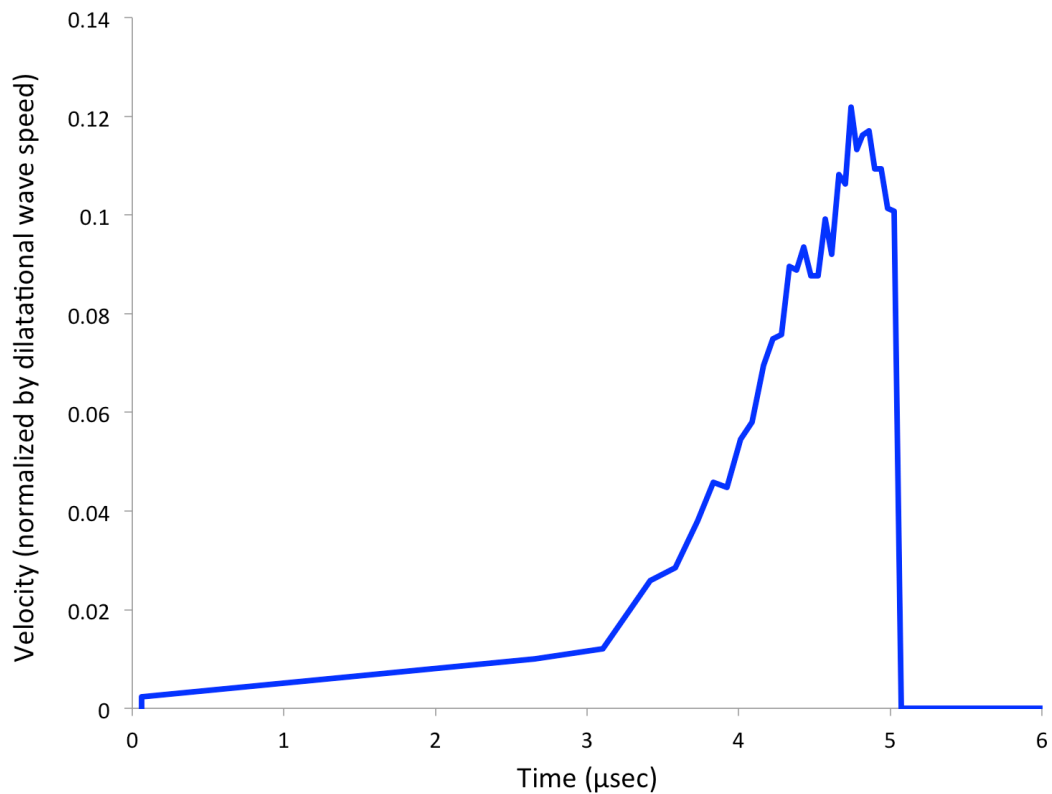


Figure 7.6: Crack tip velocity versus time for the crack propagating from the initial pre-crack, for a nominal strain rate loading of $10,000 \text{ s}^{-1}$ and random low angle GB misorientations.

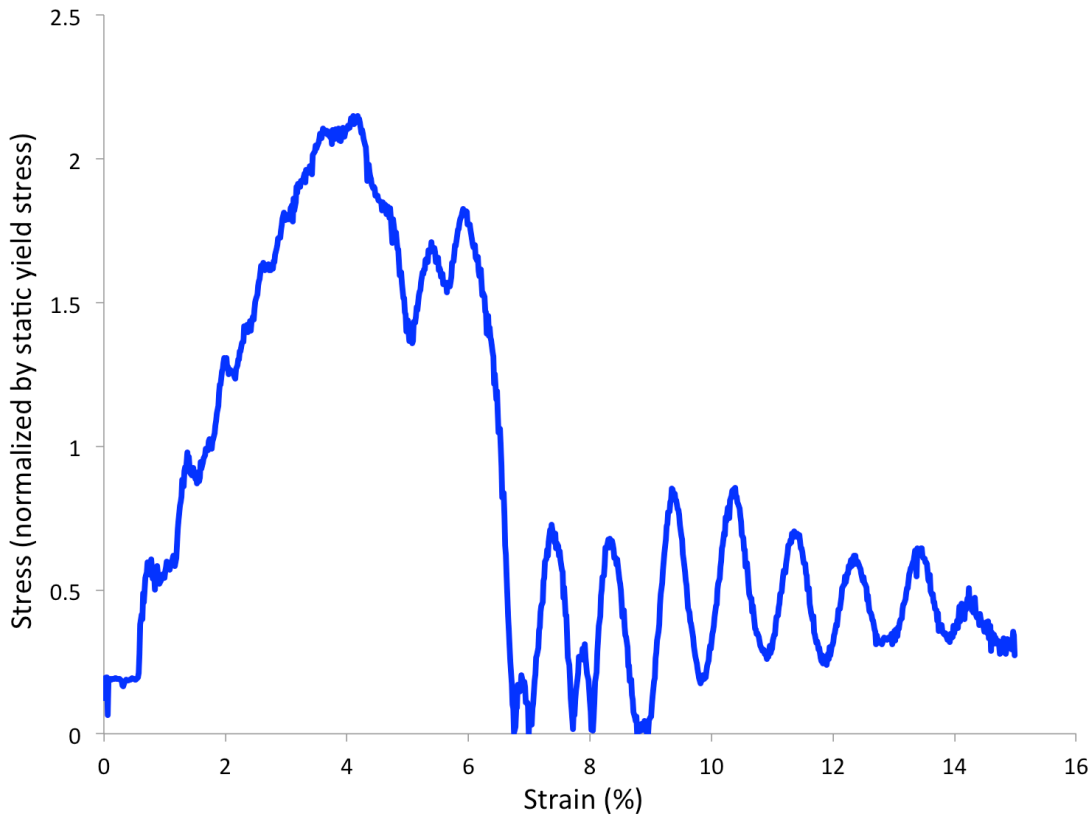


Figure 7.7: Nominal stress-strain curve for a nominal strain rate loading of $10,000 \text{ s}^{-1}$ and random low angle GB misorientations.

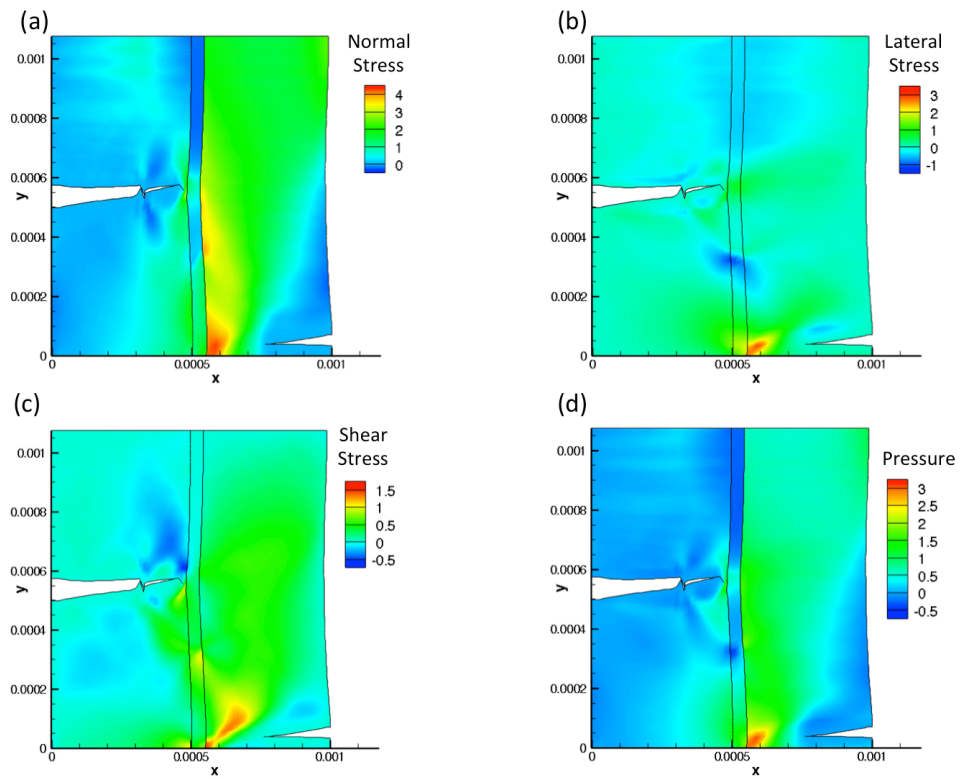


Figure 7.8: (a) Normal Stress, (b) lateral stress, (c) shear stress, and (d) pressure for a nominal strain rate loading of $10,000 \text{ s}^{-1}$, at a nominal strain of 7.5%, and random high angle GB misorientations. (Spatial dimensions are in units of meters)

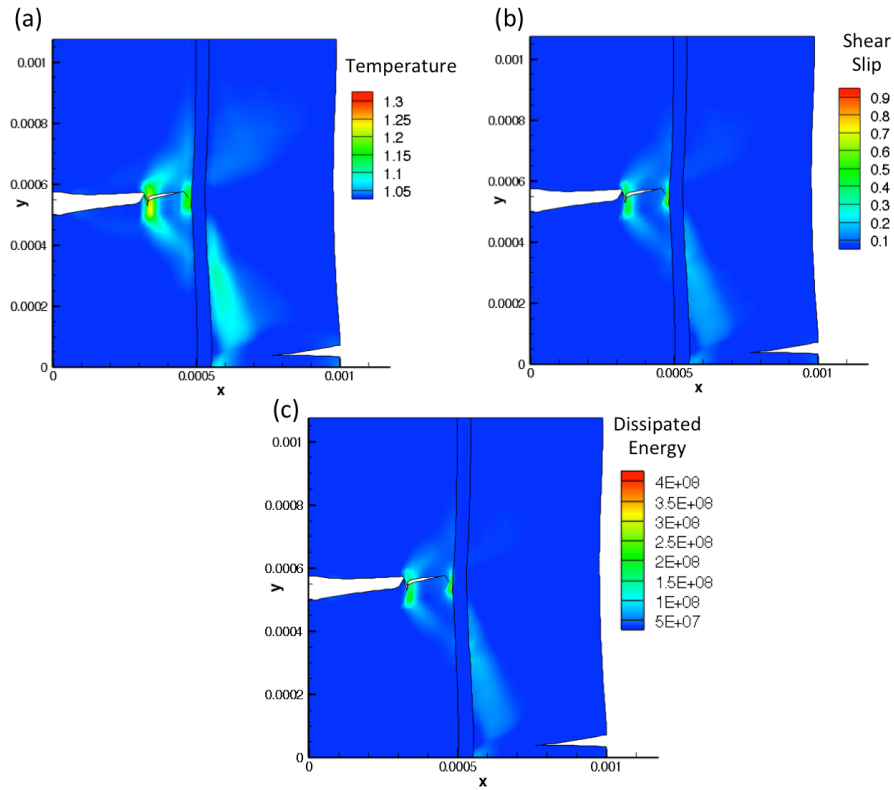


Figure 7.9: (a) Temperature, (b) shear slip, and (c) dissipated energy for a nominal strain rate loading of $10,000 \text{ s}^{-1}$, at a nominal strain of 7.5%, and random high angle GB misorientations. (Spatial dimensions are in units of meters)

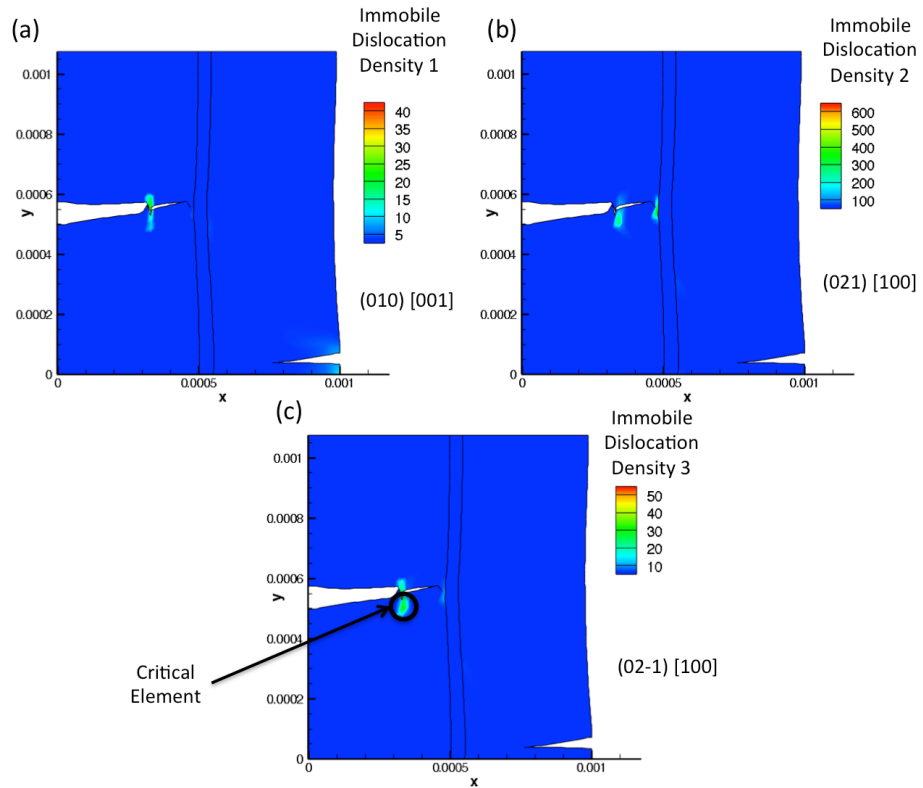


Figure 7.10: Immobile dislocation densities for (a) slip system one, (b) slip system two, and (c) slip system three for a nominal strain rate loading of $10,000 \text{ s}^{-1}$, at a nominal strain of 7.5%, and random high angle GB misorientations. (Spatial dimensions are in units of meters)

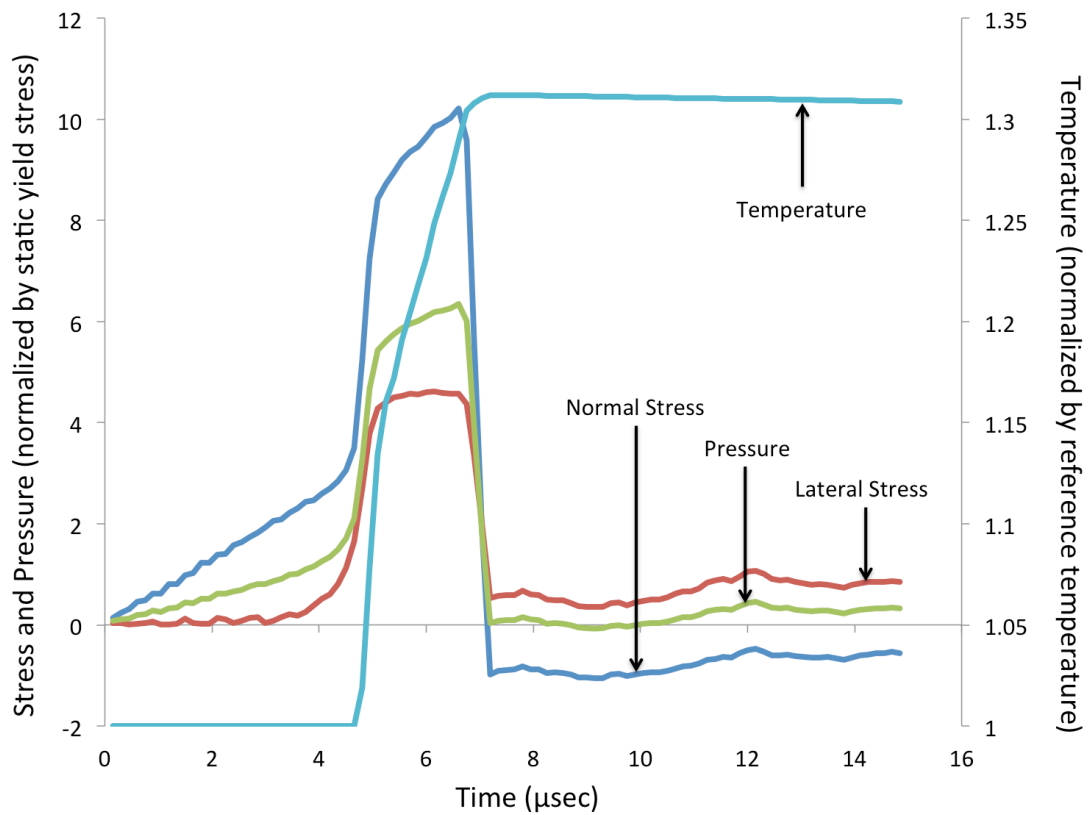


Figure 7.11: Time history plot of normal stress, pressure, lateral stress, and temperature for a nominal strain rate loading of $10,000 \text{ s}^{-1}$ and random high angle GB misorientations in the critical element location.

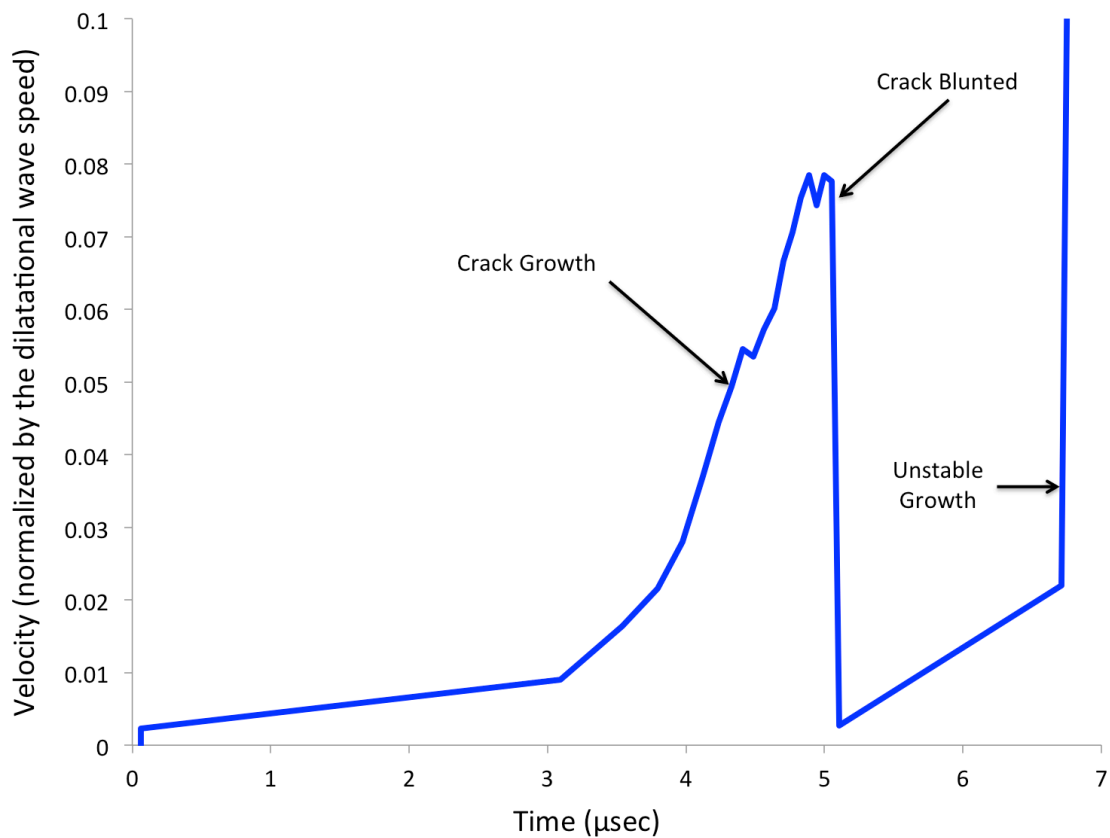


Figure 7.12: Crack tip velocity versus time for the crack propagating from the initial pre-crack, for a nominal strain rate loading of $10,000 \text{ s}^{-1}$ and random high angle GB misorientations.

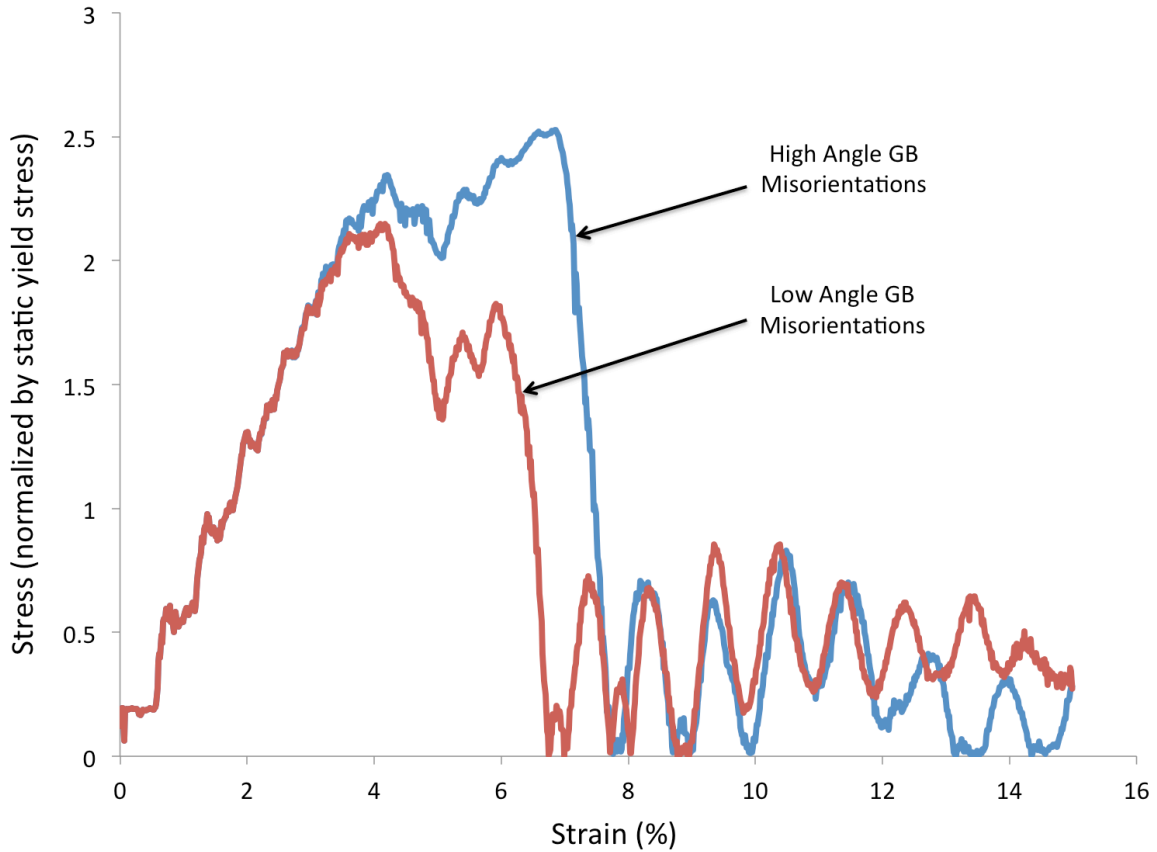


Figure 7.13: Stress versus strain curves for a nominal strain rate loading of $10,000 \text{ s}^{-1}$, for random low and high angle GB misorientations.

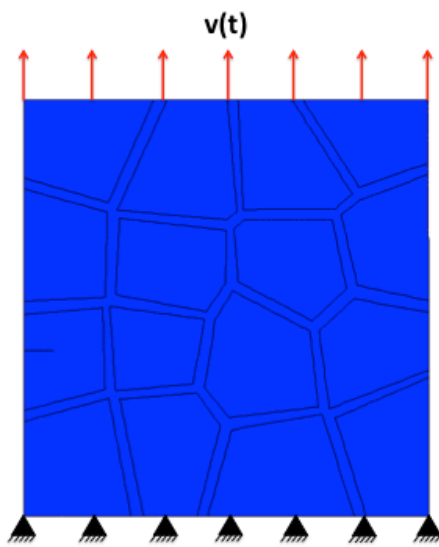


Figure 7.14: The RDX-estane aggregate with loading and boundary conditions, pre-existing crack, grain morphology.

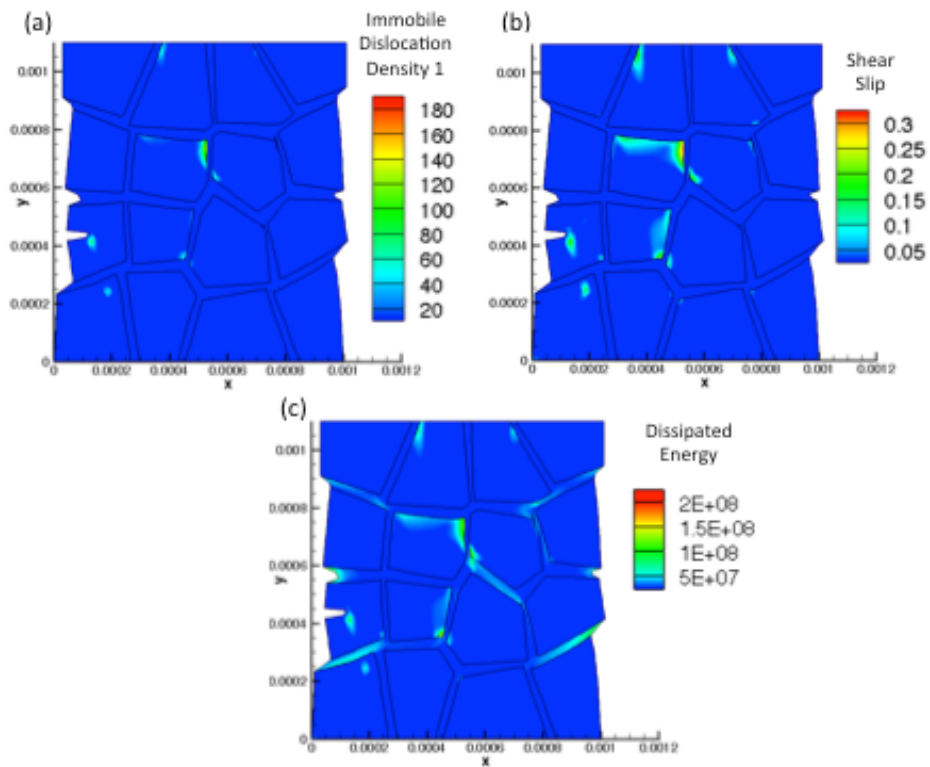


Figure 7.15: (a) Immobile dislocation densities for slip system one, (b) inelastic shear slip, and (c) dissipated energy due to viscous effects and plasticity for a nominal strain rate loading of $10,000 \text{ s}^{-1}$, at a nominal strain of 10%, and random low angle GB misorientations. (Spatial dimensions are in units of meters)

CONCLUSIONS

Through these analyses, high dynamic pressure loads and strain rate loading conditions have been investigated to understand the effects of unbounded local decomposition temperatures and hot spot formation at the microscale. This work showed that hot spot formation is coupled to the inherent crystal defects and how defects result in energy localization at defect sites. This work also showed that the microstructural response of energetic materials is a direct function of the highly anisotropic inelastic deformation that is unique to the energetic crystal RDX, which is a direct consequence of the limited slip systems for inelastic deformation.

For a polymer, where the operating temperature was below the glass transition temperature, hot spot formation resulted at the peripheries of the voids where inelastic deformation was dominant. However, for a polymer where the operating temperature was above the glass transition temperature, hot spot formation occurred at the peripheries of the crystals where shearing in the polymer region was dominant and resulted in crystal to crystal interaction. Crystal to crystal interactions occurred due a thin layer of polymer that was hydro-statically constrained between the crystals that facilitated crystal sliding and allowed for the transfer of loads from one crystal to another. This transfer of load, when large, resulted in inelastic deformation at the crystal peripheries and subsequently hot spot formation.

This work also investigated the effects of fracture at the microscale, where cracks nucleated from internal void porosity due to large stresses. Crack nucleation on the cleavage

planes at the peripheries of the voids was subsequently followed by crack propagation towards the binder where crack arrest occurred. Crack arrest at the binder occurred due to the viscous nature of the polymer material, which resulted in low stress buildup in the polymer binder regions, which acted to arrest the crack. Where cracks impinged upon the interface of the RDX-binder, a buildup of inelastic deformation and subsequent temperature accumulation occurred, which resulted in hot spot formation at the interface due to the effects of fracture.

These analyses have identified the dominant microstructural mechanisms that affect hot spot formation and failure evolution in energetic materials, and the results from these analyses can be used to tailor energetic material aggregates to a desired response based on the microstructural constituents, defects, and behavior.

FUTURE RESEARCH RECOMMENDATIONS

- 1) Develop a crack nucleation model based on dislocation density pileup release relaxation at the RDX-binder interface, to allow for the relaxation of dislocation density pileups, which can nucleate micro-cracks at the grain boundaries.
- 2) Characterize void-to-void interactions to account for void coalescence and shear strain localization in the intervoid regions.
- 3) Investigate the effects of debonding on hot spot formation and local and global failure of energetic aggregates.
- 4) Investigate shear fracture under compressive loadings, and crystal-to-crystal interactions under compression utilizing a contact algorithm.
- 5) Link thermal decomposition to chemical and combustion reactions, to use atomistic and molecular dynamic models to accurately predict the decomposition behavior of energetic materials.
- 6) Use these predictions to improve equations of state for shock loadings of energetic aggregate materials.

REFERENCES

1. R.W. Armstrong, W.L. Elban: Materials Science and Technology, DOI: doi:10.1179/174328406X84049" (2006)
2. F.P. - Bowden, A.D. - Yoffe:
3. S.M. Walley, J.E. Field, M.W. Greenaway: Materials Science and Technology, DOI: doi:10.1179/174328406X91122 (2006)
4. G.M. Swallowe, J.E. Field: Proceedings of the Royal Society of London. A. Mathematical and Physical Sciences, DOI: 10.1098/rspa.1982.0022 (1982)
5. J.E. Field: Acc. Chem. Res., DOI: 10.1021/ar00023a002 (1992)
6. C.M. Tarver, S.K. Chidester, A.L. Nichols: J. Phys. Chem., DOI: 10.1021/jp953123s (1996)
7. L. Borne, J. Mory, F. Schlessner: Propellants, Explosives, Pyrotechnics, DOI: 10.1002/prep.200800206 (2008)
8. J.E. Balzer, J.E. Field, M.J. Gifford, W.G. Proud, S.M. Walley: Combust. Flame, DOI: 10.1016/S0010-2180(02)00373-5 (2002)
9. J.S. Murray, P. Politzer: (2003)
10. R.W. Armstrong, C.S. Coffey, V.F. DeVost, W.L. Elban: J. Appl. Phys., DOI: 10.1063/1.346664 (1990)
11. H. Qiu, V. Stepanov, A.R. Di Stasio, T. Chou, W.Y. Lee: J. Hazard. Mater., DOI: 10.1016/j.hazmat.2010.09.058 (2011)
12. Y. Wu, F. Huang: Mech. Mater., DOI: 10.1016/j.mechmat.2011.08.004 (2011)
13. N.J. Whitworth, J.R. Maw: AIP Conf. Proc., DOI: 10.1063/1.1303610 (2000)
14. Shi, D.W. Brenner: The Journal of Physical Chemistry C, DOI: 10.1021/jp7119735 (2008)
15. P. Politzer, Y. Ma: International Journal of Quantum Chemistry, DOI: 10.1002/qua.20237 (2004)

16. J. Xiao, L. Zhao, W. Zhu, J. Chen, G. Ji, F. Zhao, Q. Wu, H. Xiao: Science China Chemistry, DOI: 10.1007/s11426-012-4797-1 (2012)
17. D. Bedrov, J.B. Hooper, G.D. Smith, T.D. Sewell: J. Chem. Phys., DOI: 10.1063/1.3177350 (2009)
18. W. Zhu, J. Xiao, W. Zhu, H. Xiao: J. Hazard. Mater., DOI: 10.1016/j.hazmat.2008.09.021 (2009)
19. A. Strachan, E.M. Kober, A.C.T.v. Duin, J. Oxaard, W.A.G. III: J. Chem. Phys., DOI: 10.1063/1.1831277 (2005)
20. R. Panchadhara, K.A. Gonthier: Shock Waves, DOI: 10.1007/s00193-010-0287-6 (2011)
21. M.R. Baer: Thermochimica Acta, DOI: 10.1016/S0040-6031(01)00794-8 (2002)
22. A. Barua, Y. Horie, M. Zhou: J. Appl. Phys., DOI: 10.1063/1.3688350 (2012)
23. A. Barua, M. Zhou: Modell Simul Mater Sci Eng (2011)
24. R. Bouma, W. Duvalois, A. Heijden: J. Microsc. (2013)
25. R. Bouma, A. van der Heijden, T. Sewell, D. Thompson: Numerical Simulations of Physical and Engineering Processes (InTech Publisher, Rijeka Croatia) (2011)
26. S. Palmer, J. Field: Proceedings of the Royal Society of London A. Mathematical and Physical Sciences (1982)
27. J. Sharma, R. Armstrong, W. Elban, C. Coffey, H. Sandusky: Appl. Phys. Lett. (2001)
28. D. Smith, B. Thorpe: J. Mater. Sci. (1973)
29. Y. Wang, J. Li, A.V. Hamza, T.W. Barbee Jr: Proc. Natl. Acad. Sci. U. S. A., DOI: 0702344104 [pii] (2007)
30. J. Zhang, G. Liu, J. Sun: Acta Materialia (2014)
31. A. Voevodin, J. Zabinski: J. Mater. Sci. (1998)
32. W.M. Ashmawi, M.A. Zikry: J. Eng. Mater. Technol., DOI: 10.1115/1.1421611 (2002)
33. M.A. Zikry, M. Kao: J. Mech. Phys. Solids, DOI: [http://dx.doi.org/10.1016/0022-5096\(96\)00049-X](http://dx.doi.org/10.1016/0022-5096(96)00049-X) (1996)

34. P. Franciosi, M. Berveiller, A. Zaoui: *Acta Metallurgica*, DOI: [http://dx.doi.org/10.1016/0001-6160\(80\)90162-5](http://dx.doi.org/10.1016/0001-6160(80)90162-5) (1980)
35. P. Shanthraj, M.A. Zikry: *Acta Materialia*, DOI: 10.1016/j.actamat.2011.08.041 (2011)
36. L. Kubin, B. Devincre, T. Hoc: *Acta Materialia*, DOI: <http://dx.doi.org/10.1016/j.actamat.2008.08.012> (2008)
37. T. Rasmussen, T. Vegge, T. Leffers, O.B. Pedersen, K.W. Jacobsen: *Philos. Mag. A*, DOI: 10.1080/01418610050024585 (2000)
38. M. Kaliske, H. Rothert: *Comput. Mech.*, DOI: 10.1007/s004660050171 (1997)
39. E.M. Mas, B.E. Clements, B. Blumenthal, C.M. Cady, G.T. Gray, C. Liu: *AIP Conference Proceedings*, DOI: <http://dx.doi.org/10.1063/1.1483625> (2002)
40. P.A. Cardao, J.C. Gois, J.A. Campos: *AIP Conference Proceedings*, DOI: 10.1063/1.1303603 (2000)
41. A.R. Johnson, T. Chen: *Comput. Methods Appl. Mech. Eng.*, DOI: <http://dx.doi.org/10.1016/j.cma.2004.03.014> (2005)
42. D.P. Flanagan, T. Belytschko: *Int J Numer Methods Eng.*, DOI: 10.1002/nme.1620170504 (1981)
43. M.A. Zikry: *Comput. Struct.*, DOI: 10.1016/0045-7949(94)90004-3 (1994)
44. H.G. Gallagher, P.J. Halfpenny, J.C. Miller, J.N. Sherwood, D. Tabor: *Philosophical Transactions: Physical Sciences and Engineering* (1992)
45. E.N. Brown, P.J. Rae, E.B. Orler: *Polymer*, DOI: 10.1016/j.polymer.2006.08.032 (2006)
46. H. Czerski, W.G. Proud: *J. Appl. Phys.*, DOI: 10.1063/1.2818106 (2007)
47. W.M. Lee, M.A. Zikry: *Int. J. Solids Structures*, DOI: 10.1016/j.ijsolstr.2012.07.003 (2012)
48. H.J. Bruckman Jr., J.E. Guillet: *Canadian Journal of Chemistry*, DOI: 10.1139/v68-534 (1968)
49. L. Borne: 10th Symposium on Detonation

50. S.R. Annapragada, D. Sun, S.V. Garimella: Computational Materials Science, DOI: <http://dx.doi.org/10.1016/j.commatsci.2006.12.008> (2007)
51. C.A. Stoltz, B.P. Mason, J. Hooper: Journal of Applied Physics (2010)
52. L. Borne, J. Patedoye, C. Spyckerelle: Propellants, Explosives, Pyrotechnics, DOI: 10.1002/(SICI)1521-4087(199908)24:4<255::AID-PREP255>3.0.CO;2-2 (1999)
53. B.J. Briscoe, R.W. Nosker: Wear, DOI: [http://dx.doi.org/10.1016/0043-1648\(84\)90140-6](http://dx.doi.org/10.1016/0043-1648(84)90140-6) (1984)
54. U.S. Lindholm: J. Mech. Phys. Solids, DOI: [http://dx.doi.org/10.1016/0022-5096\(64\)90028-6](http://dx.doi.org/10.1016/0022-5096(64)90028-6) (1964)
55. H. Van Swygenhoven, P.M. Derlet: Phys.Rev.B, DOI: 10.1103/PhysRevB.64.224105 (2001)
56. B. Kim, K. Hiraga, K. Morita, H. Yoshida, B. Ahn: Acta Materialia, DOI: <http://dx.doi.org/10.1016/j.actamat.2009.08.001> (2009)
57. D.E. Hooks, K.J. Ramos, A.R. Martinez: J. Appl. Phys., DOI: 10.1063/1.2214639 (2006)
58. D.A. LaBarbera, M.A. Zikry: J. Appl. Phys., DOI: <http://dx.doi.org/10.1063/1.4811684> (2013)
59. J.E. Field, N.K. Bourne, S.J.P. Palmer, S.M. Walley, J. Sharma, B.C. Beard: Philosophical Transactions of the Royal Society of London. Series A: Physical and Engineering Sciences, DOI: 10.1098/rsta.1992.0034 (1992)
60. J.D. Clayton, R. Becker: J. Appl. Phys., DOI: 10.1063/1.3695392 (2012)
61. D.E. Hooks, K.J. Ramos, D.F. Bahr: AIP Conference Proceedings, DOI: 10.1063/1.2833242 (2007)